Fakultät für Medizin

Institut für Zellbiologie des Nervensystems

Studying axonal and glial dynamics during CNS myelination and remyelination *in vivo* using zebrafish

Stavros Vagionitis

Vollständiger Abdruck der von der Fakultät für Medizin der Technischen Universität München zur Erlangung des akademischen Grades eines

Doctor of Philosophy (Ph.D.)

genehmigten Dissertation.

Vorsitzende/r: Prof. Dr. Stefan Lichtenthaler

Betreuer/in: Priv.-Doz. Dr. Tim Czopka

Prüfer der Dissertation:

1. Prof. Dr. Thomas Misgeld

2. Prof. Dr. Martin Kerschensteiner

Die Dissertation wurde am 30.07.2021 bei der Fakultät für Medizin der Technischen Universität München eingereicht und durch die Fakultät für Medizin am 22.09.2021 angenommen.

Abstract

Rapid and precise signal transduction is essential for the function of the central nervous system (CNS). Oligodendrocytes wrap neuronal axons with myelin in a process called myelination. Myelination isolates the axons electrically, restricts axonal sodium channels to specific axonal domains, called nodes of Ranvier and provides axons with necessary metabolites. Myelination is a life-long process that often produces extraordinarily complex patterns of myelin coverage on specific axons. The homeostatic state of myelination is often compromised in pathologies, like Multiple Sclerosis. However, myelin can regenerate in a process called remyelination. It is thus important to understand how myelination patterns are established during development, how do cells of the oligodendrocyte lineage respond to myelin loss and how can they select between demyelinated and unmyelinated axons during remyelination. Using larval zebrafish, I could establish a model of local demyelination within the spinal cord using 2-photon laser oligodendrocyte ablations and causing minimal bystander damage. I was able to describe the dynamics of demyelination as well as the clearance of myelin debris by immune cells. By using *in vivo* microscopy, I observed that oligodendrocyte numbers fail to fully recover after demyelination. By electron microscopy, I could verify that indeed demyelinated axons are only partially remyelinated, indicating an incomplete regenerative response. Moreover, newly differentiated oligodendrocytes showed no preference between ensheathing demyelinated or previously unmyelinated axons. Using different transgenic markers to label nodes of Ranvier, I was able to identify that neuronal Neurofascin formed clusters along unmyelinated axon stretches on positions that often corresponded to the positions of the nodes of Ranvier after myelination. By genetically ablating neuronal Neurofascin, I described that the average internode distance along myelinated axons increases and becomes more variable, an effect that could be rescued by re-introducing the Neurofascin transgenic marker. Lastly, by ablating oligodendrocytes that myelinated axons expressing the Neurofascin marker, I could show that Neurofascin does not diffuse upon myelin loss and that clustered Neurofascin could be moved, likely by intrinsic axonal mechanisms. Together, I was able to describe that zebrafish spinal cord does not

have an increased capacity to repair local, titrated oligodendrocyte loss. I also found that neurons participate in the control of node of Ranvier positioning along their length, with neuronal Neurofascin playing a functional role in this process. Lastly, I was able to show that within myelin lesions, Neurofascin remains aggregated and that Neurofascin aggregates can move, possibly by axonal mechanisms.

Zusammenfassung

Eine schnelle und präzise Signalübertragung ist für die Funktion des Zentralnervensystems (ZNS) essenziell. Oligodendrozyten umhüllen neuronale Axone mit Myelin in einem Prozess, der als Myelinisierung bezeichnet wird. Die Myelinisierung isoliert die Axone elektrisch, beschränkt die axonalen Natriumkanäle auf spezifische axonale Domänen, die als Ranvier-Schnürringen bezeichnet werden, und versorgt die Axone mit den notwendigen Metaboliten. Myelinisierung ist ein lebenslanger Prozess, der oft außergewöhnlich komplexe Muster der Myelinbedeckung auf bestimmten Axonen erzeugt. Der homöostatische Zustand der Myelinisierung ist bei Pathologien wie Multipler Sklerose häufig beeinträchtigt. Myelin kann sich jedoch in einem Prozess regenerieren, der als Remyelinisierung bezeichnet wird. Daher ist es wichtig zu verstehen, wie Myelinisierungsmuster während der Entwicklung etabliert werden, wie Zellen der Oligodendrozyten-Linie auf Myelinverlust reagieren und wie sie, während der Remyelinisierung zwischen demyelinisierten und unmyelinisierten Axonen auswählen können. Unter Verwendung von Zebrafischlarven konnte ich ein Modell der lokalen Demyelinisierung im Rückenmark mit 2-Photonen-Laser-Oligodendrozyten-Ablationen erstellen, das minimalen Schaden durch Zuschauer verursacht. Ich konnte die Dynamik der Demyelinisierung sowie die Beseitigung von Myelintrümmern durch Immunzellen beschreiben. Mit In-vivo-Mikroskopie beobachtete ich, dass sich die Oligodendrozytenzahlen nach Demyelinisierung nicht vollständig erholen. Durch Elektronenmikroskopie konnte ich bestätigen, dass demyelinisierte Axone tatsächlich nur teilweise remyelinisiert sind, was auf eine unvollständige regenerative Reaktion hinweist. Darüber hinaus zeigten neu differenzierte Oligodendrozyten keine Präferenz zwischen demyelinisierten oder zuvor nicht myelinisierten Axonen. Mit verschiedenen transgenen Markern zur Markierung von Ranvier-Schnürringen konnte ich feststellen, dass neuronale Neurofascin Cluster entlang nicht myelinierter Axonabschnitte an Positionen bildeten, die oft den Positionen der Ranvier-Schnürringen nach der Myelinisierung entsprachen. Durch die genetische Ablation von neuronalem Neurofascin habe ich beschrieben, dass der durchschnittliche Internodienabstand entlang myelinisierter Axone zunimmt und variabler wird, ein Effekt, der durch

die Expression des transgenen Neurofascin-Markers gerettet werden könnte. Schließlich konnte ich durch Abtragen von Oligodendrozyten, die Axone, die den Neurofascin-Marker exprimieren, myelinisierte, zeigen, dass Neurofascin bei Myelinverlust nicht diffundiert und dass geclustertes Neurofascin wahrscheinlich durch intrinsische axonale Mechanismen bewegt werden könnte. Gemeinsam konnte ich beschreiben, dass das Rückenmark von Zebrafischen keine erhöhte Fähigkeit besitzt, den lokalen, titrierten Oligodendrozytenverlust zu reparieren. Ich fand auch, dass Neuronen an der Kontrolle der Ranvier-Schnürringen-Position entlang ihrer Länge beteiligt sind, wobei neuronales Neurofascin eine funktionelle Rolle in diesem Prozess spielt. Schließlich konnte ich zeigen, dass Neurofascin innerhalb von Myelinläsionen aggregiert bleibt und sich Neurofascin-Aggregate bewegen können, möglicherweise durch axonale Mechanismen.

Acknowledgements

First and foremost, I would like to express my sincere gratitude towards my mentor Dr. Tim Czopka for believing in me and including me in his group. I thank him for his guidance both in experimental matters as well as in my character development. I have certainly learned a lot working with him and I hope to have become a better scientist during the process.

Moreover, I consider myself especially lucky for having chosen Prof. Dr. Thomas Misgeld and Prof. Dr. Martin Kerschensteiner as members of my thesis advisory committee, as their constructive input during our discussions has greatly benefited me. I would like to give special thanks to Thomas, for his handling of the Covid-19 pandemic, as he helped each and every one of us feel safe. I am grateful to have received financial support from the MLST graduate school, that funded a year of my dissertation, provided a considerable consumables budget and supported my participation to international conferences.

Next, I would like to thank all the members of the Czopka, Misgeld and Godinho labs for offering a welcoming and positive work environment, especially our former technician Wenke Barkey, whose assistance has been proven invaluable. I would also like to thank Kristina, Moni and Yvonne for their irreplaceable contribution to the day to day matters of the institute. I would also like to thank Dr. Martina Schifferer for introducing my to electron microscopy and for her contribution in acquiring these data.

Lastly, I would like to thank the people closer to me, for their presence has helped me enormously during the last few years. First, Franzi and Roberta, you have been wonderful colleagues and friends and I will always cherish your friendship. Aris, Elina and Giorgos, no matter how far we are, I know you have always been there for me. I would like to dedicate this to my partner, Eleni, who has been brightening my days and has supported me immeasurably. Lastly, there are really not enough words to express my gratitude to the most important people in my life, my parents. They are the best parents there are and I owe them everything.

Table of contents

1. Introduction

“There is a grandeur in this view of life, […] from so simple a beginning endless forms most beautiful and most wonderful have been and are being evolved”. With this most influential quote, Charles Darwin summed up masterfully the essence of evolution, the mechanism that describes the origin and interconnectivity of all life on Earth. Perhaps one of the most complex and, certainly in my view, most wonderful of these forms is the Nervous System (NS) of organisms. The NS allows organisms to receive and process information about their environment and to coordinate their responses to those stimuli. The NS is anatomically divided in two major parts, the Central Nervous System (CNS), consisting of the brain and the spinal cord, and the Peripheral Nervous System (PNS), consisting of the sensory elements that project towards the CNS as well as the motor elements that project from the CNS to the periphery.

There are two major classes of cells in the CNS, neurons and glia. Seminal neuroanatomical analyses during the late 19th and early 20th century described thoroughly the morphology of these cells. It was initially believed that glia cells provide structural support for the neurons and hold the whole tissue together (glia < Greek: *γλοία* or *γλία*, meaning glue). The major types of glial cells are astrocytes, microglia and oligodendroglia. Despite their original characterisation as mere connective tissue of the CNS, glial cells have since been shown to mediate a variety of functions within the CNS. Astrocytes are important for neuronal tissue homeostasis, they form the blood-brain barrier, protecting the CNS from passive molecular diffusion, they cover and support neuronal synapses and they provide growth factors and metabolites. Microglia are non-neuronal cells which are responsible for the immune responses that happen within the CNS. Finally, oligodendrocytes produce myelin, a lipoproteinic substance that wraps around CNS axons (Byrne and Roberts, From molecules to networks).

1.1 Oligodendrocytes and CNS myelination.

The term oligodendroglia refers to oligodendrocytes (OLs) and oligodendrocyte precursor cells (OPCs). OLs were first described by del Río Hortega ((Pérez-Cerdá et al., 2015), characterized by the morphology of their relatively sparce process network (oligodendrocyte is a composite word deriving from the Greek elements oligo- (όλιγο = few), dendro- (δένδρο = tree) and -cyte (<κύτταρο = cell). One of the main functions of OLs is myelination, the deposition of myelin on axonal surface. The high fat concentration in myelinated areas renders them relatively light in colour, while non-myelinated areas, rich in neuronal somata, appear darker. This led to the establishment of the terms white and grey matter, respectively (Purves et al., 2004). Initial descriptions of myelinated axons suggested myelin as being a structure of axonal origin, drawing similarities to bone marrow, after which it was named (from Greek μυελός = marrow). It was only later identified that it is in fact the product of OLs in the CNS and Schwann cells in the PNS (Rosenbluth, 1999).

Myelin coverage of axons isolates them electrically from their environment. Moreover, axons are not fully covered by myelin, but instead myelin appears along axons in intermittent segments, separated by sort non-myelinated areas called nodes of Ranvier. The nodes of Ranvier, apart from the lack of myelin, are characterized by a high local concentration of voltage-gated sodium and potassium channels. This local concentration acts synergistically with the electrical isolation of myelinated segments to result in fast signal transduction along myelinated axons, in a mode called saltatory conduction. In saltatory conduction, depolarization is not propagated linearly along the axon. Instead, voltage-gated sodium channels are only localised to the nodes of Ranvier and at these sites, depolarisation can take place and the subsequent ion current can flow passively through the myelinated segment until the next node. This flow causes the depolarisation of the second node and the process is repeated. Because depolarisation seems to jump from node to node, this mode of conduction has been termed saltatory. The provided insulation by myelin increases the conduction velocity from 0.5-10 m/s along unmyelinated axons to up to 150 m/s along myelinated ones (Purves et al., 2004).

Electrical isolation of axons favours signal transduction energetically, by lowering the cost of action potential propagation in terms of ATP consumption. Moreover, the finding that myelin loss can affect the survival of axons themselves, lead many researchers in the field to hypothesize that myelin might have different roles that promote axonal survival. It has been well described that astrocytes can provide metabolic support to the neurons they contact. The discovery of monocarboxytransporter1 (MCT1) expression by OLs and its localization within the internode lead to subsequent research that revealed how OLs can provide (primarily) lactate to axons, while in lack of this transport, axon morphology and even neuronal survival was affected (Fünfschilling et al., 2012; S. Lee et al., 2012). The consensus at the moment is that metabolic support constitutes one of the major functions of OLs in the glia-axon interface (Morrison et al., 2013; Nave, 2010b, 2010a). More recent data suggest that metabolic support by OLs can directly affect cognitive functions, independently of saltatory conduction (Moore et al., 2020).

Several recent studies have highlighted the importance of OLs in other neuronal functions. OLs express glutamine synthetase, which is dispensable for myelination but indispensable for brain glutamate signalling (Xin et al., 2019). OLs also can modulate neurotransmitter release and presynaptic properties by expressing BDNF (Jang et al., 2019).

OL generation has long been shown to be responsive to neuronal activity and task learning. It has been shown that piano practicing can induce white matter changes (Bengtsson et al., 2005). Learning a complex visuo-motor task was again shown to affect the neuroanatomy of white matter (Scholz et al., 2009). More recently a study showed that integration of newly generated OLs in the adult somatosensory cortex is highly enhanced by motor task learning (Hughes et al., 2018).

Not only is neuronal activity shaping white matter, but myelination is also important for higher cognitive functions. It has been shown to play a role in motor skill acquisition (McKenzie et al., 2014). Recent studies have shown that neuronal activity during fear learning leads to the formation of new myelin, which is needed for maintaining the memory (Pan et al., 2020). Along the same lines, another

study showed that inhibition of new OL formation negatively affects memory consolidation (Steadman et al., 2020).

Not all axons exhibit the same myelination pattern. Many axons are fully myelinated along their lengths, while others show different forms of myelination. Recent work, published by our group and others has described sparse myelination in cortical neurons as well as in the zebrafish spinal cord (Auer et al., 2018; Tomassy et al., 2014). However, since myelination is a process that continues throughout life, it has proven challenging to dissect whether the sparse myelination phenotype represents a final state of myelination or if it is a steppingstone towards full myelination.

To summarize, OLs are the glia subtype responsible for producing myelin, a fatty substance that wraps around the axons and supports their function by electrical insulation, metabolic aid as well as via signalling. Myelination persists and changes throughout life in a complex interplay between neurons and OLs.

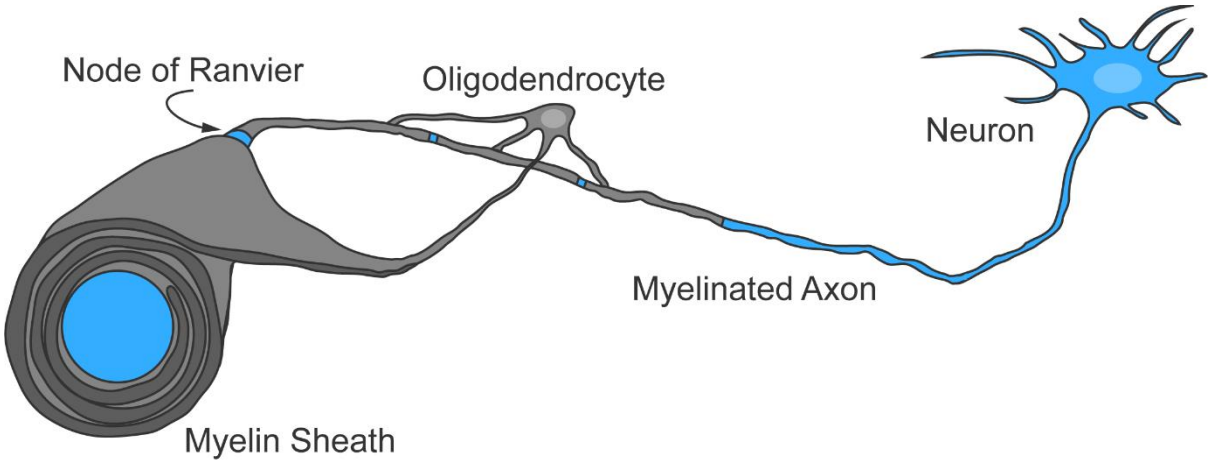

Figure 1.1 Example illustration of a myelinated axon

Illustration of a myelinated axon (cyan) of the CNS. Oligodendrocytes (grey) produce myelin that wraps around the axons in intermitted segments called myelin sheaths. Consecutive sheaths are separated by short, non-myelinated gaps, the nodes of Ranvier.

1.2 Selecting target axons for myelination.

As already mentioned, myelination is an almost lifelong process, due to the presence of OPCs, the most proliferative cell population in the CNS (M. R. Freeman & Rowitch, 2013). In fact, OPCs maintain a persistent population within the CNS. Moreover, OPCs differentiate constantly, replacing lost myelin due to old OL death and adding myelin on other axons (Young et al., 2013). In fact, there has been several studies that showed that myelination is not static, but it increases overall for almost throughout the lifetime (Hill et al., 2018; Miller et al., 2012), while new myelin can form both on previously partially myelinated and unmyelinated axons both in physiological (Hughes et al., 2018) condition or during local remyelination (Snaidero et al., 2020). In contrast to Schwann cells in the PNS, which are dedicated in myelinating a single axon by a single internode, OLs are able to make multiple sheaths, targeting multiple axons at the same time. The sheaths that a single OL makes can vary in length, but all are created within a narrow timeframe of 5 hours *in vivo,* as shown in zebrafish. Most of the newly formed sheaths are maintained and grow in length, while a small fraction is retracted (Czopka et al., 2013). This indicates the putative presence of a system that selects axon targets for myelination during OPC differentiation.

While the exact mechanism of axon selection for myelination in the CNS is still unknown, it has already been described that axon diameter (calibre), surface molecule expression and neuronal activity seem to regulate myelination. First, it has been shown *in vitro* that OLs fail to myelinate inert fibres with diameter smaller than 0.4 μm (Bechler et al., 2015; S. Lee et al., 2012). Furthermore, more recently, by inactivating the phosphatase and tensin homolog (PTEN) in cerebellar granule cells, researchers managed to increase their calibre and thus increase their myelination (Goebbels et al., 2017). Apart from axon diameter, since differentiating OLs are in direct contact with axonal surface, it has also been proposed that several axonal surface molecules affect their targeting for myelination. These cues include, among others, polysialylated neural cell adhesion molecule (PSA-NCAM), which is known to be downregulated when myelination starts (P. Charles et al., 2000; Oumesmar et al., 1995), the junction adhesion molecule (JAM2), which is known to be expressed in

non-myelinated neuronal surfaces (the somatodendritic region) (Redmond et al., 2016) and the transmembrane protein LINGO-1 (Jepson et al., 2012; X. Lee et al., 2007; Mi et al., 2005). These factors are all negative regulators for myelination. There have also been described several positive regulators such as N-cadherin (Chen et al., 2017; Schnädelbach et al., 2001), the EphA/B tyrosine kinase receptor (Linneberg et al., 2015), and L1-CAM (Laursen et al., 2009).

As mentioned in the previous section, there seems to be a strong correlation between neuronal activity and myelination. Indeed, it has been shown that increased neuronal activity is associated with increased myelination and axon selection both in development and in adulthood. This effect of neuronal activity on OPCs seems to be associated with synaptic vesicular release, since OPCs are known to express neurotransmitter receptors and form synapses with glutamatergic and GABA-ergic axons (Akay et al., 2021). However, it has also been known that activity-dependent axon selection is prominent in some neuronal subtypes, while it is negligible in others (Almeida, 2018; Klingseisen and Lyons, 2018; Pan and Monje, 2020). This would suggest that axonal identity may have a different influence in axon selection for myelination. It is already known that different axonal subtypes show different myelination coverage (Auer et al., 2018; Nelson et al., 2020; Tomassy et al., 2014). However, whether axon calibre, the expression and presentation of specific molecules, levels of activity or a combination of the three serves as a determinant of axon selection for OPCs is a complicated subject which prompts further investigation.

1.3 Models and prominent features of remyelination

The important implications of myelination for CNS function can be further demonstrated by examining the effects of myelin damage to the CNS. There have been several reported pathologies that are characterized either by myelin loss (demyelination) or myelin deformity (dysmyelination). In humans, the most prominent of these disorders is Multiple Sclerosis (MS), which is characterized by local demyelination within CNS lesions. As previously mentioned, CNS myelin is formed throughout life by differentiation of OPCs to OLs in order to either replace dying OLs or myelinate new axon targets. Through this OL lineage feature, myelin can be replaced even in cases of extensive pathology in a regenerative process called remyelination (R. J. M. Franklin & ffrench-Constant, 2008). This can lead to phenotype rescue by protecting axons that would perish after being demyelinated and by restoring conduction velocity and network communication.

As remyelination is a regenerative process, it should be able to restore function. This means that OPCs should be able to differentiate at an increased rate, in order to replace the lost myelin, while simultaneously maintaining their own population. While it remains primarily thought of that remyelination requires the differentiation of OPCs, recent studies have shown evidence that differentiated OLs that were spared during demyelination could also participate in remyelination (Bacmeister et al., 2020; Neely et al., 2020). Moreover, differentiating OPCs should be able to accurately target demyelinated axons while differentiating. Lastly, since it is known that certain sheath characteristics (sheath length and thickness) affect conduction velocity (Brill et al., 1977), remyelinating sheaths should have similar structure to lost sheaths, in order to restore conduction within the network.

In order to study demyelination and remyelination, several animal models have been used, the most common of which is Experimental Autoimmune Encephalitis (EAE), which resembles some of the clinical characteristics of MS. EAE's main advantage is that the effectors of OL damage and demyelination are self-reactive immune cells, similar to human MS. However, while in MS auto-

immunoreactivity does not appear to have a consistent protein target, EAE models are induced by specifically guiding the immune system to targeting specific myelin proteins such as MOG or MBP (Gold et al., 2000).

Other models use chemical compounds that specifically affect myelin, like lysolecithin (Cunha et al., 2020; Jeffery & Blakemore, 1995) or OLs, like ethidium bromide (Blakemore, 1982) and cuprizone (Baxi et al., 2017). Lysolecithin acts as a myelinolytic, dissolving lipid membranes, including myelin sheaths, and thus causing local demyelination, only at the injection cite. However, it has been shown that axons also suffer injury 24 hours post lysolecithin application. Moreover, it has been shown that other cell types (astrocytes, microglia, OPCs) are also sensitive to lysolecithin (Plemel et al., 2018). Ethidium bromide injections also have local effect as ethidium bromide is a DNA intercalator that ablates cells that absorb it. It has been applied within white matter, where the predominant cell type present is OLs. However, it is known to affect other cell types, including OPCs and astrocytes (Blakemore, 1982; Blakemore & Franklin, 2008; Sim et al., 2002). Both lysolecithin and ethidium bromide, while effective as chemical ablation agents, have little specificity to OLs. On the other hand, cuprizone is the only chemical thought to specifically affect OLs. It can be administered systemically as a food supplement, which renders the precise localisation and extent of myelin lesions variable (Blakemore & Franklin, 2008). It also has been shown to affect axons (Gudi et al., 2017). Overall, while all chemical ablation agents can effectively reduce the numbers of OLs and cause demyelination, this effect can often extend to other cell types within myelin lesions, leading to a complicated pathological phenotype the features of which are hard to interpret.

In order to address the problem of specificity that is common in chemical demyelination models, researchers have more recently employed chemogenetics as a means of causing demyelination. In this approach, transgenic animals are used, which express chemical receptors or enzymes in a cell type-specific manner. These animals are treated with a chemical agent that is not affecting negative cells for the genetic component, but positive cells either uptake or metabolise the chemical and are thus led to cell death. Such systems are the NTR-MTZ system (Chung et al., 2013; Sekizar et al.,

2015) as well as the DTR/DTX system (Gritsch et al., 2014; Oluich et al., 2012) and the TRPV1-capsaicin system (Neely et al., 2020). However, expression levels of the genetic component of these systems, as well as the bioavailability of the chemical component can be causes for variability in these systems.

Finally, targeted laser-ablations of OLs have also been frequently conducted (Auer et al., 2018; Chapman et al., 2020; Kirby et al., 2006; Snaidero et al., 2020). Laser ablations are by design highly specific since individual cells are manually targeted and ablated. They are also less variable because the extent of damage can be highly predictable. However, in lack of sophisticated, automated, laser targeting systems, this ablation method remains highly laborious, limiting the number of possible cell targets per experiment and thus it is not yet possible to cause extensive myelin damage in this manner.

By using the aforementioned models, researchers are able to induce demyelination and study remyelination dynamics in animal models, in order to better understand the underlying mechanisms of these processes. It is long known that in MS, remyelination is often inefficient and incapable of causing clinical improvement (Prineas & Connell, 1979). Some of the aforementioned animal models are instead characterised by complete remyelination, while only extended cuprizone treatment leads to remyelination failure (Bacmeister et al., 2020; Lassmann & Bradl, 2017). It is clear that the animal models of demyelination and remyelination are not true models of MS (R. J. Franklin & ffrench-Constant, 2017). Lastly, aging is shown to affect the ability of OPCs to differentiate, so this might be another reason for remyelination failure irrespective of another underlying pathology (Hill et al., 2018; Münzel et al., 2014). However, it remains important to understand how and why remyelination fails in MS and in aging, despite the presence of a potent OPC population.

It is well described that myelin sheath thickness and internode length are important for modulating conduction velocity (Brill et al., 1977). Regarding myelin sheath thickness, it is understood that remyelination leads to the formation of thinner myelin sheaths, a feature that has been used for identifying remyelinated axons in ultrastructural analyses (Blakemore, 1974; Ludwin & Maitland,

1984). It is however not known if the observed difference in myelin sheath thickness is simply due to the difference in OL age, with the remyelinating sheaths being thinner because they are significantly younger than older sheaths that were not affected during demyelination. It has been also shown that remyelination leads to restoration of conduction velocity. However, since remyelinating sheaths are thinner than normal, it can be calculated that AP propagation is probably slower than in normally myelinated axons. (R. J. M. Franklin & ffrench-Constant, 2017).

As I described previously, the three major factors that affect axon choice in development are axonal calibre, expression of molecules on the axonal surface and neuronal activity. It is easy to hypothesise that these factors should also play a role in axon selection in remyelination OPCs within a demyelinated lesion should be able to recognise one or a combination of these features in order to accurately select and repair demyelinated axons. A recent study has shown that indeed, following laser ablations of individual OLs, the majority of myelin sheaths (66%) re-form in remyelination (Snaidero et al., 2020). Two other studies, using cuprizone to cause more extensive myelin damage, have shown that remyelination in this setting is not as precise. However, learning a complex motor task seemed to increase remyelination accuracy (Bacmeister et al., 2020; Orthmann-Murphy et al., 2020). This indicates that neuronal activity associated with motor learning can help target axon selection.

Snaidero et al. showed that despite the presence of a multitude of smaller calibre, unmyelinated axons within a demyelinated area, the calibre of axons with newly formed myelin in remyelination was higher and similar to unaffected, myelinated axons. Also, the same study provides an example longitudinal electron micrograph of an axon with a remyelinated segment and an unmyelinated segment and shows that the myelinated segment had obviously larger calibre (Snaidero et al., 2020). While it is known that calibre is an important selection factor for axon selection (S. Lee et al., 2012), it remains unclear whether demyelinated axon diameter decreases gradually after myelin loss or if axons retain their size as a structural selection cue for remyelination.

Overall, demyelination can cause severe neurological pathologies like MS. Remyelination does take place due to the presence of OPCs in the CNS but it is often inefficient to completely rescue the phenotype and alleviate the pathology. This has prompted research using a multitude of animal models, through which many discoveries on the features of remyelination, sheath thickness, length and axon choice have been described. However, the problem of enhancing remyelination overall and remyelination fidelity still remains and further experiments are needed in order to understand the OPC potential and how to enhance it in such settings.

1.4 Anatomy and molecular composition of nodes of Ranvier.

As described above, nodes of Ranvier are, by definition, the intermittent gaps between consecutive myelin sheaths on neuronal axons. In fact, with the nodes of Ranvier as points of reference, one can define specific domains around them. The paranodal junctions or paranodes are the areas next to the nodes of Ranvier that include the axon-OL contact points. On the paranodes, each layer of myelin is tethered on the axonal surface, via adhesion molecule interactions, making distinct structures often seen in electron micrographs, the paranodal loops of myelin. Adjacent to the paranodes, under the myelin sheath, the next axonal domain is the juxtaparanode and finally the internode.

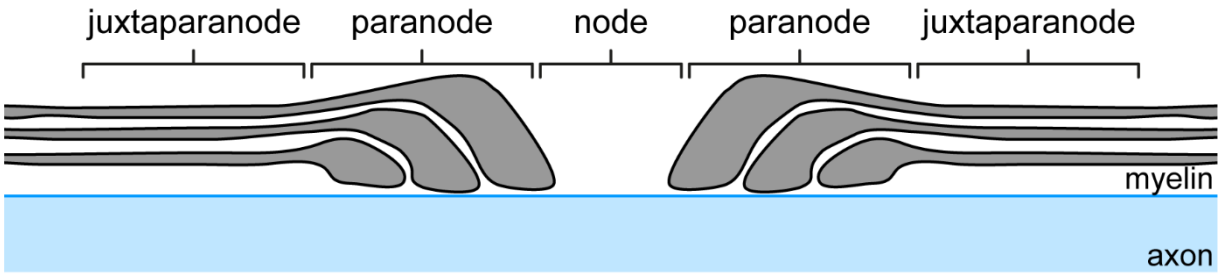

Figure 1.2 Compartments of the nodes of Ranvier

Illustration of the compartments of a node of Ranvier, marking the nodal region, the paranodes and the juxtaparanodes.

These different compartments are characterized by the differential localization of certain, well described, molecules. These molecules can be categorized by their position along the axon (node, paranode, juxtaparanode) or by their position in relation to the axonal cross-section. There are cytoplasmic molecules that are either part of axonal cytoskeleton or they are interacting with it, there are transmembrane molecules that can contact both their cytoplasmic counterpart and proteins outside the axon, in the extracellular matrix (ECM). Finally, there are adhesion molecules that are tethered to the membrane, contacting only proteins in the ECM. For a detailed overview of perinodal molecular organization, see Figure 1.4 as adapted from (Stathopoulos et al., 2015).

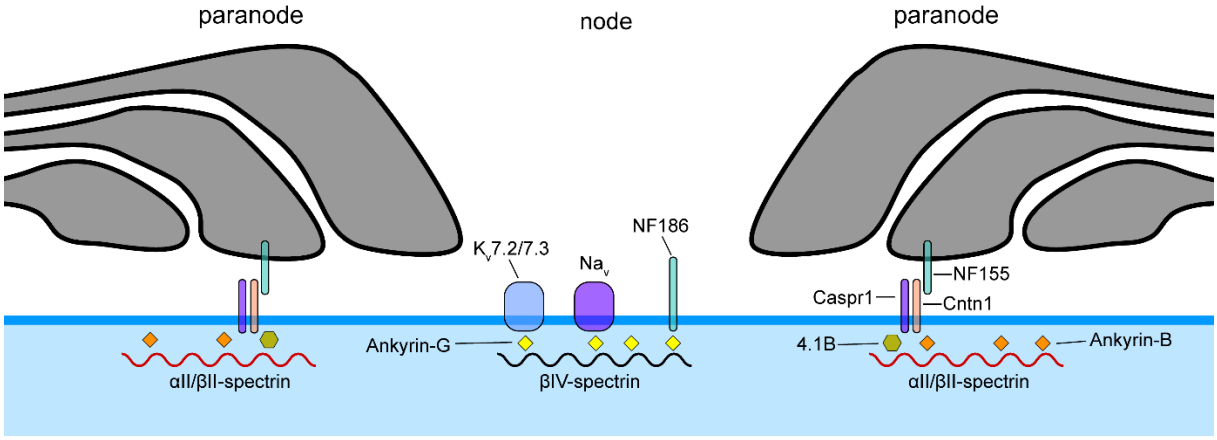

Figure 1.3 Molecular composition of the nodes of Ranvier

Overview of the molecules that localise to the nodes of Ranvier and the adjacent paranodes, adapted from Stathopoulos et al. 2015.

Several of the structural and molecular components of the perinodal area have been linked to nodal assembly and maintenance. The main sources of interactions that are relevant for nodal homeostasis are the paranodal junctions at the axoglial interface, the ECM interactions at the node itself and interactions with elements of the cytoskeleton within myelinated neurons.

Paranodal junctions are a form of septate-like junctions (Boyle et al., 2001) that depend on the tripartite interaction between Caspr and Cntn1 (from the axonal side) with Neurofascin155 (NF155) from the glial side (Perrine Charles et al., 2002). When Caspr and Cntn1 were genetically ablated, this caused severe motor deficits and the mutation was lethal (up to P33 and P18 respectively) (E. O. Berglund et al., 1999; Bhat et al., 2001). These mutations were shown to disrupt the septate-like junctions of the paranodes. However, sodium channels seemed to cluster to the nodes, despite the lack of intact paranodal barriers flanking them (Bhat et al., 2001; Boyle et al., 2001).

NF155 is a product of the *nfasc* gene. Volkmer at al. showed that the *nfasc* gene actually expresses many different mRNAs, suggesting that the transcript is subject to alternative splicing (Volkmer et al., 1992). The most relevant isomorphs of Neurofascin for myelination are Neurofascin186 (NF186) and NF155. They were first described by Davis et al., which also showed that the smaller isomorph

lacks a certain extracellular domain called Mucin domain (Davis et al. 1996). The larger isomorph, NF186 localized strongly at the nodes of Ranvier, while NF155 was primarily expressed by OLs (Collinson et al., 1998). Apart from the interaction of Neurofascin with the cytoskeletal elements, further research showed that it can also contact sodium channels via its extracellular domain (Sherman et al., 2005). The same study also revealed that Nfasc$^{-/-}$ mice did not survive past the first postnatal week, lacking paranodal junctions and node formation, highlighting the indispensability of Nfasc expression for CNS function. Further studies revealed that while loss of NF155 disrupted paranodal structure, it did not affect the clustering of sodium channels at the node of Ranvier. On the other hand, loss of NF186 severely impacted sodium cluster and AnkyrinG localization. (Pillai et al., 2009; Thaxton et al., 2011; Zonta et al., 2008). Finally, another study showed that neuron-specific loss of NF186 affects the localisation of several nodal components and disrupts paranodes (Desmazieres et al., 2014).

These results, studying major molecular components of the paranodes indicated that while paranodal junction maintenance is overall important for survival, they were not the main mechanism by which nodal components are restricted to the nodes of Ranvier.

Shifting our attention to the axonal cytoskeleton, βIV-spectrin is known to be important for sodium channel clustering via its interaction with AnkyrinG at the nodes of Ranvier (Komada & Soriano, 2002). However, βIV-spectrin has been recently shown to be instead important for long term nodal maintenance but not for sodium channel clustering itself (Liu et al., 2020). AnkyrinG, the main Ankyrin of the node of Ranvier (Kordeli et al., 1995), has also been shown to be an important mediator for nodal clustering, as mice that lack AnkyrinG, fail to properly localise both sodium channels and NF186 (Zhou et al., 1998). In a more recent study, lack of AnkyrinG did not affect sodium channel localisation and node formation, as AnkyrinG's loss can be compensated by expression of AnkyrinR. However, when both ankyrins were genetically ablated, sodium channels were absent from nodes of Ranvier and this led to premature lethality of animals by the end of the first postnatal week (Ho et al., 2014). This result is remarkably similar to the phenotype observed in

Nfasc$^{-/-}$ mutants, where loss of NF186 led to sodium channel and AnkyrinG loss from nodes (Pillai et al., 2009; Thaxton et al., 2011; Zonta et al., 2008). Therefore, there seems to be strong evidence that interactions between NF186 and AnkyrinG are important for sodium channel clustering and nodal organisation.

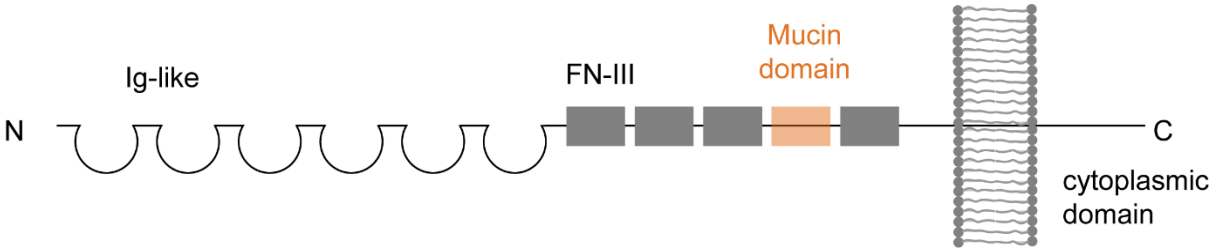

Figure 1.4 Structure of neuronal Neurofascin

Illustration depicting neuronal Neurofascin structure, having as template the zebrafish protein Nfasca. The extracellular part of the protein consists of six Ig-like domains, four fibronectin-III-like domains and the Mucin.

NF186 is a transmembrane adhesion molecule, consisting of a large extracellular domain that can be subdivided in 6 Ig-like domains, 4 fibronectin-III-like domains and the Mucin domain (Davis et al. 1996). NF186 also has a transmembrane domain and the cytoplasmic tail, which is responsible in binding AnkyrinG and the cytoskeleton (Figure 1.5). Apart from the cytoskeleton, NF186 is known to interact with brevican in the ECM (Hedstrom et al., 2007) and with sodium channels via its extracellular domain (Ratcliffe et al., 2001).

To summarise, there is a generally thorough understanding of the molecular composition of nodes of Ranvier as well as of the contribution of these molecules to overall nervous system function. Paranodal junctions are important for overall maintenance, but dispensable for clustering of nodal components at the node of Ranvier. On the other hand, AnkyrinG and NF186 seem to stand out, as their loss disrupts the localisation of other nodal components. Further investigation is needed to provide information on how these nodal proteins assemble to form the node of Ranvier *in vivo*, prior, during and after myelination.

1.5 Regulation of node positioning along individual axons

While the formation of nodes of Ranvier has been studied extensively, a largely understudied area is the regulation of node positioning along individual axons. It is well described that myelin sheath length (internode distance) can affect conduction velocity (Brill et al., 1977).

Some studies suggest that internode distance is regulated only by intrinsic OL mechanisms (Bechler et al., 2015). It is known that individual oligodendrocytes can make a limited amount of myelin sheaths (10-30 sheaths per cell, as reported in zebrafish) with highly variable lengths both within individual cells as well as between different cells (Czopka et al., 2013; Neely et al., 2020), (Figure1.6). These differences in sheath length, even sheath made by individual cells, are thought to be the main regulator of node positioning in an oligodendrocyte-specific manner.

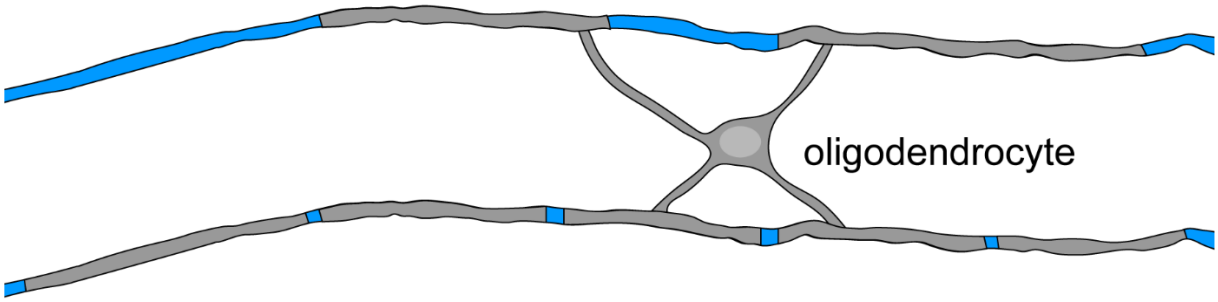

Figure 1.5 Individual oligodendrocytes make sheaths of variable lengths.

Schematic showing how individual oligodendrocytes can myelinate multiple axons with sheaths of variable length. At the same time, not all axons are myelinated equally.

However, there is also heterogeneity between axons on the patterns of myelin that covers them. Myelin is not regularly distributed along the axons, but instead forms shorter or longer segments. One striking example of this discrepancy is the axons of the gerbil auditory system (globular and spherical bushy cells), which show a stereotypical myelination pattern, with myelin segments along axons shortening the closer one gets to the axonal terminus. This myelination pattern is necessary for precise AP arrival (Ford et al., 2015). Moreover, some cortical neurons are shown to be myelinated discontinuously, being only covered by individual sheaths (Tomassy et al., 2014).

Importantly, it is also known that the same oligodendrocytes can participate in the formation of different patterns by myelinating different axons (Hughes et al., 2018)

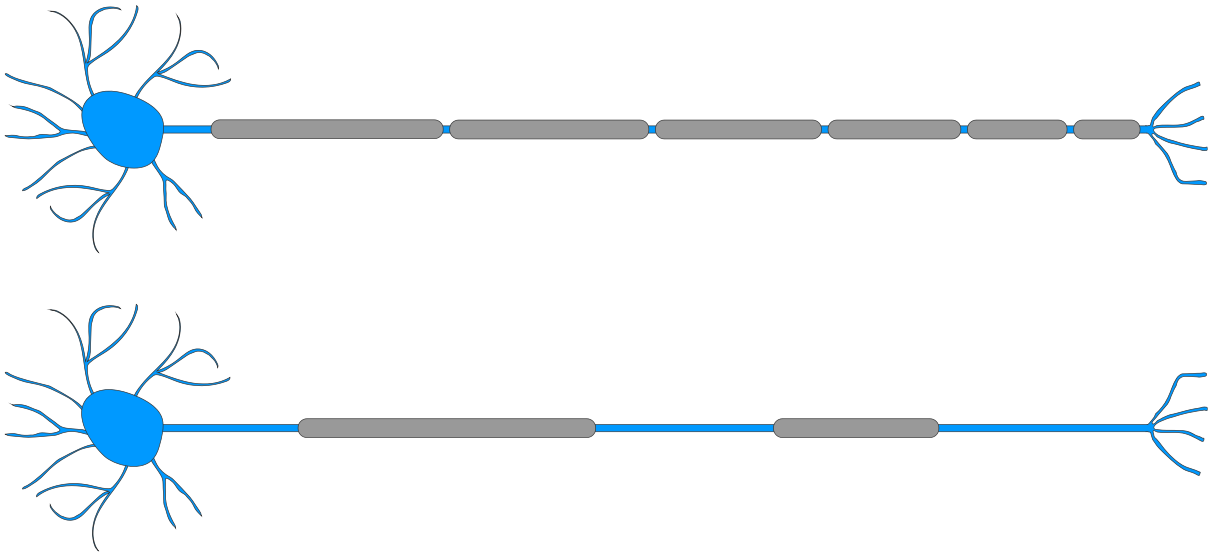

Figure 1.6 Individual axons can show variable and distinctive myelination patterns.

Schematic showing two examples of distinctive myelin patterns (top) in the gerbil auditory system and (bottom) in the murine cortex.

It is difficult to envision a mechanism that secures the formation of such stereotypic patterns by locally heterogenous OL populations that can inherently make longer or shorter sheaths in different brain regions. An alternative possibility would be that these neurons can intrinsically, at least partially, guide myelin deposition along their length. Two recent studies published back-to-back, have confirmed that neuronal activity can indeed affect myelin sheath length at the local level (Baraban et al., 2018; Krasnow et al., 2018).

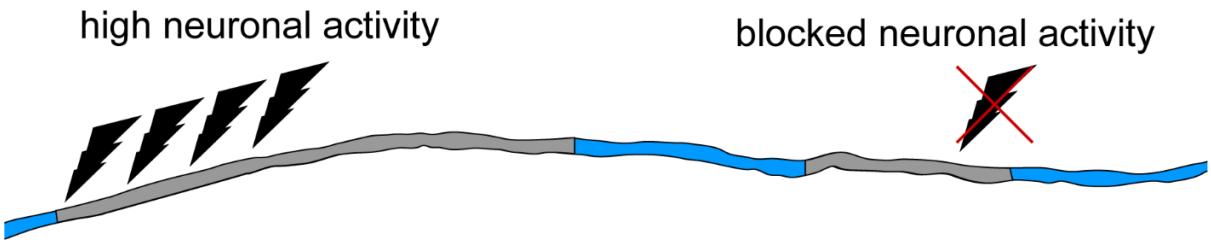

Figure 1.7 Effect of neuronal activity on individual sheaths' length.

Schematic showing how increased neuronal activity leads to sheath lengthening while blocking neuronal activity halts lateral sheath growth (modified from Miller et al. 2017).

Another important line of evidence that supports the hypothesis of neuronal contribution in myelin deposition regulation derives from experiments in which, sparsely myelinated axons were demyelinated. In a study performed by our group, we found instances when upon ablation of individual myelin sheaths, the subsequent remyelination faithfully re-established the pre-ablation status quo, with new myelin perfectly replacing the lost myelin (Auer et al., 2018). In a more recent study, performing a similar experiment in the murine cortex also showed that patterns of myelination are likely to get restored (Snaidero et al., 2020). The persistence of myelination patterns even after myelin degeneration and replacement, could indicate the presence of structural "memory" on the axon, that can guide the placement of new myelin to recapitulate the pre-manipulation state.

Voltage-gated sodium channels are known to form clusters along unmyelinated axons *in vitro* (S. A. Freeman et al., 2015; M. Kaplan et al., 1997; M. R. Kaplan et al., 2001) and in histological analyses of murine brain slices (S. A. Freeman et al., 2015). OL-secreted factors, but without direct contact with OLs, have been shown to be necessary for cluster formation (S. A. Freeman et al., 2015)). Such protein clusters can constitute pre-myelination axonal cues that pre-pattern the axonal surface in preparation for myelination. Since nodal position defines sheath length, the presence of such clusters constitutes a promising way in which individual axons can intrinsically regulate their myelination pattern.

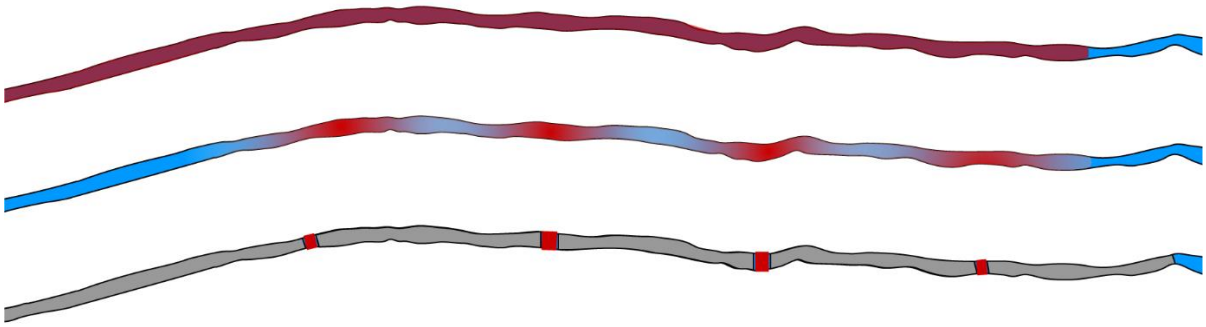

Figure 1.8 Clustering of nodal proteins prior to myelination could regulate node position.

Theoretical contribution of clustered nodal proteins to the formation of the final node positioning.

While the prevailing view is that the length of myelin sheaths is an entirely intrinsic property of OLs, the observation of highly complex myelination patterns together with the discovery that neuronal activity can directly affect sheath length has initiated an investigation of whether neuronal mechanisms that regulate sheath length and thus node positioning exist. Nodal proteins are known to cluster *in vitro* and *in vivo* along individual axons in the absence of myelin and could serve as local cues for future node positioning. However, it is not known to what extent this is possible, prompting *in vivo* experiments to answer that question.

1.6 Demyelination-induced changes to the nodes of Ranvier.

The intricate structure that forms and supports nodes of Ranvier raises the question: *What happens to the complex molecular network of nodal components, following demyelination?* Recent evidence produced by us and by others (Auer et al., 2018; Snaidero et al., 2020) has shown that myelination patterns of individual axons are likely to be restored following demyelination and remyelination. These observations suggest that the axon contains some form of "molecular blueprint" that is retained upon myelin loss and can guide the deposition of new myelin in order to replicate the pre-damage myelination pattern. A possible candidate location for the identification of such molecules is the node of Ranvier, as it contains components that are highly organised and interact with both the axonal cytoskeleton and the ECM.

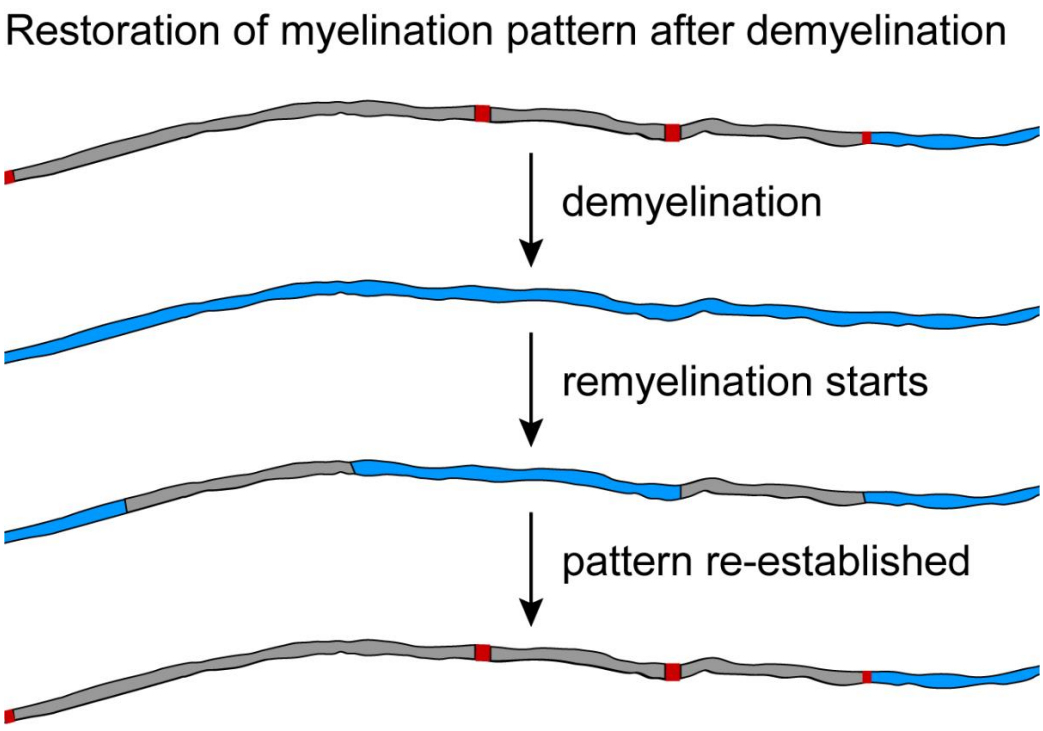

Figure 1.7 Putative restoration of myelination pattern after demyelination.

Illustration depicting the timeline of events that could lead to the restoration of myelin pattern (grey) along an individual axon (cyan) following demyelination. Nodes of Ranvier (red) are potential hotspots that could guide the restoration process.

Several studies have focused into changes in nodal component distribution upon myelin loss. One study (Oluich et al., 2012), showed that nodal length increased in lesions upon OL ablations in the spinal cord and that AnkG diffused along longer stretches flanked by paranodal labelling. Other studies, (Craner et al., 2003, 2004) showed that voltage-gated sodium channels 1.2 and 1.6 appear diffused within demyelinated lesions in Experimental Autoimmune Encephalitis (EAE) in the spinal cord and the optic nerve. In (Craner et al., 2004; Howell et al., 2006), looking again into MS lesions, the researchers found that Nfasc-186 localization is disrupted upon local demyelination, with Nfasc-186+ regions appearing elongated. However, in these experiments, the labelling of Nfasc-186 does not appear fully diffused, but rather cluster-like. Moreover, the researchers found that the localization of Nfasc-186 is restored upon remyelination.

As reviewed extensively in Lubetzki et al., while the above studies focus primarily on white matter, in grey matter axons, sodium channels seem to remain clustered upon demyelination. Indeed, recent evidence have been published that support this hypothesis and show the persistence of isolated nodal components following demyelination in the cortex (Lubetzki et al., 2020; Orthmann-Murphy et al., 2020). Similarly, sodium channel accumulations were also reported in dysmyelination models (like *jimpy* mice), on axons that lack myelin. Lubetzki et al. also raises the possibility that nodal clusters can facilitate signal transduction via microsaltatory conduction (a partially functional saltatory conduction) in pre-myelination settings. It is conceivable that clustered nodal remnants could also enable microsaltatory conduction, partially rescuing the conduction halt that demyelination imposes (Lubetzki et al., 2020).

Overall, there are several lines of evidence suggesting that certain molecules remain clustered upon demyelination while others diffuse out into the axon. Generally, histological analyses are limited in their assessment of dynamic processes like demyelination and remyelination, because of their inability to longitudinally follow individual structures. Moreover, the complexity of nodes of Ranvier in terms of sheer number of potential target proteins further increases the difficulty for such

experiments. It is thus important to characterise the potential fates of nodal proteins *in vivo*, in order to describe their dynamics and potential contribution in regulating remyelination.

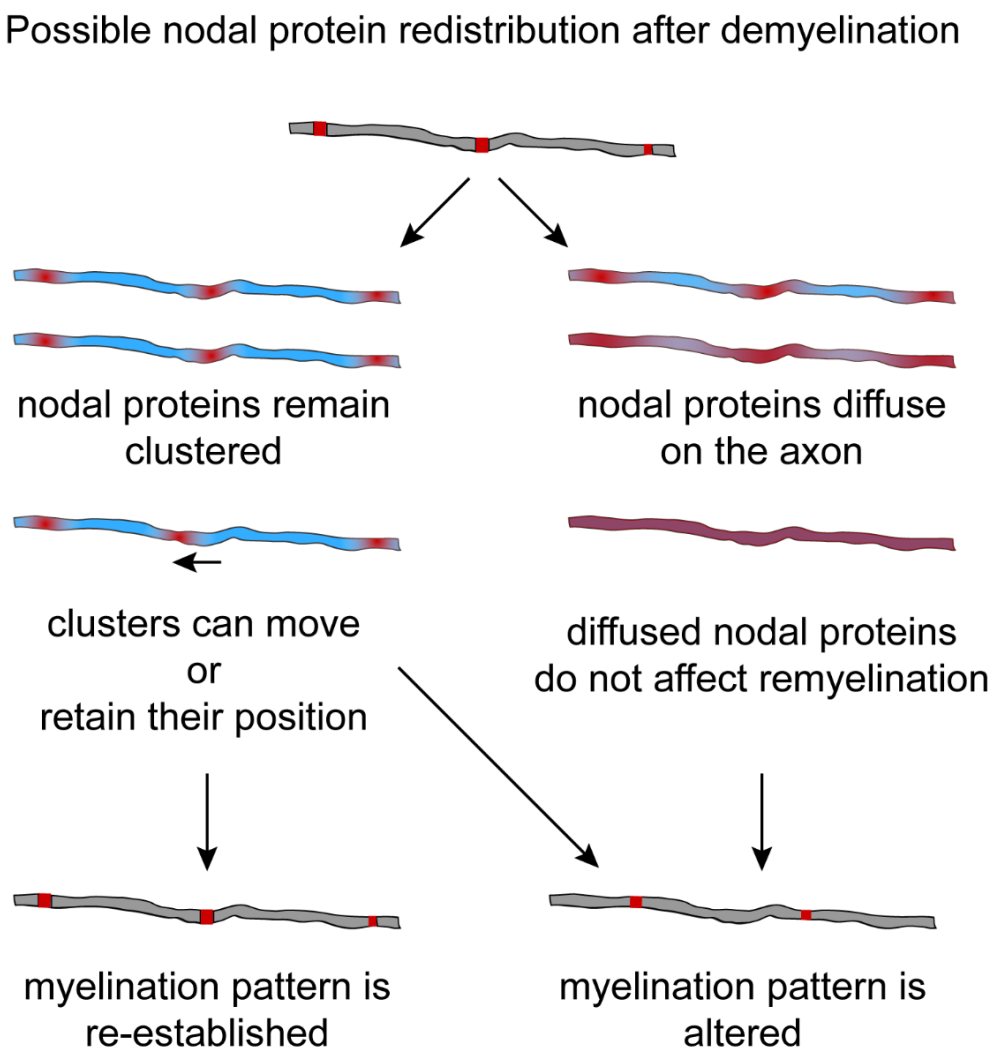

Figure 1.8 Nodal component fate following demyelination.

Illustration depicting the potential dynamics of nodal molecules along an individual axon after demyelination. Nodal proteins can conceptually diffuse along the axon or remain clustered. The nodal clusters can either retain their position to serve as hallmarks for remyelination or they can be motile leading to an altered coverage pattern after remyelination.

1.7 Aim of the project.

Oligodendrocytes facilitate rapid and precise signal transduction in the CNS by wrapping the axons in sheaths of a lipoproteinic substance called myelin that isolates the axons electrically. Moreover, oligodendrocytes via the myelin sheaths provide the axons with necessary metabolites. The differentiation of oligodendrocytes and axonal myelination does not stop but continues throughout life. Pre-existing myelin can also remodel in length. In disease, remyelination does occur, but for function to be fully restored, faithful remyelination of the demyelinated axons is essential.

The dynamics of remyelination following myelin damage are not yet fully described with regard to oligodendrocyte differentiation. Moreover, how newly differentiated oligodendrocytes select axon targets in a system that contains both demyelinated and unmyelinated axons is not yet described.

Lastly, since myelination often requires the formation of highly specific patterns of internodal distances, it is important to describe how myelin is deposited along the length of individual axons in order for these patterns to be established and for the nodes of Ranvier to form in the correct positions.

In order to address these gaps of knowledge my thesis has the following aims:

1. To establish reagents and assays in order to study myelination and oligodendrogenesis dynamics in developing zebrafish.

2. To address the position where and time when new oligodendrocytes differentiate following ablations as well as to identify their axon targets for myelination.

3. To understand how future node positioning along individual axons is regulated by glia and neurons.

4. To assess whether node position, once established, can remodel following local axonal demyelination.

2. Materials and Methods

2.1 Cloning

Cloning of constructs for transgenic expression was done in collaboration with Dr. Tim Czopka, Wenke Barkey, Franziska Auer, Tobias Hoche and Roberta Marisca.

For the 5' entry clone **p5E_mfap4**, an 1.5kb part of the mfap4 locus was amplified using the primer pair attB4_mfap4 and attB1R_mfap4 from genomic AB wildtype DNA (Walton et al., 2015). The product of this PCR was recombined into the pDONRP4-P1R vector via BP clonase to generate the p5E_mfap4.

For the middle entry clone **pME_memCerulean**, the sequence was amplified from a third plasmid using the primers attB1_memC/YFP_F and attB2R_memC/YFP_R. The resulting product was recombined with the pDONR221 vector using BP clonase to generate the pME_memCerulean.

For the middle entry clone **pME_tagCFP**, the sequence was amplified from a third plasmid using the primers attB1_tagCFP_F and attB2R_tagCFP_R. The resulting product was recombined with the pDONR221 vector using BP clonase to generate the pME_tagCFP.

For the middle entry clone **pME_KillerRed**, the sequence was amplified from a third plasmid using the primers attB1_KillerRed_F and attB2R_KillerRed_R. The resulting product was recombined with the pDONR221 vector using BP clonase to generate the pME_KillerRed.

To generate the middle entry clone **pME_Nfasca-nostop**, the coding sequence of the zebrafish Neurofascin-a gene (*nfasca* - ENSDART00000112655.3) was amplified from AB wildtype zebrafish Cdna, using the primer combination attB1_Nfasca_F and attB2R_Nfasca_nostop_R to also remove the stop codon. The PCR product was recombined with the pDONR221 vector using BP clonase to generate the pME_Nfasca-nostop.

For the middle entry clone **pME_EYFP-NaV-II-III**, a 1.3 kb fragment encoding for the II-III region of the Nav1.2 gene (Garrido et al., 2003), encoded in zebrafish by the scn1lab gene (exons 16-18 -

ENSDART00000151247.3) was commercially synthesised (BioCat). The synthesised fragment was used as a template for a PCR with the primers XhoI-NaV-II-III_F and XbaI-NaV-II-III_R. The product was then cloned, using the two restriction sites introduced by the primers, into a pCS2+ vector that contained EYFP, with its stop codon removed between the restriction sites BamHI and EcoRI. The resulting plasmid pCS2+_EYFP_NaV-II-III was then amplified using the primers attB1_YFP_F and attB2R-NavNaV-II-III_R and the product was recombined with the pDONR221 vector using BP clonase to generate the pME_EYFP-NaV-II-III.

For the middle entry clone **pME_EYFP-cntn1a**, 2.6kb of the zebrafish contactin1a gene (ENSDART00000170348.2) was amplified using the primer pair EcoRI_cntn1a_F and XbaI_cntn1a_R and was cloned without the coding sequence for the amino acids 1-45 (which code for a signal peptide for secretory pathway). into a pCS2+ vector that contained EYFP fused to the secretory pathway signal peptide of zebrafish CD59 protein (ENSDART00000126737.4) between BamHI and EcoRI sites to create pCS2+_sigpepEYFP-cntn1a. This plasmid was then used as a PCR template using the primers attB1_sigpepEYFP_F and attB2R_cntn1a_R. The resulting product was recombined with the pDONR221 vector using BP clonase to generate the pME_EYFP-cntn1a.

For the 3' entry clone **p3E_EYFP**, the sequence was amplified from a third plasmid using the primers BamHI_C/YFP_F and EcoRI_C/YFP_R. The product was then digested with BamHI and EcoRI and was purified using a PCR purification kit (Qiagen). The resulting digested sequence was cloned into a pCS2+ vector also digested with BamHI/EcoRI. The resulting plasmid was used as a template for the PCR amplification of EYFP-pA using the primers attB2_C/YFP_F and attB3R_pA_R and was then cloned into the vector pDONR_P2P3R with a BP-reaction

To make the expression construct **pTol2_mbp:memCerulean**, p5E_mbp (Almeida et al., 2011), pME_memCerulean and the plasmids p3E-pA and pDestTol2_pA of the Tol2kit (Kwan et al., 2007) were recombined using a multisite LR reaction.

To make the expression construct **pTol2_mbp:KillerRed**, p5E_mbp (Almeida et al., 2011), pME_KillerRed and the plasmids p3E-pA and pDestTol2_pA of the Tol2kit (Kwan et al., 2007) were recombined using a multisite LR reaction.

To make the expression construct **pTol2_mbp:memRFP**, p5E_mbp (Almeida et al., 2011), pME_ memRFP, and the plasmids p3E-pA and pDestTol2_pA of the Tol2kit (Kwan et al., 2007) were recombined using a multisite LR reaction.

To make the expression construct **pTol2_cntn1b:tagCFP**, p5E_cntn1b (Czopka et al., 2013), pME_tagCFP and the plasmids p3E-pA and pDestTol2_pA of the Tol2kit (Kwan et al., 2007) were recombined using a multisite LR reaction.

To make the expression construct **pTol2_huC:tagCFP**, p5E_huC (Mensch et al., 2015), pME_tagCFP and the plasmids p3E-pA and pDestTol2_pA of the Tol2kit (Kwan et al., 2007) were recombined using a multisite LR reaction.

To make the expression construct **pTol2_cntn1b:Nfasca-EYFP**, p5E_cntn1b (Czopka et al., 2013), pME_Nfasca-nostop, p3E_EYFP and pDestTol2_pA of the Tol2kit (Kwan et al., 2007) were recombined using a multisite LR reaction.

To make the expression construct **pTol2_cntn1b:EYFP-cntn1a**, p5E_cntn1b (Czopka et al., 2013), pME_EYFP-cntn1a, and the plasmids p3E-pA and pDestTol2_pA of the Tol2kit (Kwan et al., 2007) were recombined using a multisite LR reaction.

To make the expression construct **pTol2_UAS:EYFP-cntn1a**, p5E_UAS (Kwan et al., 2007), pME_EYFP-cntn1a, and the plasmids p3E-pA and pDestTol2_pA of the Tol2kit (Kwan et al., 2007) were recombined using a multisite LR reaction.

To make the expression construct **pTol2_cntn1b:EYFP-NaV1.2-II-III**, p5E_cntn1b (Czopka et al., 2013), pME_EYFP-NaV-II-III, and the plasmids p3E-pA and pDestTol2_pA of the Tol2kit (Kwan et al., 2007) were recombined using a multisite LR reaction.

To make the expression construct **pTol2_mfap4:memCerulean**, p5E_mfap4, pME_memCerulean, and the plasmids p3E-pA and pDestTol2_pA of the Tol2kit (Kwan et al., 2007) were recombined using a multisite LR reaction.

Table 2.1 Primer list

Primer name	Primer sequence
attB4_mfap4	GGGGACAACTTTGTATAGAAAAGTTGGCGTTTCTTGGTACAGCTGG
attB1R_mfap4	GGGGACTGCTTTTTTGTACAAACTTGCTTCTCACTCTCTCCTCAAC
attB1_memC/YFP_F	GGGGACAAGTTTGTACAAAAAAGCAGGCTGCCACCATGCTGTGCTGC
attB2R_memC/YFP_R	GGGGACCACTTTGTACAAGAAAGCTGGGTCTTACTTGTACAGCTCGTCCATGC
attB1_tagCFP_F	GGGGACAAGTTTGTACAAAAAAGCAGGCTGCCACCATGAGCGGGGG
attB2R_tagCFP_R	GGGGACCACTTTGTACAAGAAAGCTGGGTTTAGCGGTACAGCTCGTCCATG
attB1_KillerRed_F	GGGGACAAGTTTGTACAAAAAAGCAGGCTGCCACCATGGGATCCGAGGGCGGCCCCGCC
attB2R_KillerRed_R	GGGGACCACTTTGTACAAGAAAGCTGGGTCTAATCCTCGTCGCTACCGATGG
attB1_Nfasca_F	GGGGACAAGTTTGTACAAAAAAGCAGGCTGCCACCATGTGGACACAGAGGCGGTG
attB2R_Nfasca_nostop_R	GGGGACCACTTTGTACAAGAAAGCTGGGTCTGCCAAAGAGTAGATGGCATTG
XhoI-NaV-II-III_F	CACACTCGAGATATGAGCTCTTTCAGTGCCGA
XbaI-NaV-II-III_R	CATCTAGATTAGATAAAGCAGGTTTTCCTGA
attB1_YFP_F	GGGGACAAGTTTGTACAAAAAAGCAGGCTGCCACCATGGTGAGCAAGGGCGAGGAG
attB2R-NavNaV-II-III_R	GGGGACCACTTTGTACAAGAAAGCTGGGTCTTAGATAAAGCAGGTTTTCCTGA
EcoRI_cntn1a_F	CACAGAATTCCCGGTGTTCGAGGAGCAGC
XbaI_cntn1a_R	CATCTAGATCAGAGCATCAGAGTCCAGAG
attB1_sigpepEYFP_F	GGGGACAAGTTTGTACAAAAAAGCAGGCTGCCACCATGAAAGCTTCTGTCGGAG
attB2R_cntn1a_R	GGGGACCACTTTGTACAAGAAAGCTGGGTCTCAGAGCATCAGAGTCCAGAG
BamHI_C/YFP_F	GATGGATCCATGGTGAGCAAGGGCGAG
EcoRI_C/YFP_R	GACGAATTCTTACTTGTACAGCTCGTCCATGC
attB2_C/YFP_F	GGGGACAGCTTTCTTGTACAAAGTGGATATGGTGAGCAAGGGCGAG
attB3R_pA_R	GGGGACAACTTTGTATAATAAAGTTGAAAAAACCTCCCACACCTCCC

Colour code: att recombination site, restriction site, Kozak sequence, base to avoid frame shift.

2.2 Transgenic animals

All animal experimentation was performed in accordance with the animal welfare regulations, approved by the local animal welfare authorities. Animals were maintained at a stable temperature of 28.5°C with a 14h light / 10h dark cycle. Table 2.2 lists all the transgenic lines used.

Table 2.2 Transgenic zebrafish lines used.

Transgenic Line	Reference
Tg(mbp:KillerRed)	(Auer et al., 2018)
Tg(mbp:memCerulean)	(Auer et al., 2018)
Tg(mbp:memRFP)	(Auer et al., 2018)
Tg(mbp:EGFP-CAAX)	(Almeida et al., 2011)
Tg(mbp:nls-EGFP)	(Karttunen et al., 2017)
Tg(mfap4:memCerulean)	generated
Tg(cntn1b(3kb):KalTA4)	Donated by the Lyons lab
Nfasca$^{\Delta 28/\Delta 28}$	generated

2.3 CRISPR/Cas9 mediated mutagenesis in the *nfasca* gene

Nfasca$^{\Delta 28/\Delta 28}$ mutant zebrafish were generated using CRISPR/Cas9 genome editing. 1-cell stage, AB wildtype embryos were injected with 12.5 ng/µl sgRNA and 300 ng/µl Cas9-encoding mRNA. The sgRNA (Table 2.3) was designed using CHOPCHOP (Labun et al., 2016) and was generated as described (Hruscha et al., 2013). First generation animals (F1) were sequenced for indel mutations and one individual with a 28bp deletion 5' to the target site was selected to raise Nfasca$^{\Delta 28/+}$. Subsequent generations and all samples from experiments involving *nfasca* mutants were genotyped, using the primers shown in Table 2.3.

Table 2.3 gRNA and genotyping primers.

Oligonucleotide name	Sequence
Nfasca_guide#3 (target underlined)	AAAGCACCGACTCGGTGCCACTTTTTCAAGTTGATAACGGACTAGCCTTATTTTA ACTTGCTATTTCTAGCTCTAAAACCTGGAGCCAAACGGTGTCCTCTATAGTGAGT CGTATTACGC
Nfasca_geno_F	CTGTGGAGTTTTACACCAAGG
Nfasca_geno_R	GCTTACCTGTGTGGTACTGG

2.4 mRNA synthesis and injection

All insertion of genetic material for transient (somatic) expression or generation of transgenic lines was mediated by Tol2 transposase by the used of the Tol2kit (Kwan et al., 2007). In order to synthesise the Tol2 transposase mRNA, the transposase-encoding plasmid was linearised using the restriction enzyme NotI (New England BioLabs). The product of the digest was subsequently isolated using a PCR purification kit (Qiagen). The mMessage mMachine SP6 transcription kit (Invitrogen) was used for the *in vitro* transcription. The transcript was then purified using an RNA clen up kit (Qiagen). mRNA concentration was then measured and the Tol2 transposase mRNA was stored at -80°C.

Injections of the constructs of choice were conducted as already described (Vagionitis & Czopka, 2018). To summarize, 1-cell stage fertilised embryos were injected with 1nl of solution containing 20-30 ng/µl plasmid DNA, 25-60 ng/µl transposase mRNA and 1% phenol red (Sigma Aldrich).

For generation of new transgenic lines, injected embryos were screened using a stereo-dissecting microscope (Nikon SMZ18) at 3-4 dpf for expression of the transgene and positive embryos were raised to adulthood (F0). Then these F0 transgenic animals were outcrossed to wildtype ones and their offspring were again screened for germline transmission in order to raise stable transgenic lines.

2.5 Mounting of larvae and *in vivo* microscopy

Transgenic fish were screened for expression of the desirable fluorescent proteins using a stereo fluorescent microscope (Nikon SMZ18). Anaesthetised fish (incubated in Danieau's buffer containing 0.2 mg/ml MS-222 for 5-10 minutes) were embedded in 1% ultrapure low melting point agarose (Invitrogen), as already described (Vagionitis & Czopka, 2018). The standard orientation of the embedded fish was head-left, unless the cell of interest was in the contra-lateral side of the spinal cord. In these cases, the embedding orientation was reversed (head-right).

For imaging of embedded zebrafish embryos and larvae a confocal laser scanning microscope (Leica TCS SP8) was used. During *in vivo* microscopy, confocal z-stacks were acquired as 8bit or 12bit images with a pixel size ranging between 76 and 114 nm and a z-spacing of 1µm using a Fluotar VISIR 25x/0.95 WATER immersion objective. Images are shown as lateral views of the zebrafish spinal cord with the anterior to the left and dorsal to the top of the image. To avoid photobleaching during acquisition of fast, time-lapse images, an 8kHz resonant scanner was used.

After imaging, fish were released from the agarose and were either euthanised using an overdose of MS-222 or were placed in Danieau's buffer. For experiments conducted after 5 days post fertilisation (dpf) larvae were kept at a stable temperature of 28.5°C with a 14h light / 10h dark cycle and were fed with Sera Micron as well as Paramecia.

2.6 Laser ablations of KR-expressing oligodendrocytes

KillerRed expressing oligodendrocytes were ablated using a MaiTai DeepSee HP (Newport/Spectra Physics) 2-photon laser and a 25x 1.05 NA MP (XLPLN25XWMP) water immersion objective on an Olympus FV1000/MPE microscope. Using the live mode of the microscope, cells of interest were identified using a 559nm laser. A line region of interest (ROI) was drawn along the major axis of the soma and the 2-photon laser was used to bleach along this ROI set at 770nm (1.75W output) for 0.5 seconds.

2.7 Immunohistochemistry and confocal microscopy of tissue sections

Immunohistochemistry on spinal cord cross-sections was performed according to a published protocol (Vagionitis et al. 2021).

Confocal z-stacks of zebrafish spinal cord cross-sections were acquired as 12bit images with a pixel size of 36 nm, z-spacing of 0.19 µm and pinhole set to 0.8AU using an HC PL APO CS2 63x/1.20 WATER immersion objective.

2.8 Whole-mount immunohistochemistry

Whole-mount immunohistochemistry on zebrafish larvae or embryos was performed as already described (Vagionitis et al. 2021).

Microscopy on whole-mount stained zebrafish was performed similarly to *in vivo* microscopy (see paragraph 2.5).

2.9 Transmission Electron Microscopy

For the preparation of zebrafish samples for electron microscopy (EM), a previously published method was used (Czopka & Lyons, 2011). In short, larval zebrafish were euthanised with an overdose of MS-222 (15 mM) and fixed in a solution containing 2% glutaraldehyde (GA), 4% PFA and 0.1 M sodium cacodylate, pH 7.4. Microwave stimulation was performed in order to accelerate fixation and improve its uniformity (Czopka & Lyons, 2011). Sample-containing glass vials were placed in a 4°C water bath and they were first irradiated 2 times with 100W microwaves for 1 minute, each followed by 1 minute of cool-down. Then the samples were irradiated 5 times with 450W microwaves for 20 seconds, each followed by 20 seconds of cool down. A thermometer allowed for monitoring of the temperature of the water bath for the whole fixation protocol. Samples when then kept in the same fixative solution at 4°C until further processing.

Samples were subsequently transferred to the EM hub of the Munich Cluster for Systems Neurology (SyNergy) at the German Centre for Neurodegenerative Diseases (DZNE), Munich, where they were prepared by our collaborator, Dr. Martina Schifferer. Secondary fixation, en bloc stain, dehydration and embedding were done according to previously published protocols (Czopka & Lyons, 2011), (Cunha et al., 2020).

Blocks carrying the fixed samples were trimmed in a trimming device (Leica EM Trim). Trimming was done until the level of the somite segment 17, which was in the centre of the region of interest and was easily identifiable due to the presence of anatomical features of the larva (cloaca). Samples were subsequently sectioned in 50-70nm sections using an ultramicrotome (Leica EM UC7). Sections were collected on formvar-coated, copper grids. For each sample, sections were taken from 3 regions, at positions 0, +75µm and +150µm, with 0 being the position of somite 17 and the + sign indicates a more anterior position relative to somite 17. Section-carrying grids were then contrasted by incubation with 1% uranyl acetate (UA) for 30 minutes at RT, followed by three washes with distilled water. Samples were then incubated with lead citrate solution (Reynolds' stain - (Venable & Coggeshall, 1965). Following 4 washes with distilled water and a drying step using Whatman paper, sample-carrying grids were left to dry before being imaged. Samples were transferred into a JEM1400+ (JEOL) electron microscope equipped with a Ruby camera. Images were acquired using the TEM Center and ShotMeister.

2.10 (+)-JQ1 treatment

(+)-JQ1 was used at a final concentration of 2 µM, diluted in Danieau's buffer and 1% DMSO. 2 dpf embryos were treated either to the (+)-JQ1 containing solution or to a control solution containing 1% DMSO in Danieau's buffer. Treatment was stopped at 5 dpf after the fish were imaged.

2.11 Image analysis and processing

Analysis of confocal images was conducted either using ImageJ (FIJI), LasX (Leica) and Imaris (Bitplane). Brightness adjustments and registration of images was done using FIJI (StackReg plugin for registration). LasX was used to adjust the orientation of the xyz volumes acquired and export re-oriented images, when needed. For deconvolution of confocal images, the Huygens Essentials v16.10 1p2 was used (Scientific volum imaging, the Netherlands).

The FilamentTracer tool of Imaris 8.4.2 (Bitplane) was used for the reconstruction of axon morphology as well as node positioning. Individually labelled axons were reconstructed in a semi-automated fashion, by tracing automatically the axon of interest starting at the soma, while axon diameter was reconstructed automatically. For the reconstruction of nodes of Ranvier, the tool was used on its automatic mode. Finally, the resulting traces were superimposed in order to more clearly visualise nodal spacing along individual axons.

For the analysis of electron micrographs, the LLP Viewer (System in Frontier inc.) was used. Through the LLP Viewer, montages of the spinal cord cross-sections were corrected for incorrect positioning of individual images and the resulting regions of interest were then exported as TIF files. Brightness adjustment of the resulting TIF files was done in FIJI, while Photoshop CC (Adobe) was used to create pseudo-coloured images in order to highlight specific structures of interest (both on electron micrographs and confocal images).

Measurements of fluorescent intensity as well as various measurements of length were conducted in FIJI (including the measurement of axon diameter from electron micrographs). Finally, all figure panels were assembled and annotated using Illustrator CC (Adobe).

2.11 Data analysis

Oligodendrocyte number measurements

For cell number quantification, transgenic lines expressing a fluorescent protein either in the cytoplasm or carrying a nuclear localisation signal were used. For the analysis of timelines, images from 6 to 13 dpf were taken centred around somite segment 17 and included the entire width of the spinal cord. Cells were counted within an area of the field of view, demarcated by two dorsal oligodendrocytes (for the experiments of oligodendrocyte ablations, the two cells were the two surviving OLs at the borders of the lesion – for control fish, they were chosen randomly as 2 cells close to either edge of the field of view). This method of using two local landmarks to define the region of interest ensures that fish growth will not factor in the result. Cell numbers were normalised to 150 µm of length of the spinal cord and the resulting cell density was used for comparison between animals. Cells were annotated during the analysis as located in the ipsilateral side (closer to the objective during microscopy), the contralateral side or as being in the grey matter, when the OL somata were localised in the centre of the spinal cord. Newly added oligodendrocyte numbers were calculated as the difference of the number of cells at the end of the timelapse (13 dpf) minus the number of cells at 1 day post-ablation (1 dpa – 7 dpf).

Axon and neurite number measurements

For measuring the numbers of myelinated axons, electron micrographs of the spinal cold were divided into halves and myelinated axons were easily identified and counted. The ventral spinal cord was not assessed, as not being the focus of the study. Axons were then divided into two groups, those who are located in the dorsal tract and those we are in the lateral side of the spinal cord.

For measuring the numbers of neurites, confocal images of the spinal cord with neurites transiently labelled, in the proximity of an OL soma were traced in Imaris (Bitplane) as already described. Traced axons were measured before and after the ablation of the neighbouring oligodendrocyte.

Cell body fragmentation time quantification

For measuring the oligodendrocyte fragmentation time, a transgenic line with all oligodendrocytes expressing the photosensitiser KillerRed were used. Timelapses of spinal cord regions of interest

following OL ablations were analysed, and the time of cell fragmentation was assessed as the time of the loss of the bleached soma demarcation by the fluorescent protein (KillerRed).

Macrophage recruitment time quantification

For measuring the macrophage recruitment time, a transgenic line with all oligodendrocytes expressing the photosensitiser KillerRed and all phagocytes labelled was used. Timelapses of spinal cord regions of interest following OL ablations were analysed and the time of recruitment of the first macrophage to enter the lesion site was noted.

Macrophage number measurements

For measuring the macrophage recruitment time, a transgenic line with all oligodendrocytes expressing the photosensitiser KillerRed and all phagocytes labelled was used. Timelapses of spinal cord regions of interest following OL ablations were analysed, and infiltrating macrophages were measured between 0 (pre-ablation) and 5 days post ablation (dpa).

Correlative light and electron microscopy

For correlating light and electron microscopy images, electron micrographs taken at 3 positions: at somite 17, 75µm and 150µm anteriorly to somite 17 and were compared to the respective confocal image of the same area. By comparing the number and relative positioning of myelinated axons in the dorsal spinal cord as assessed by TEM and light microscopy, lesion sites were identified.

Axon perimeter measurements

Axon perimeter was measured in electron micrographs. Focusing on the dorsal tract, the 50 largest axons, by visual impression, were analysed.Regions of interest were designed using FIJI around the plasma membrane of each axon in question and the length of the ROI was then measured.

Fluorescence intensity measurements.

For the measurement of fluorescent intensities, the x line tool of Fiji was used. The line width was adjusted manually to match the thickness of the axon. Fluorescent intensity values were manually

categorised as belonging to node, cluster or myelinated areas. A single value of background fluorescence was measured and subtracted for each image. For obtaining the intensity of fluorescent markers at the nodes of Ranvier, stretches of axons at the nodes of Ranvier, 1µm-long, were measured and averaged. Fluorescence intensity values were normalised at the maximum fluorescence of the node and the peaks of several nodes were aligned.

When each partially myelinated axon was analysed, fluorescence intensity measurements were taken from one node, one myelinated stretch and the unmyelinated part of the axon. All values were normalised to the maximum intensity at the node. To obtain the fluorescent intensity traces, all values were normalised to the average fluorescence of 5µm of myelinated axon. ΔF/F was then calculated.

Measurements of internodal and intercluster distances

To measure the distance between clusters or nodes, the x line tool of Fiji was used. The distance of the first cluster/node from the soma of the analysed neuron was not measured.

For the Nfasca mutant analysis, internodal distance was measured along CoPA axons in the spinal cord of 8 and 9 dpf zebrafish and the resulting data were used to calculate the average value per animal. This allowed for comparison between wildtype and mutant animals. Image acquisition and analysis was done prior to the genotyping of the samples in question, making the analysis blind.

Node/cluster ratio calculation

For the calculation of the node/cluster ratio, two numbers were acquired. The number of clusters along an unmyelinated axon and the number of nodes along the same axon after it was myelinated. Then the number of nodes was divided by the number of clusters to obtain the node/cluster ratio per axon. Values from different axons were plotted.

Daily motility measurement for clusters and nodes

To measure the daily motility of clusters and nodes, the distance of the cluster or node from a chosen landmark within the field of view was measured over time. Daily fish growth was calculated as the

ratio of distances between two fixed landmarks within 24h. Distance of nodes or clusters from a fixed landmark was corrected by dividing with the fish growth factor. These daily measurements of distance were subtracted in order to calculate daily motility. To visualise node translocation, initial position was set to zero. Daily motility values are always positive, because the direction of movement for clusters and nodes was not analyses, so all movements are shown as absolute values.

Sheath length measurements

Sheath length was measured using the x line tool of Fiji. Sheaths were measured only when their borders were clearly visible. For the analysis of (+)-JQ1 treatment experiment, only sheaths with 0 or 1 neighbours were measured and their shape and location (dorsal and ascending) were used to verify that these sheaths formed around CoPA neurons.

For the correlation of sheath length with the presence of heminodal Nfasca-EYFP, sheaths were categorised accordingly, and their respective frequency was calculated.

Assessment of Nfasca-EYFP cluster fate

The density of Nfasca-EYFP clusters compared to the diffused localisation along unmyelinated parts of the axon without clusters rendered them easily identifiable by visual impression. Images were pasted on Illustrator CC (Adobe) one after the other and aligned to a landmark, close to the cluster of interest. If more than one cluster was analysed, images were realigned for each cluster. Images were corrected for growth in body size, measured as the percentile change in linear distance between two somata of neurons within the field of view. A box of 1-2μm was drawn over the aligned images at the position of a cluster. Only when a node or a heminode were found inside this border, it was counted as residing at the same position. Only clusters without any structural axonal elements, like axon collateral branches were analysed.

Assessment of nodal origin

For the analysis of nodal origin, images were aligned to a landmark close to the analysed node. The alignment was corrected for body growth, similarly to before. If more than one node was analysed on the same axon, the images were realigned for each node. A box, 2-3 μm wide was drawn around each node and it was used to assess whether a cluster was present at a previous timepoint in the same position, prior to myelination. As with cluster fate analysis, only nodes without axon collateral branches were analysed, as structural features of the axon could influence the deposition of myelin and thus the positioning of nodes.

2.12 Statistics

All quantifications and frequency tables were initially done in Excel (Microsoft). All statistical analysis was conducted using GraphPad Prism9 (GraphPad Software LCC). Normality tests were used to assess the Gaussian distribution of the data. In the text description of the data, all data are expressed as mean ± standard deviation (SD. For simplicity and legibility, the main text always reports mean ± standard deviation (SD). In figures, normally distributed data are expressed as mean ± standard deviation (SD), while skewed data are expressed as median with interquartile range (IQR), unless otherwise stated. Statistical testing was done appropriately according to the type of distribution of data. Normally distributed data were tested with paired or unpaired t-test or ANOVA for three or more variables. For skewed data, non-parametric tests were used (Wilcoxon matched pairs signed rank test, Mann-Whitney test or Kruskal Wallis test with multiple comparisons). For correlation, Pearson's r was calculated. P-values are always shown in the graph and written in the main text, together with the statistical test performed.

2.13 Solutions and buffers

Danieau's Buffer (30x - stock solution for 900ml)

Ingredients	Amount
NaCl (Roth)	91.52g
KCl (Roth)	1.41g
$MgSO_4$ (VWR Chemicals)	2.66g
$Ca(NO_3)_2$ (Roth)	3.83g
HEPES (Roth)	32.17g
Distilled water	Add to 900ml

Adjust pH to 7.6.

For the working (0.3x) solution, add 10ml of stock solution to 990ml of distilled water.

Tricaine (20x - stock solution for 100ml)

Ingredients	Amount
Tricaine/MS-222 (PharmaQ, UK)	400mg
Distilled water	100ml
Tris (Alfa Aesar), pH adjusted to 9	2ml

Adjust pH to 7. Store in darkness and in the fridge or in the freezer in aliquots.

Working solution made by diluting 1 ml of 20x stock in 19ml of 0.3x Danieau's buffer.

(+)-JQ-1 (stock solution for 250µl)

Ingredients	Amount
(+)-JQ-1 (Sigma Aldrich)	5mg
DMSO (Sigma Aldrich)	250µl

(+)-JQ-1 (2 µM working solution)

Ingredients	Amount
(+)-JQ-1 stock solution	9.14µl
DMSO (Sigma Aldrich)	1% (2ml in 200ml solution)
Danieau's	198 ml

Working solution was prepared fresh before each experiment.

3.Results

3.1 Using zebrafish to investigate dynamics of oligodendrocyte formation and axonal myelination.

Zebrafish has had an increasing popularity as a model system for cellular neuroscience in general and for specifically oligodendrocyte biology (Czopka, 2016). Zebrafish larvae swam into the mainstream due to their advantages, such as their genetic accessibility, their rapid early development, their translucent bodies making them ideal for *in vivo* microscopy, and their utilization in high throughput drug screening surveys. The zebrafish nervous system is remarkably similar to the mammalian one, while developing in a fraction of the time mammalian systems develop. Simple *in ovo* injections of plasmid DNA can lead to the creation of transgenic lines which express certain fluorescent molecules under the control of specific promoter elements, ideal for studying different cell populations during development *in vivo* (Preston & Macklin, 2015).

3.1.1. Establishment of reagents to study neurons and glia in vivo

For labelling oligodendrocytes *in vivo* in zebrafish, I used the promoter of myelin basic protein (mbp) (Jung et al., 2010), which is expressed in all oligodendrocytes in the CNS as well as in Schwann cells, the myelinating glia of the PNS.

I used the following lines:

Tg(mbp:KillerRed) was used to express the fluorescent protein KillerRed in myelinating cells. KillerRed is cytoplasmic, which allows me to label somata of oligodendrocytes as well as cytoplasmic channels on myelin sheaths. This provides information about the general morphology and localization of the cells. (Figure 3.1 B)

Tg(mbp:nls-EGFP) was used to express EGFP targeted to the nucleus by carrying a nuclear localization signal (nls). It allows for a clearer quantification of oligodendrocyte number and

assessment of position, without the obscuration that the cytoplasmic proteins create due to the density of labelling (Figure 3.1 C).

Tg(mbp:mem-XFP) was used to label myelin by membrane anchored fluorescent proteins (such as EGFP-CAAX) and allows for accurate depiction of myelin sheath morphology (Figure 3.1 D).

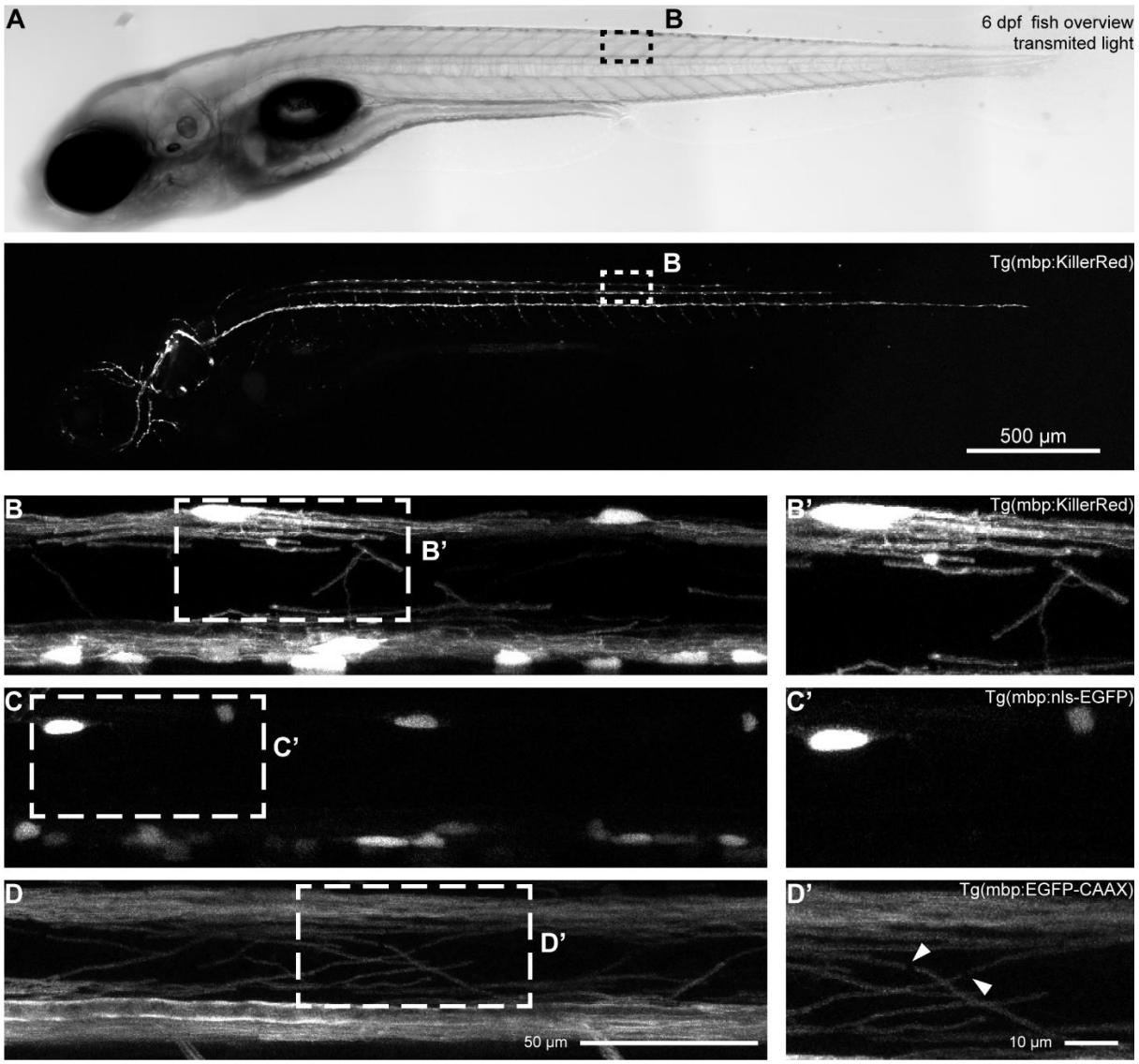

Figure 3.1 Genetic tools to label myelinating oligodendrocytes.

Different genetic tools allow to label different cellular sub-compartments.
A. Overview of 6 dpf zebrafish with transmitted light (top) and all myelinating cells (Tg(mbp:KillerRed) - bottom). Box indicated the size and location of the ROI shown in B. Scale bar = 500µm.
B. Tg(mbp:KillerRed) showing a cytoplasmic fill of all oligodendrocytes. Scale bar = 50µm. **B'.** Zoom in of the boxed area. Scale bar = 10µm.
C. Tg(mbp:nls-EGFP) showing the nuclei of all oligodendrocytes. Scale bar = 50µm. **C'.** Zoom in of the boxed area. Scale bar = 10µm.
D. Tg(mbp:EGFP-CAAX) showing the myelin of all oligodendrocytes. Scale bar = 50µm. **D'.** Zoom in of the boxed area. Scale bar = 10µm.

The spinal cord is comprised of a number of interneurons that project axons either to the brain (afferent) or to the posterior of the spinal cord (efferent). In order to label spinal cord neurons, I used constructs carrying the contactin1b (cntn1b) promoter, which is a neuron-specific promoter that is biased towards larger calibre axons (Czopka et al., 2013). Lastly, in order to observe finer neuronal processes, I employed the huC promoter (Park et al., 2000), which labels many neuronal subtypes. Using these promoters in a transient expression paradigm, I could label individual neurons, of various subtypes, which can be identified by their morphology (Goulding, 2009), Figure 3.2). These neuronal subtypes also show different myelination patterns, as it will be indicated in the following paragraphs.

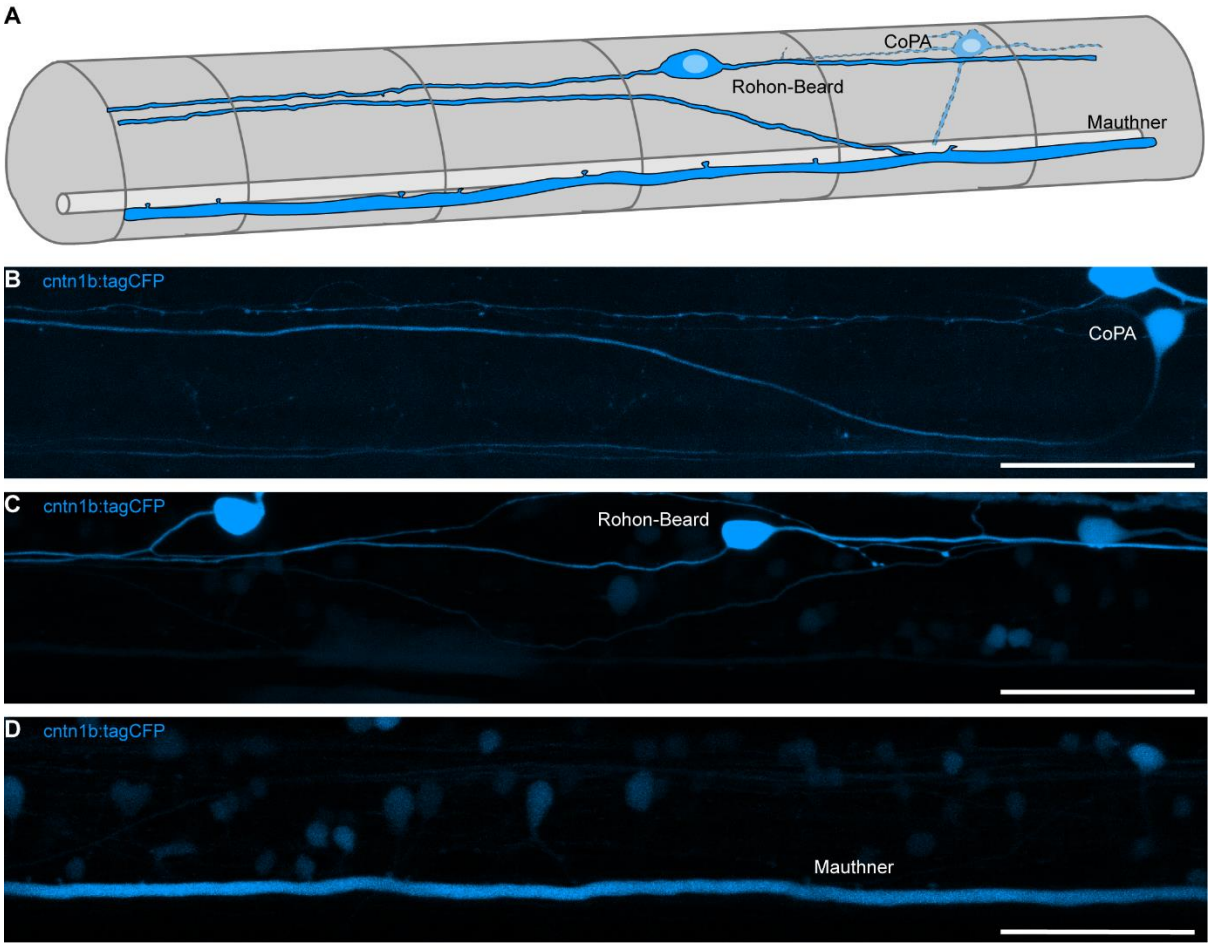

Figure 3.2 Neurons and axons of the zebrafish spinal cord

Transient expression of cntn1b:tagCFP labels different neuronal subtypes in the spinal cord
A. Overview of the spinal cord with labelled neurons. Note the Rohon-Beard somata and processes in the dorsal spinal cord, CoPA somata overlapping with the dorsal axonal tract and the prominent presence of the large Mauthner axon in the ventral spinal cord. Scale bar:50µm
B. Cartoon showing the relative positions and trajectories of CoPA, Rohon-Beard and Mauthner axons in the spinal cord.

I focused my analysis mainly on sparsely labelled CoPA (Commissural Primary Ascending) neurons, which are among the first ones to get myelinated in the dorsal spinal cord (Figure 3.3 A, B) (Koudelka et al., 2016). CoPA neurons have their somata in the dorsal spinal cord and project their axons towards the ventral spinal cord. Then, they cross the midline and ascent again to the dorsal axonal tract, which they follow and project to the brain. CoPA neurons receive synaptic input from Rohon-Beard sensory neurons (see next paragraph), and they then convey the signal to V2a interneurons (Pietri et al., 2009).

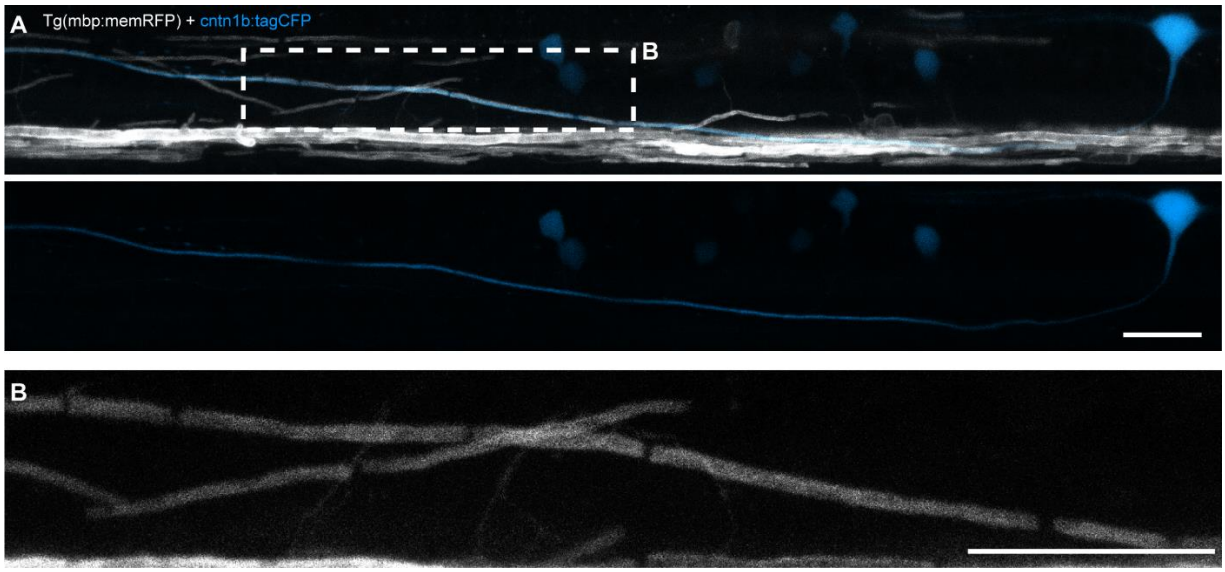

Figure 3.3 CoPA axon overview and myelination.

A. Single labelling of a CoPA neuron with its soma on the contralateral side and the axon descending and crossing the midline to ascent to the ipsilateral dorsal tract (Top) neurons and myelin labelled, (bottom) only neurons labelled).
B. Magnification of the boxed area in A. showing a fully myelinated part of the CoPA neuron**.** Scale bars:20μm

I also made observations about the Rohon-Beard neurites, which are very rarely myelinated, often carrying a single myelin segment per cell (Figure 3.4). Rohon-Beard neurons are shown to be involved in mechanosensation, responding to light touch stimuli (Knafo et al., 2017; Roberts et al., 2012).

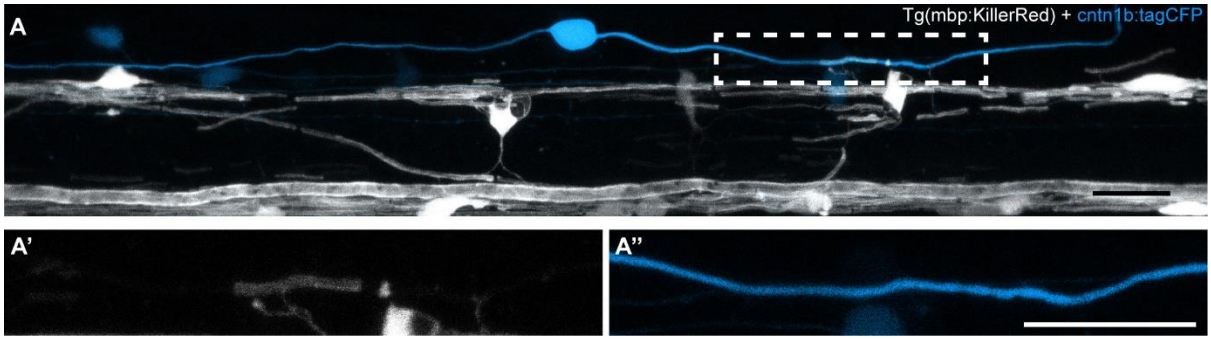

Figure 3.4 Rohon-Beard neurite overview and myelination.

A. Rohon-beard sensory neuron (brightest cell body) with its two processes, one afferent and one efferent with myelin labelling.
A', A'' Magnification of the boxed area in A. showing the RB process around a myelinated segment. (**A'**) myelin only, (**A''**) neuron only. Scale bars:20µm

Another neuron that I analysed was the Mauthner neuron, because of its interesting morphological properties. Each zebrafish has two Mauthner cells, located in close to the midline of rhombomere 4. From there, they project to the posterior of the fish in a stereotyped path along the ventral spinal cord. Mauthner axons are primarily characterized by their large size, and they are known to be involved in quick escape responses, known as C-start responses (Eaton et al., 1991). Mauthner axons are identified as the first axons that are myelinated in the spinal cord, myelinated first in the anterior and later in the posterior spinal cord (Almeida et al., 2011), Figure 3.5).

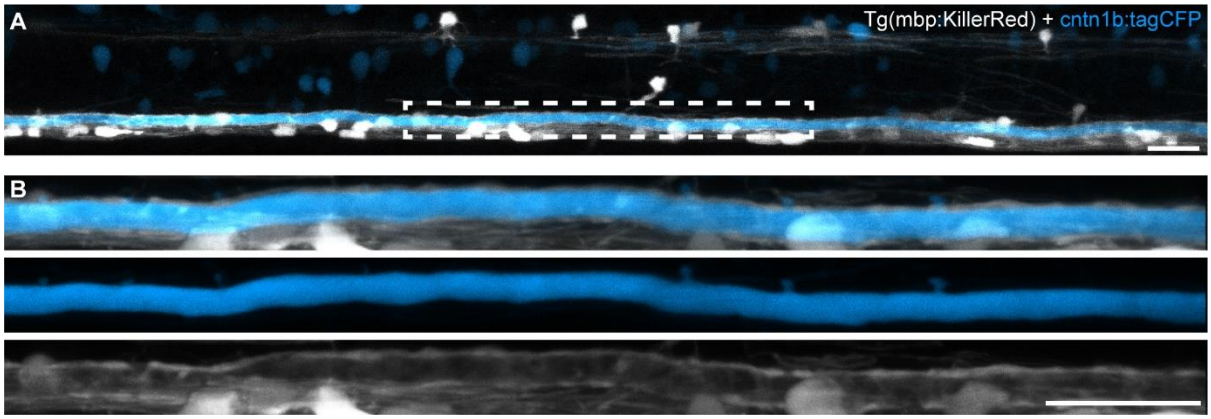

Figure 3.5 Mauthner axon overview and myelination.

A. Spinal cord overview with the Mauthner axon prominently labelled and all myelin labelled.
B. Magnification of the boxed area in A., showing the Mauthner axon (cyan) and all myelin (grey). Note the prominent the large en passant synaptic boutons in the cyan channel. Scale bars:20µm

Lastly, in order to label phagocytic cells, microglia, and macrophages, I used the microfibril associated protein 4 (*mfap4*) promoter (Walton et al., 2015). This promoter is expressed in peripheral macrophages and in microglia of the brain and the spinal cord. To visualize all cells, I used the transgenic line Tg(mfap4:memCerulean) (Marisca et al., 2020) - Figure 3.6). *mfap4*+ cells can be found throughout the body, with a higher concentration at the caudal hematopoietic tissue (Walton et al., 2015), Figure 3.6 B boxed area).

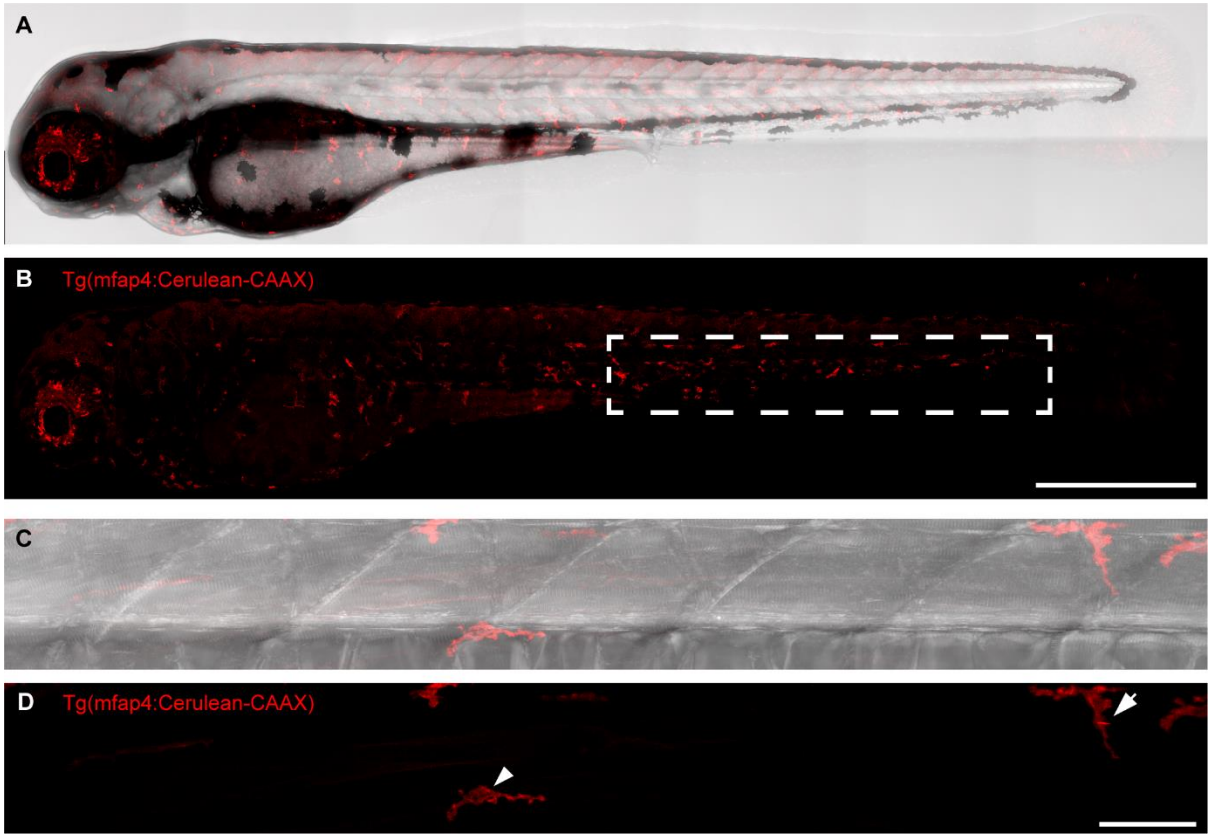

Figure 3.6 Labelling zebrafish phagocytes

A. Overview of 4 dpf zebrafish with labelled phagocytes and transmitted light.
B. Overview of 4 dpf zebrafish with labelled phagocytes (single channel). Boxed area indicates the caudal hematopoietic tissue. Scale bar:500µm
C. Spinal cord zoom in at 6 dpf with transmitted light and labelled phagocytes.
D. Spinal cord zoom in at 6 dpf with labelled phagocytes. Arrowhead points at microglia, arrow points at a peripheral phagocyte. Scale bar:50µm

Using these different genetic tools, I was able to transgenically label phagocytes, oligodendrocytes, and spinal cord neurons. I could describe the overall myelination and oligodendrocyte numbers in the spinal cord, but also the myelination of single axons for a considerable portion of their length. I

used these tools to analyse myelin dynamics and myelination of individual axons in development and following myelin damage.

3.1.2. Developmental oligodendrogenesis in the zebrafish spinal cord

It has been well established that oligodendrocyte numbers and myelin content increases in the spinal cord between 4- and 8-days post fertilization (dpf) (Czopka et al., 2013). It was recently shown by our group that oligodendrocyte numbers continue to increase at least until 30 dpf (Marisca et al., 2020). Apart from the ongoing oligodendrogenesis, we have already described the dynamics of individual sheaths from both early and late born oligodendrocytes (Auer et al., 2018). However, it remained unclear where and on which neurons new myelin, formed by newly differentiated oligodendrocytes, is deposited within the spinal cord. Moreover, the location where individual new oligodendrocytes appear in the tissue is not yet described. So, firstly, I wanted to understand the dynamics and distribution of myelination in terms of myelin sheath formation as well as oligodendrocyte differentiation within the spinal cord.

It has been already described that spinal cord myelination in zebrafish does not happen all at once, but oligodendrocytes in the anterior spinal cord differentiate first, followed by oligodendrocytes in the anterior (Almeida et al., 2011). Hence, I focused my analysis on a field of view centred around somite segment 17, which marks the middle of the trunk of the fish. Because the fish increases in size over time, I always measured cells within a field of view defined by distinguishable cell bodies and I corrected my measurements for body growth, to keep measurements consistent.

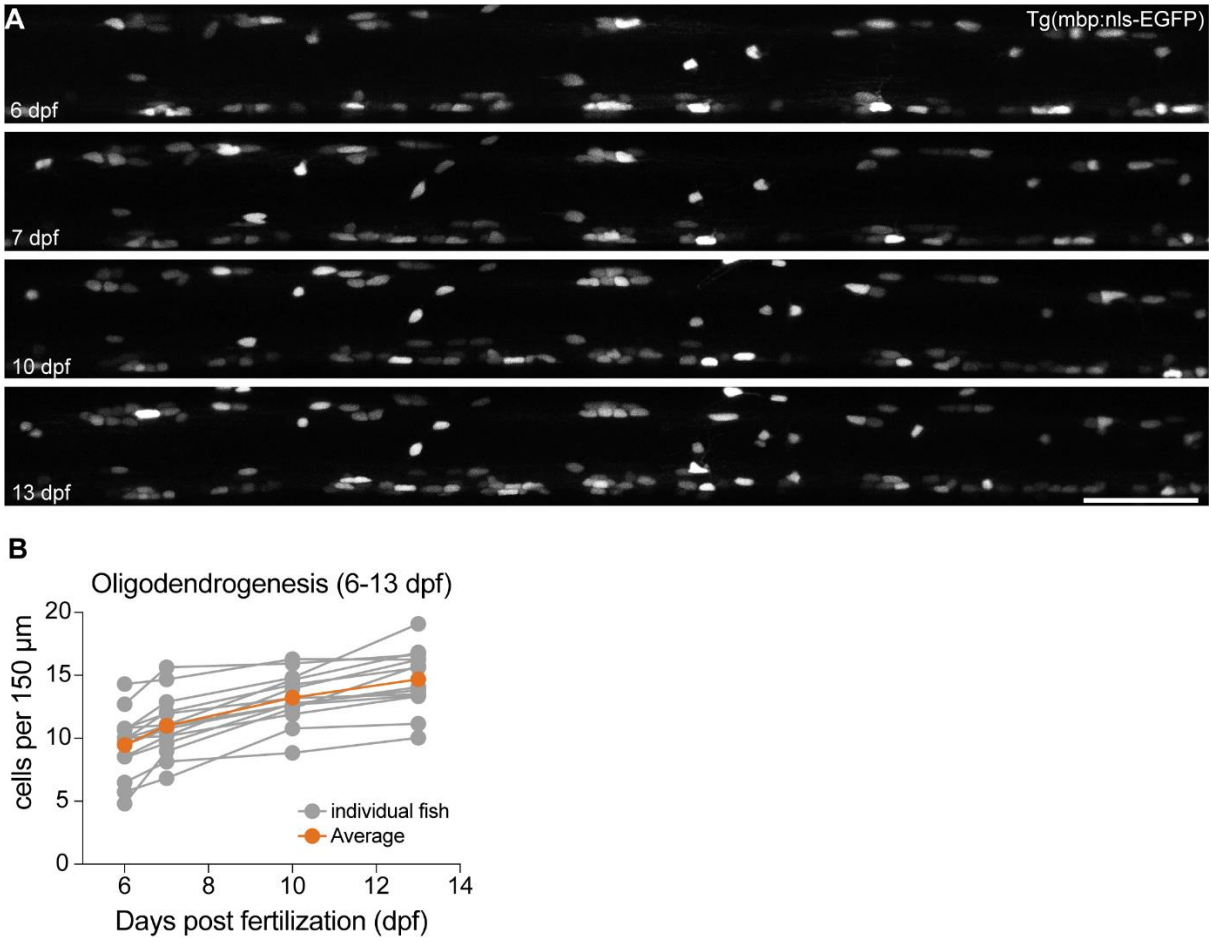

Figure 3.7 Oligodendrocyte number increase between 6 and 13 dpf.

A. Confocal images timeline showcasing the increase in oligodendrocyte numbers in the area around somite segment 17. Scale bar:50µm
B. Quantification of oligodendrocyte numbers per fish over time, expressed as cells per 150µm. Grey lines show individual fish, orange line shows the average.

As mentioned before, it is known that throughout the spinal cord, oligodendrogenesis proceeds at least until 30 dpf (Marisca et al., 2020). First, I wanted to verify this finding. I quantified that at 6 dpf, there are on average 9.48±2.57 oligodendrocytes per 150 µm of spinal cord (n=14 fish). By 13 dpf, there are 14.7±2.4 oligodendrocytes (n=14 fish). In total, oligodendrocyte numbers increase by 55% during the second week of life, with a daily increase of ~9.2% (Figure 3.7 A, B).

It has been described that oligodendrocyte precursors do not consist of a homogenous population of cells, but there are two subgroups with different localizations within the spinal cord, which also exhibit different properties (Marisca et al., 2020). Specifically, OPCs can be divided into cells

localized in neuron-rich areas (grey matter for simplicity) and axon-rich areas (white matter). My oligodendrocyte imaging allows me to assess the localisation of newly differentiated oligodendrocytes in these two regions and describe if there are differences in the differentiation rates between grey and white matter.

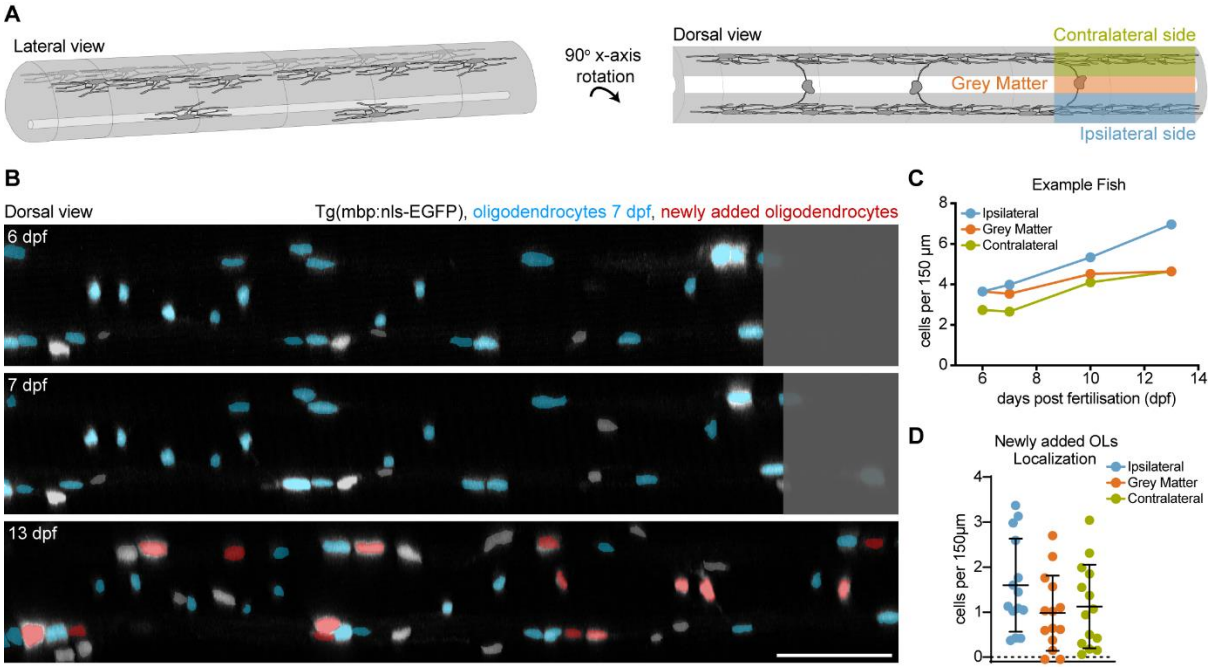

Figure 3.8 Distribution of newly differentiated oligodendrocytes within the spinal cord

A. Cartoon schematic showcasing the rotation and the division of the spinal cord into subregions.
B. Confocal images timelines showing pre-existing oligodendrocytes (false coloured as cyan) as well as newly differentiated oligodendrocytes (false coloured as red). Grey cell bodies are Schwann cells of the PNS as identified by examining the z-stack. Grey shaded boxes show the increase in the size of the field of view during body growth in development. Scale bar:50µm.
C. Quantification of oligodendrocyte numbers in the three sub-compartments of the example shown in B.
D. Quantification of the distribution of newly added oligodendrocytes during this time frame into the three spinal cord regions. Data are shown as mean ± SD.

To quantify the cells, I rotated my samples by 90^{o} around the x axis to obtain a dorsal view. Then I cropped away the ventral spinal cord, which is very dense in oligodendrocytes and myelin labelling, primarily due to the presence of the Mauthner and other reticulospinal axons. I then divided the spinal cord into 3 subregions, the ipsilateral, the contralateral side of the spinal cord that contains the myelinated axon tracts (white matter) and the centre of the spinal cord, which is constituted primarily of neuronal cell bodies (grey matter) (Figure 3.8 A). I found that newly added oligodendrocytes are

relatively equally added in all three regions, with on average increase by 1.6±1.03 OLs per 150 µm in the ipsilateral side, by 0.98±0.84 OLs per 150 µm in the contralateral side and by 1.12±0.93 OLs per 150 µm in the grey matter (n=14 fish. Repeated Measurements one-way ANOVA, p = 0.1408, no significance in multiple comparisons) (Figure 3.8 B-D).

During my experiments, I noticed that the number of myelinated axons in the dorsal tract of the spinal cord increases over time. However, it was also evident from my live imaging experiments, that new myelin forms between the two prominent axonal tracts (dorsal and ventral), in the lateral, more superficial part of the spinal cord (Figure 3.9A, B).

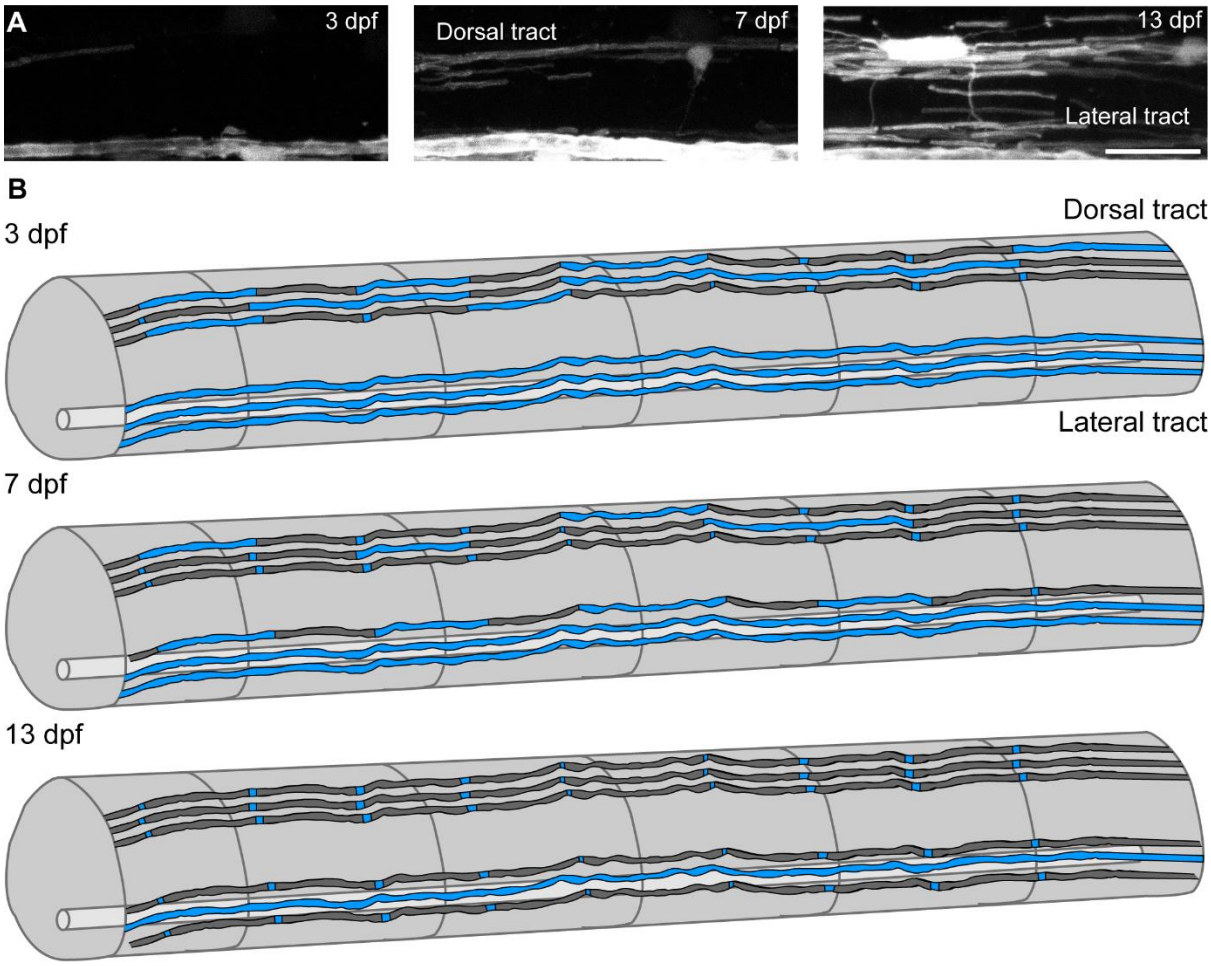

Figure 3.9 Progression of myelin deposition during development within the spinal cord.

A. Confocal image timeline showing all myelin in the spinal cord. Note the increase in myelin density, first in the dorsal and then in the lateral tract. Scale bar: 50µm.
B. Illustration of myelin(grey) deposition in axons(cyan) of the dorsal and lateral tracts over time.

I then wanted to quantify the progression of myelination in these two spinal cord compartments. Fluorescent label of myelin is very dense, especially in the dorsal tract, making it challenging to obtain accurate measurements of the number of myelinated axons from confocal live imaging. To measure the number of myelinated axons in the spinal cord, I performed Transmission Electron Microscopy of spinal cord cross sections at 7, 10 and 13 dpf. I found that the average amount of myelinated axons in the spinal cord dorsal to the Mauthner axon increases from 34.44±4.88 myelinated axons per hemi-spinal cord at 7 dpf to 50.33±3.71 at 13 dpf (n=9/3 sections/fish -~46% increase Figure 3.10A-C).

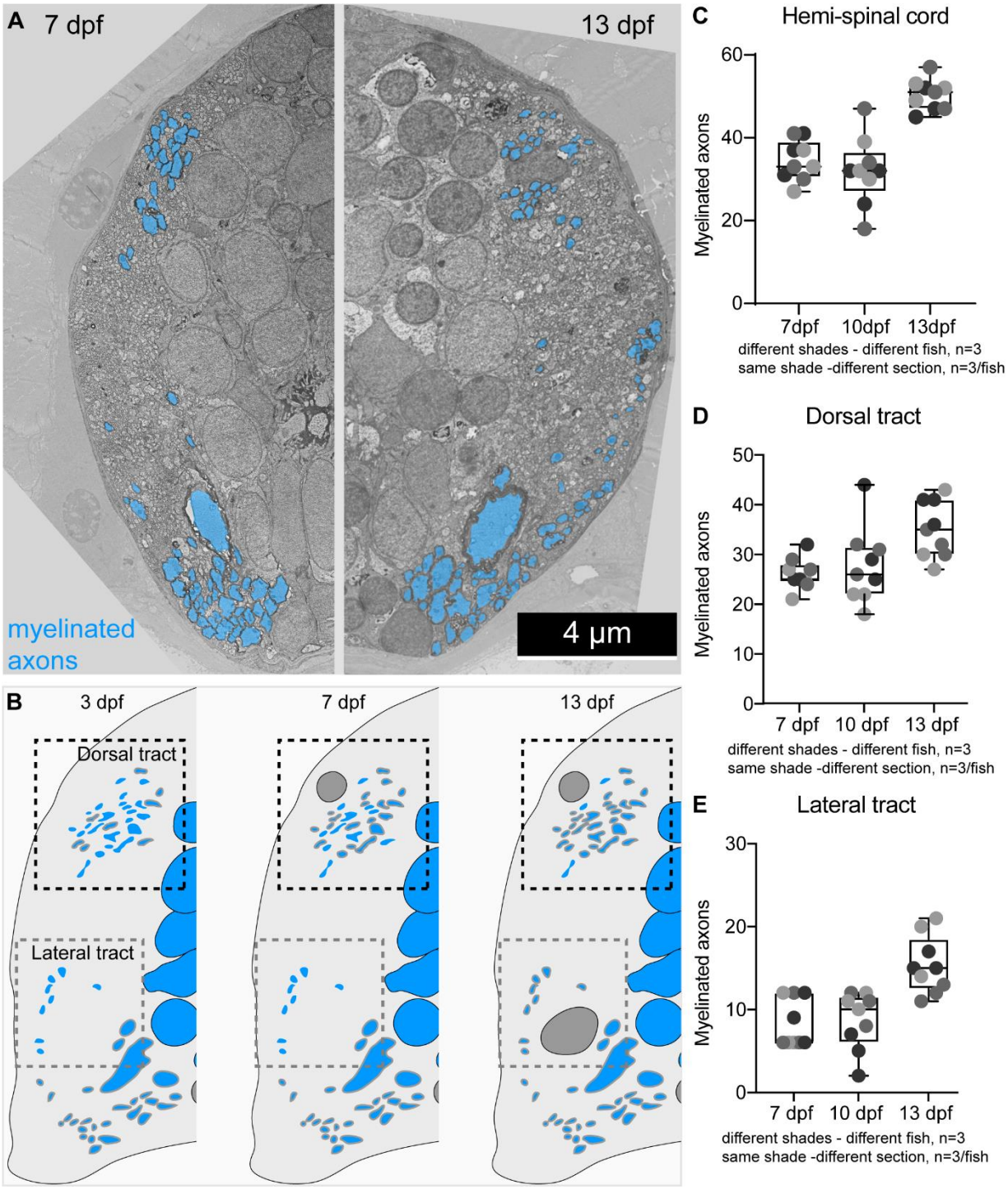

Figure 3.10 Progression of myelin deposition during development

A. TEM micrograph showing the myelinated axons (cyan) at 7 dpf (left half) and 13 dpf (right half). Scale bar: 4µm.
B. Cartoon schematic showcasing the progression of myelination in the dorsal and lateral spinal cord from 3 to 13 dpf. Axons are coloured cyan, oligodendrocytes and myelin dark grey.
C. Quantification of myelinated axons per half of the spinal cord. Axons ventral to the Mauthner axons were excluded from this analysis. Data shown as boxplots with range and individual values. Data point colours represents different fish. Data points of the same colour represent the same sections.
D. Quantification of myelinated axons in the dorsal tract over time. Data shown as boxplots with range and individual values. Data point colours represent different fish. Data points of the same colour represent the same sections.
E. Quantification of myelinated axons in the lateral tract over time. Data shown as boxplots with range and individual values. Data point colours represent different fish. Data points of the same colour represent the same sections.

Focusing on the two axonal tracts I was interested in, I found that the number of myelinated axons in the dorsal tract increases by increases from 26.11±3.14 at 7 dpf to 35.00±5.71 at 13 dpf (n=9/3 sections/fish - ~34.1% increase). At the same time, in the lateral spinal cord, the number of myelinated axons increases from 8.33±2.92 at 7 dpf to 15.33±3.43 at 13 dpf (n=9/3 sections/fish - ~84% increase - Figure 3.10C-E).

To conclude, my data verify that myelination in the zebrafish spinal cord is dynamic with new oligodendrocytes forming continuously. Choice of myelinated axons follows a stereotypic pattern: oligodendrocytes myelinate targets in the dorsal myelinated tract as well as in laterally running axons, which form a new, lateral myelinating tract.

3.2 Studying oligodendrocyte dynamics following focal demyelination.

3.2.1 Establishing an assay for experimental oligodendrocyte ablations.

Having shown how stereotyped spinal cord myelination is during development, I can use this model to test how dynamics of oligodendrocyte formation and axonal myelination deviate from 'normal' development after introducing focal demyelination by ablating individual oligodendrocytes.

I ablated cells expressing KillerRed, a genetically encoded photosensitizer (Bulina et al., 2005) that upon light excitation produces hydrogen peroxide and Reactive Oxygen Species (ROS), that are highly toxic to cells. Often, excitation of KillerRed is done using a normal epifluorescence lamp (Teh et al., 2010). For my experiments, as I wanted to ablate individual oligodendrocytes, I used a 770nm 2-photon laser at a low power setting. I set up the 2-photon laser, to scan linearly across the soma of the targeted oligodendrocyte, where a large amount of KillerRed localizes (Figure 3.11).

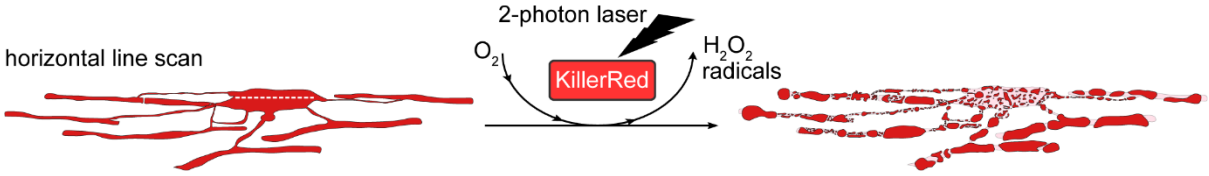

Figure 3.11 Oligodendrocyte ablations using KillerRed.

Cartoon – KillerRed excitation by 770nm two-photon laser used to ablate individual oligodendrocytes by horizontal line scan across the cell's soma.

This allowed me to observe dying oligodendrocytes over time and run time-lapses between 4 and 5 dpf (Figure 3.12A). I quantified that on average 84.6±37.5 min after ablations cell somata fragmented and disappeared (n=11 cells) (Figure 3.12B).

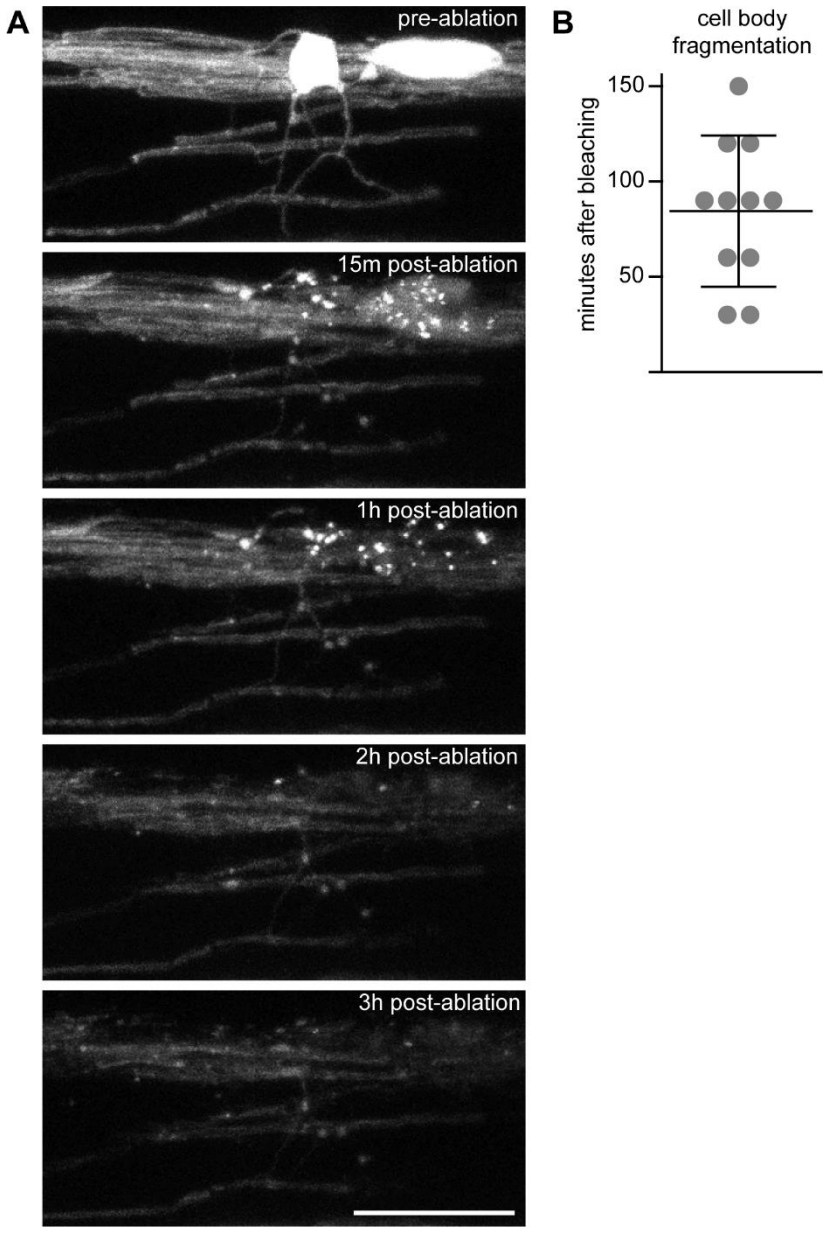

Figure 3.12 Timelapse of dying oligodendrocyte following KillerRed ablations.

A. Confocal image timeline (top to bottom) showing an oligodendrocyte disintegrating following KillerRed ablation. Scale bar: 20µm.
B Quantification of cell body fragmentation time. Data shown as mean ± SD.

I was also able to follow the process of cell disintegration in more detail. The example in Figure 3.13 shows that most myelin debris are removed by 24 hours post ablation (hpa), as well as the loss of two oligodendrocytes causes a significant decrease in the density of myelin within the affected area.

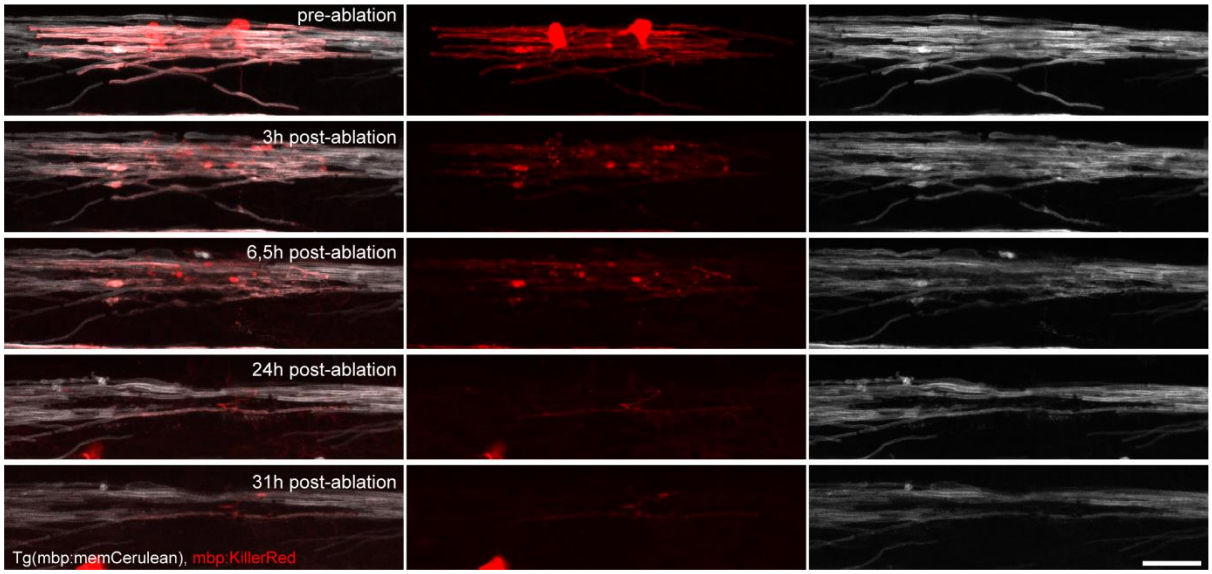

Figure 3.13 Timelapse of myelin disintegrating following KillerRed ablations.

Confocal image timeline (top to bottom) showing two oligodendrocytes disintegrating following KillerRed ablation. Note the decrease in density of myelin over time. Scale bar: 20μm.

In order to better target single oligodendrocytes, I focused my manipulation to the cells with somata in the dorsal spinal cord, because this is an area with sparser oligodendrocytes (compared to the ventral spinal cord). These cells, as I already described before, are in close proximity to the dorsal myelinated tract and the axons that run within it. Even though the laser power needed for the oligodendrocyte ablations was relatively low, an important step was to assess the degree of bystander damage putatively caused by the laser line scan in the dorsal tract axons, which have been my main focus throughout my research.

To do this, I performed oligodendrocyte ablations in zebrafish with Tg(mbp:KillerRed) transgenic background, where all oligodendrocytes express KillerRed. In addition to the full transgene, I also transiently injected cntn1b:tagCFP or huC:tagCFP, which label neurons and their axons. I was able to label 66 axons in 8 fish in total, proximal to KillerRed expressing oligodendrocytes, which I ablated. Comparing pre-ablation and 1hpa images, I was not able to observe any form of axonal damage (Figure 3.14A, B). Only when I rotated the scanning direction of the 2-photon laser, making it perpendicular to the dorsal tract, I ended up truncating 1/12 labelled neurites (n=1 fish –not shown).

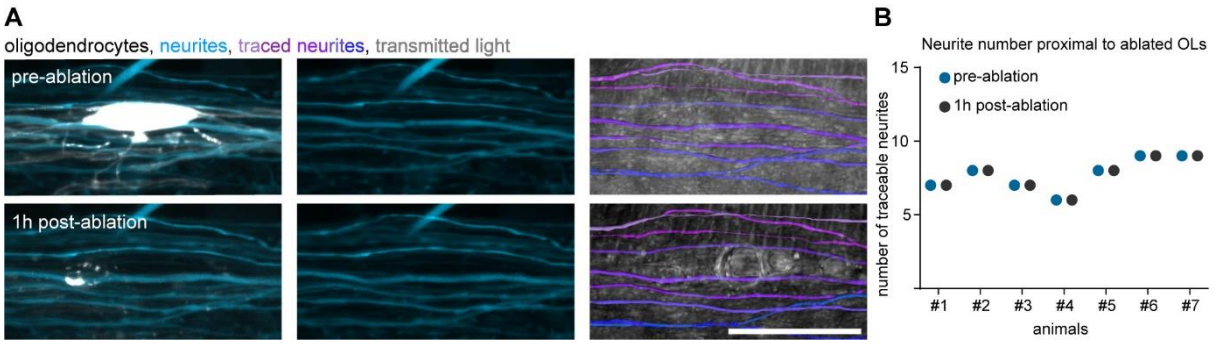

Figure 3.14 Assessing axonal bystander damage following dorsal oligodendrocyte ablations by light microscopy.

A. Confocal images showing the ablation of a single oligodendrocyte surrounded by multiple neurites. (right) Neurites were traced, false-coloured and overlayed with the transmitted light to show putative damage.
Scale bar = 10 µm.
B. Quantification of neurites pre- and post-ablation oligodendrocyte ablations.

Transient injections allowed me to label some, but not all axons that comprise the dorsal axon tract. To better assess the possibility of axonal loss due to the oligodendrocyte ablations, I compared control to ablated sides of the same fish using TEM cross-sections. First, by measuring the perimeters of the 50 largest control side axons, I determined that only two of them were smaller than 0,7 µm (2/450 measured axons in n=9 sections from n=3 fish). I then quantified the perimeters of the 50 largest axons in the ablated side. If the ablations caused axon damage, that would mean that within the 50 largest axons I measured, I would be able to find more axons smaller than 0,7 µm. I found that while I was able to find slightly more axons smaller than 0,7 µm within the ablated side (8/450 measured axons, in n=9 sections from n=3 fish), this result was not significant (p = 0,5, Wilcoxon test).

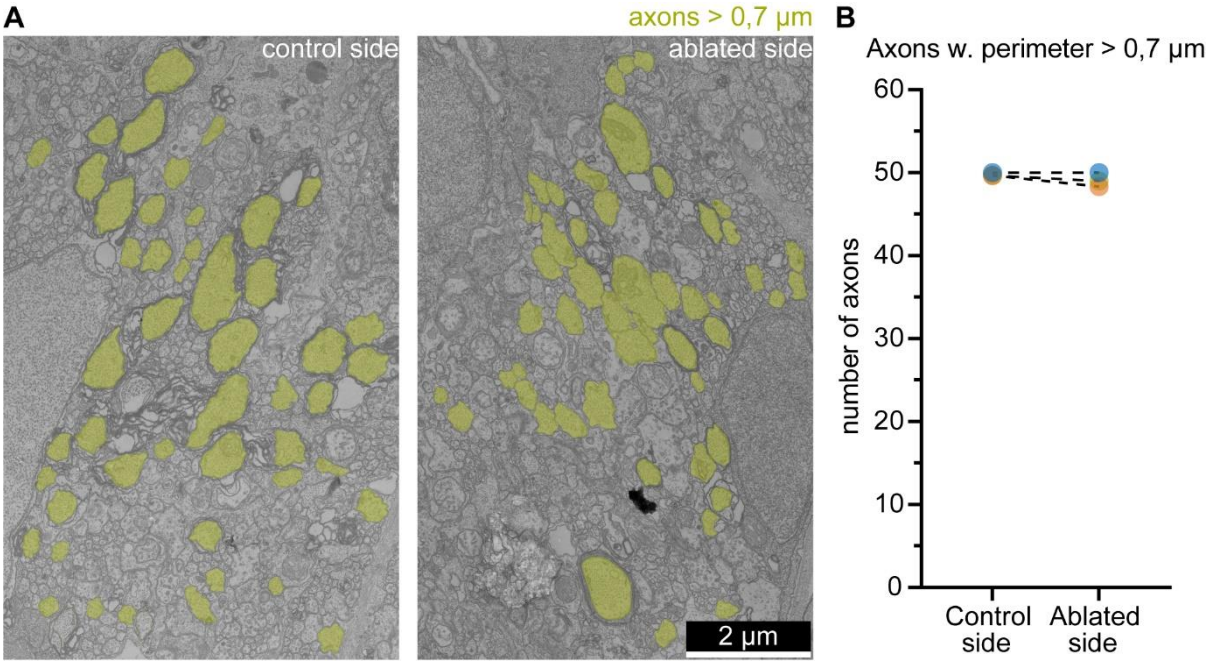

Figure 3.15 Assessing axonal bystander damage following dorsal oligodendrocyte ablations by electron microscopy.

A. TEM micrographs comparing the control and ablated dorsal tracts. Scale bar: 2µm
B. Quantification of axons with perimeter larger than 0,7 µm in control and in ablated sides per fish. Different colours indicate individual animals.

These experiments show that I was able to use my ablation approach to specifically target individual oligodendrocytes efficiently, with minimal bystander damage to surrounding axons.

Phagocytic response to oligodendrocyte ablations

Phagocytosis, the clearing of cell fragments following damage was recently shown (R. Berglund et al., 2020a; Cunha et al., 2020) to be essential for recovery from neuroinflammation and subsequent remyelination in a demyelinated setting. Due to the importance of phagocytic activity to the recovery from demyelination, I wanted to characterize the dynamics of phagocytic cells in proximity to my field of view.

To directly observe phagocytes (microglia as well as infiltrating macrophages), I used the Tg(mfap4:memCerulean) full transgenic line and crossed it to the Tg(mbp:KillerRed) line to ablate oligodendrocytes. These ablations were again performed at 4 dpf and time-lapse microscopy was used to observe phagocytic activity (Figure 3.16). I ablated in total 20 oligodendrocytes in 7 fish and

saw 28 infiltrating phagocytes uptaking fluorescent debris immediately after cell lysis (Figure 3.17A). In 5/7 fish, macrophages had infiltrated the lesion already after 10 min post-ablation, showing how rapidly these cells can react to CNS damage (Figure 3.17B). On average, for every ablate oligodendrocyte, 1.4 phagocytes would infiltrate the lesion area, showing a strong correlation between the degree of myelin damage and the immune response that clears up the debris (Pearson r = 0.9003, p = 0.0009- Figure 3.17C).

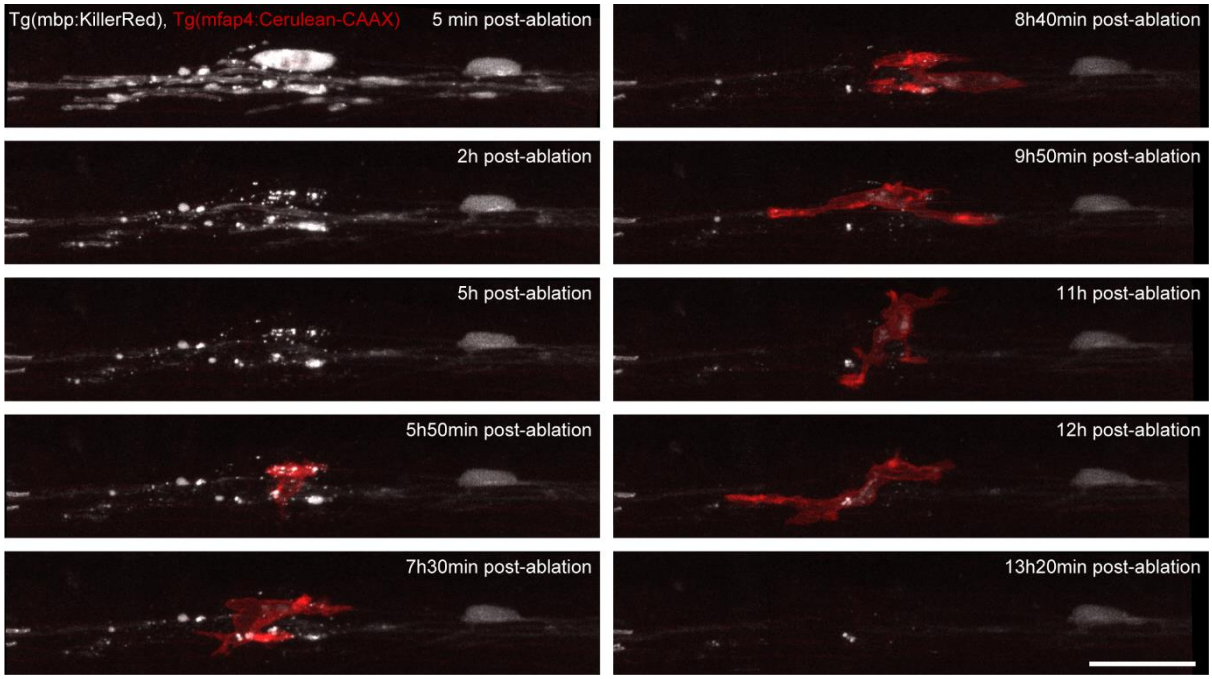

Figure 3.16 Timelapse of single macrophage clearing oligodendrocyte debris.

Confocal image timeline showing the response of a single macrophage to the ablation of an oligodendrocyte Scale bar: 20µm.

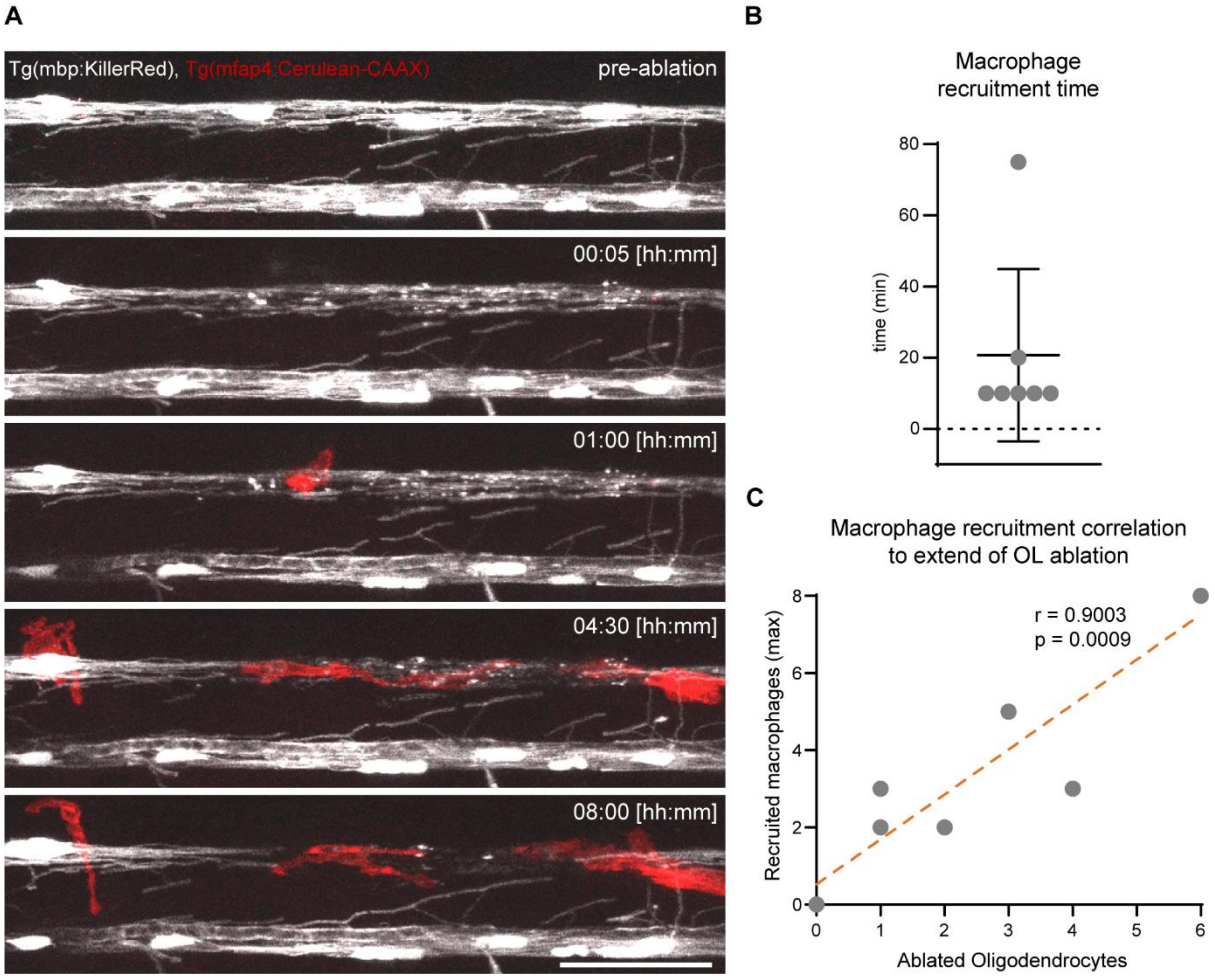

Figure 3.17 Macrophage infiltration following 4 dpf oligodendrocyte ablations.

A. Confocal panel showing a time-lapse of oligodendrocytes and phagocytes following oligodendrocyte ablations. Scale bar = 50 μm.
B. Quantification of macrophage recruitment time following oligodendrocyte ablations. Data shown as mean ± SD.
C. Correlation of recruited phagocyte numbers to ablated oligodendrocytes. Pearson's correlation test. P value and Pearson r depicted in the graph.

Furthermore, I wanted to assess how long phagocytes reside within a demyelinated area. To do so, I used again Tg(mbp:KillerRed) and Tg(mfap4:memCerulean) double transgenic zebrafish and proceeded with multiple oligodendrocyte ablations at the level of somite 17 (Figure 3.18A). I found an average 6.6-fold increase in resident phagocytes in the spinal cord at 1 day post ablation (1.5±1.0 phagocytes pre ablation vs 9.9±2.9 phagocytes at 1 day post ablation, paired t-test, $p < 0.0001$, Figure 3.18B). From 2 to 5 days post ablation the macrophage numbers gradually drop, with a rate on average by 36% per day until they return to almost normal levels at 5 dpa (Figure 3.18C).

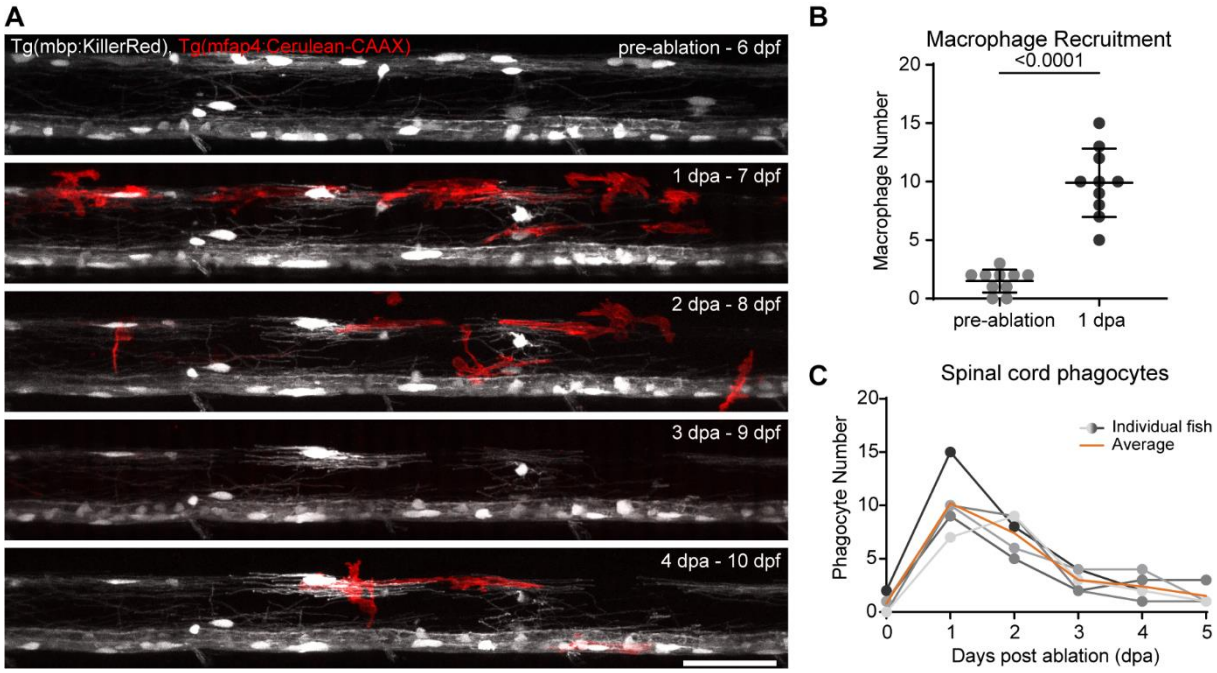

Figure 3.18 Macrophage dynamics following 6 dpf oligodendrocyte ablations.

A. Confocal panel showing a time-lapse of oligodendrocytes and phagocytes following oligodendrocyte ablations. Scale bar = 50 µm.
B. Quantification of macrophage number pre-ablation vs 1d post-ablation. time following oligodendrocyte ablations. Paired t-test. P value depicted in the graph. Data shown as mean ± SD.
C. Quantification of spinal cord phagocytes following oligodendrocyte ablations over time. Shades of grey represent individual samples while the orange line represents the average.

These data show that I can efficiently ablate single as well as multiple oligodendrocytes, without causing any bystander damage to surrounding axons. Macrophages and microglia are attracted to the lesion site rapidly after oligodendrocyte ablations. They phagocytose myelin debris and their response in numbers depends on the extend of demyelination (number of ablated oligodendrocytes). Phagocytes are retained within the lesioned area for longer time, eventually though they migrate again away.

3.2.2. Oligodendrocyte and myelin dynamics following focal demyelination.

As already described, oligodendrocyte ablations lead rapid cell disintegration, including the myelin it was producing. To repair this damage, new myelin has been formed in a process called

remyelination (R. J. M. Franklin & ffrench-Constant, 2008). New myelination is typically the product of the formation of new oligodendrocytes (although recently it has been proposed that surviving oligodendrocytes can also participate in remyelination, in certain experimental models of demyelination – (Bacmeister et al., 2020; Neely et al., 2020). To assess this, I analysed the oligodendrogenesis within a demyelinated area of the spinal cord following multi-oligodendrocyte ablations centred around somite 17 within the spinal cord.

In my analysis, I compare the affected, ipsilateral side (ablated side) with the non-affected, contralateral side (control side). I found that, while the control side oligodendrocyte numbers kept increasing as described for non-affected fish (see chapter 3.1.2), the ablated side represents 17.8±17.1% of the oligodendrocytes of the control side at 7 dpf (1d post ablation) and reaches only 53.9±38.6% of oligodendrocytes of the control side by 13 dpf (7d post ablation), indicating partial recovery (n=28 fish - Figure 3.19A, B).

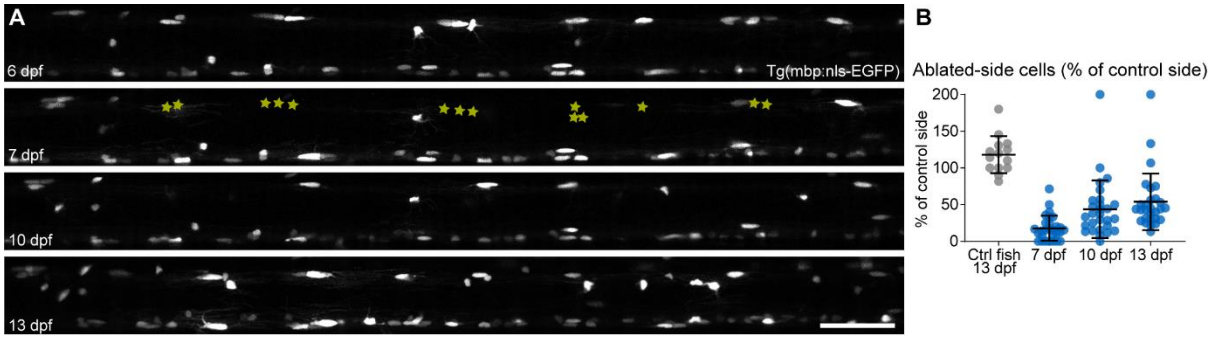

Figure 3.19 Oligodendrocyte ablations at 6 dpf lead to a lasting drop in myelinating oligodendrocytes.

A. Confocal panel showing a time-lapse of oligodendrocytes at different times following oligodendrocyte ablations. Green asterisks indicate the position of ablated cells. Scale bar = 50 µm.
B. Quantification of ablated (ipsilateral) side oligodendrocytes, expressed as percentage of control (contralateral) side cells and compared to control, unablated fish. Data shown as mean ± SD.

I was also curious about the distribution of newly differentiated oligodendrocytes during this timeframe. For this analysis, I once again rotated my obtained images along their x axis, in order to see the spinal cord from a dorsal viewpoint (Figure 3.20A). I divided the spinal cord in three subsegments, the ipsilateral (ablated side), the contralateral (control side) and the central segment which includes oligodendrocytes resident in the grey matter.

I found slightly more newly added cells in the ablated side compared to the control side and the grey matter (1.6±0.89 cells per 150µm in the ablated side vs 1.1±0.8 cells per 150 µm in the grey matter vs 1.12±0.81 cells per 150µm in the control side, n=28 fish, RM one-way ANOVA, p=0.0223, multiple comparison p-values shown in the graph- Figure 3.20B, D). These cell numbers correspond to a rate of oligodendrogenesis that was slightly increased in the ablated side, averaging at 25.82±15.13% while it was 19.04±13.61% in the grey matter and 16.73±14.42% in the control side (n=28 fish, p=0.023, Friedman test).

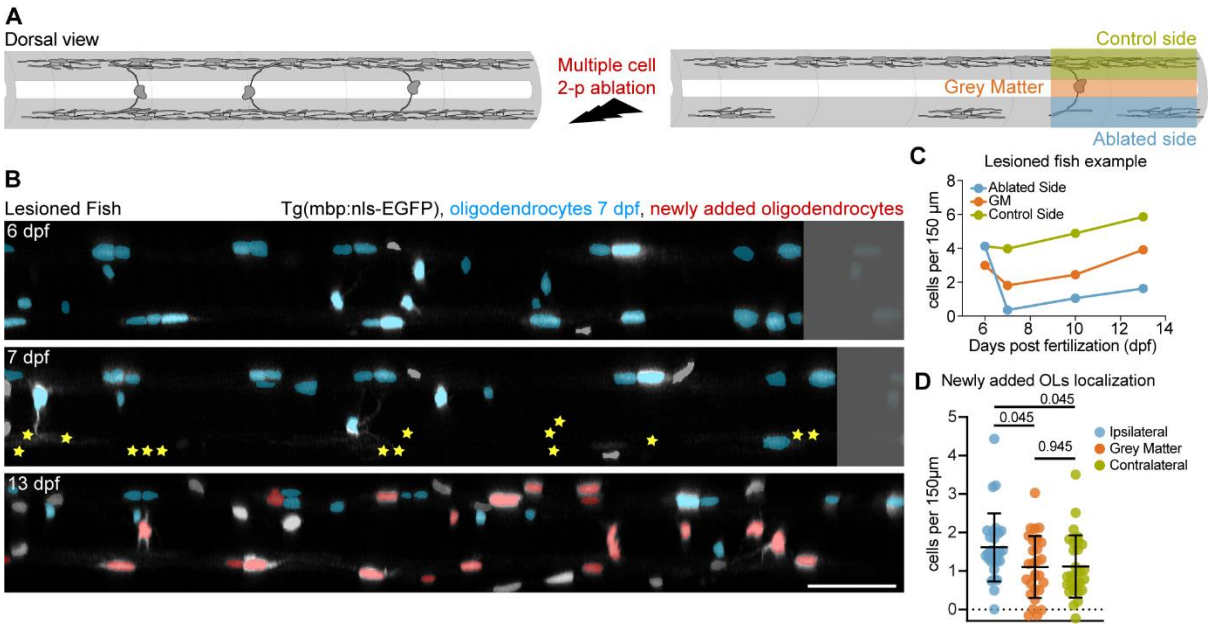

Figure 3.20 Distribution of newly differentiated oligodendrocytes within the spinal cord after 6 dpf ablations.

A. Cartoon schematic showcasing the rotation and the divide of the spinal cord into subregions following oligodendrocyte ablations.
B. Confocal images timelines showing pre-existing oligodendrocytes (false coloured as cyan) as well as newly differentiated oligodendrocytes (false coloured as red). Asterisks indicate the position of ablated oligodendrocytes. Grey cell bodies are Schwann cells of the PNS. Grey shaded boxes show the increase in the size of the field of view during body growth in development. Scale bar:50µm
C. Quantification of oligodendrocyte numbers in the three sub-compartments of the example shown in B.
D. Quantification of the distribution of newly added oligodendrocytes during this time frame into the three spinal cord regions. Data are shown as mean ± SD, RM one-way ANOVA, multiple comparison p-values shown in the graph.

Taken together, these data suggest that following oligodendrocyte loss in developmental fish, the numbers of oligodendrocytes that differentiate after the ablations never reach the numbers of cells

in the control side and they only show a slight increase in their rate of differentiation compared to control side cells.

It is known that individual OLs can make multiple myelin sheaths (10-30 sheaths pin zebrafish (Czopka et al., 2013; Neely et al., 2020). Therefore, it remains possible that fewer oligodendrocytes could produce more sheaths in order to compensate for the lack in OL numbers after ablations.

To address this, I analysed spinal cord cross-sections using TEM. As my ablation experiments were always centred around somite 17, which marks the middle of the fish body, I was able to collect spinal cord cross-sections that localize inside the demyelinated area I created. Using local landmarks, like myelinated axons that were spared from the ablations, I was even able to identify the area of the lesion my sections derived from. (Figure 3.21 A-B)

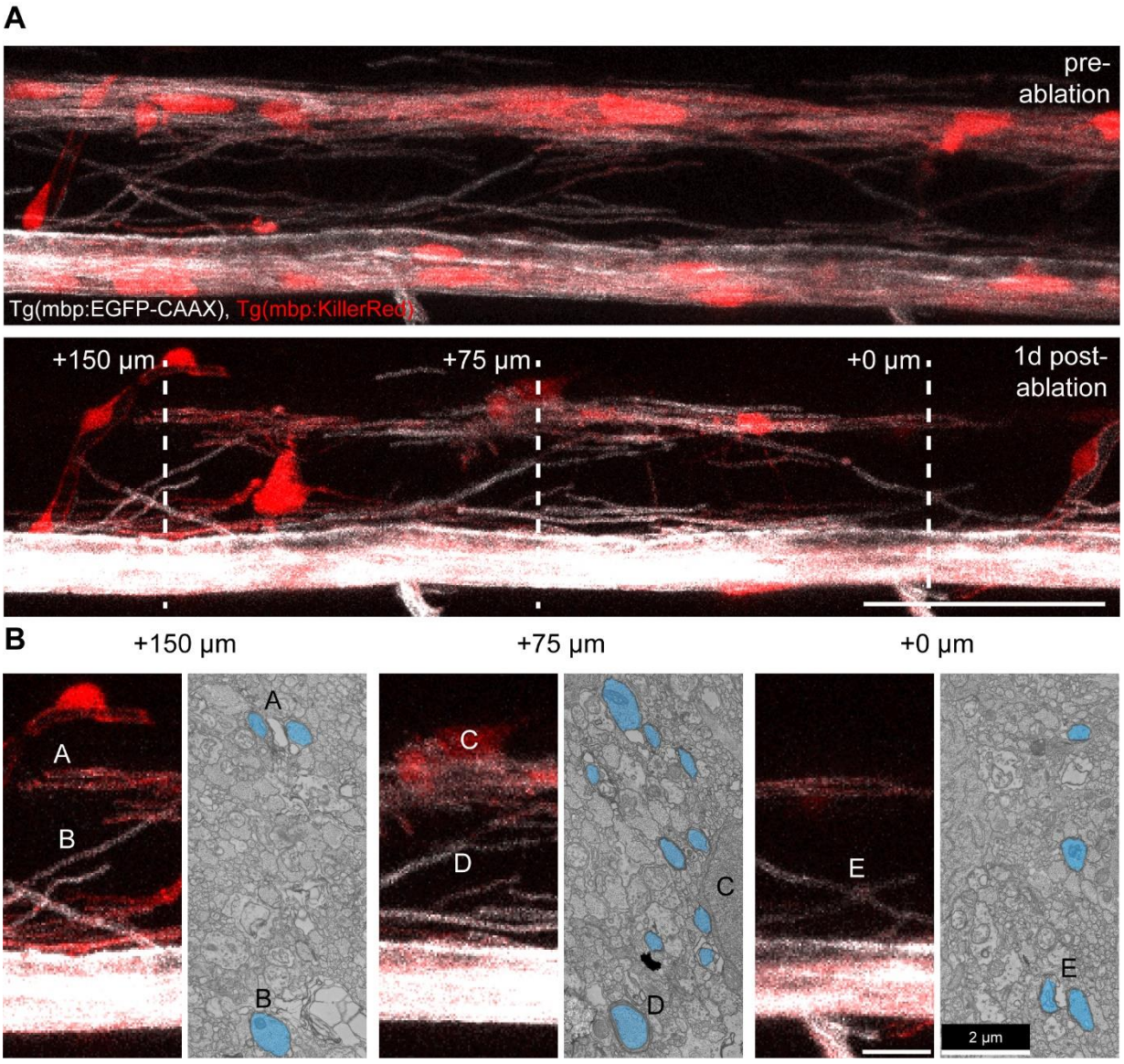

Figure 3.21 Attempt at correlative light and electron microscopy.

A. Confocal images showing a demyelinated area pre and at 1d post-ablation with possible local landmarks marked by dashed lines at 3 positions. Scale bar = 50 µm.
B. Comparison of the confocal areas with respective TEM cross-sections of the same area, with myelinated axons labelled in cyan that seemed to correspond to the landmarks, labelled with letters from A-E. Note that C marks an OL. Scale bar = 2 µm for TEM and.10 µm for confocal images.

By following this approach, I was able to quantify the myelinated axons per spinal cord side (hemi-spinal cord). I found that at 7 dpf (1d post-ablation), the ablated side contained significantly less myelinated axons than the control side (16.22±7.36 myelinated axons in the ablated side versus 34.44±4.88 in the control side, paired t-test, p = 0.0002). This difference remained prominent up to

13 dpf (7d post-ablation) (32.11±5.82 myelinated axons in the ablated side versus 50.33±3.71 in the control side, paired t-test, p = 0.0002 – Figure 3.23 A, B). This indicates that oligodendrocytes born after myelin damage do not show increased potential to respond to extensive demyelination and compensate for the lack of enhanced oligodendrogenesis.

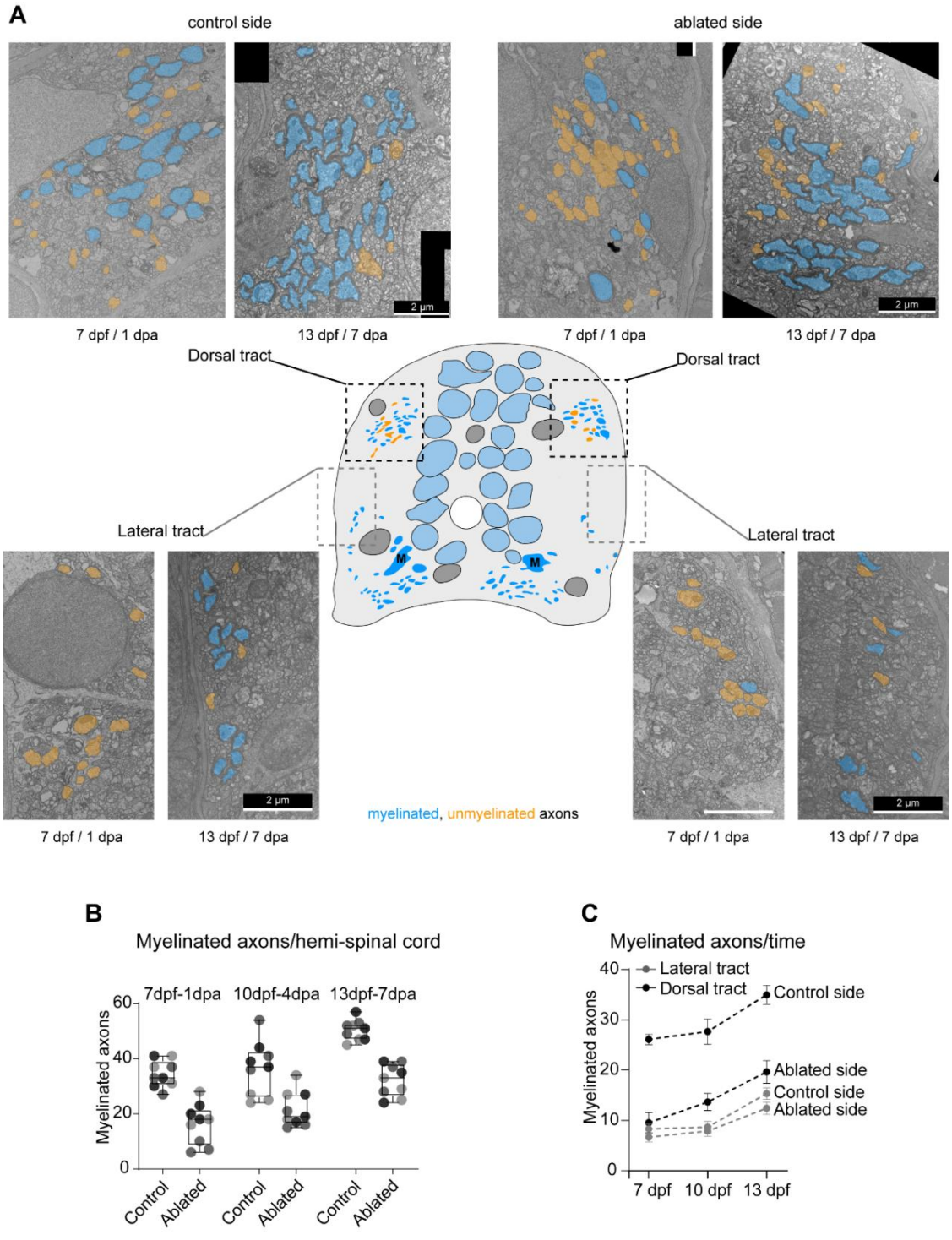

Figure 3.23 Spinal cord TEM analysis reveals only partial remyelination by 13 dpf – 7 d post ablation.

A. Electron micrograph composites depicting the dorsal and lateral myelinated tracts of the spinal cord at 7 dpf and 13 dpf. Control sides (left) are compared to ablated sides (right). Myelinated axons are coloured cyan while non-myelinated are orange. The dorsal tract is depicted at the top of the panel, while the lateral tract at the bottom. Schematic of a spinal cord cross-section at the centre for orientation purposes Scale bar = 2 µm.
B. Quantification of myelinated axon numbers per hemi-spinal cord at 7, 10 and 13 dpf following ablations. Box plots with median and range.
C. Quantification of myelinated axon numbers according to their locations at different timepoints. Data shown as mean ± SD.

3.2.3 Axon choice by newly added oligodendrocytes following focal demyelination.

Since oligodendrocyte dynamics showed no overall response after local demyelination, I assessed if they exhibit preferences in axonal choice for myelination. Within the lesion caused by the ablations there are two conceptually different axonal populations: demyelinated axons that lost their myelin after oligodendrocyte death and non-myelinated axons. Oligodendrocytes could in this context choose the demyelinated axons over the previously unmyelinated ones to restore function through targeted remyelination, even in an environment of no enhanced oligodendrogenesis. Understanding this matter of axon choice is important because gaining a deeper knowledge on oligodendrocyte behaviour in this context can help us device new means to alter it.

As characterized previously, the time between 6 and 13 dpf is characterized by the myelination of laterally running, superficial axons by newly differentiated oligodendrocytes. At the same time, the number of myelinated axons within the dorsal tract also increases. Following demyelination of the dorsal tract, I want to test the capacity of late born oligodendrocytes, to choose between demyelinated dorsal tract axons and developmentally to-be-myelinated lateral tract axons. There are overall 3 possible scenarios (Figure 3.22):

1. Demyelinated axons could be remyelinated by newly added oligodendrocytes.
2. Newly added oligodendrocytes could select preferentially the unmyelinated axons that would be myelinated during normal development.
3. Alternatively, new oligodendrocytes could show no preference between the two axonal populations.

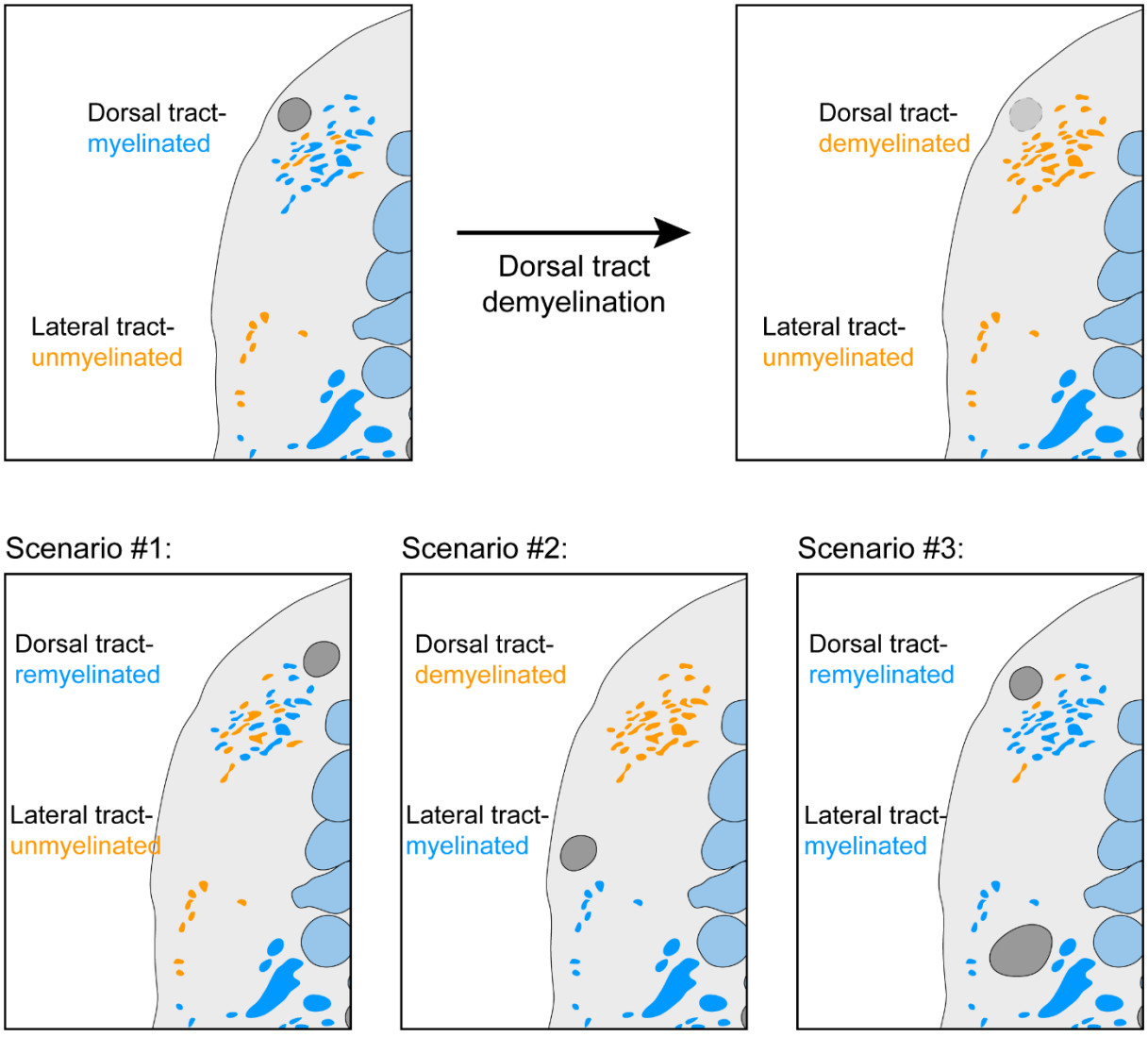

Figure 3.22 Possible scenarios of target axon choice in remyelination.

Illustration of the two axonal tracts within the spinal cord, with the dorsal tract being primarily myelinated and the lateral tract unmyelinated. After demyelination of the dorsal tract axons, newly differentiated oligodendrocytes could remyelinate the affected axons, myelinate the unmyelinated axons or show no preference between the two.

I compared the number of myelinated axons in the dorsal tract to the number of myelinated axons in the lateral spinal cord. I found that myelinated dorsal tract axons increase between 7 and 13 dpf in the ablated side and in the control side by similar rates. Over the same timeframe, lateral tract myelinated axon numbers also increase, but the addition of new myelinated axons is similar in both control and ablated sides. (Figure 3.23C).

Together, this means that newly differentiated oligodendrocytes likely have no preference between remyelinated affected axons or myelinated non-affected ones.

This result of no enhanced preference towards demyelinated axons prompted me to investigate further why demyelinated axons would not be competitive targets in the process of remyelination. It has been described that calibre is also one of the criteria deciding whether an axon will be myelinated or not (Stassart et al., 2018). Importantly, it has also been proposed that myelinated axons (or parts of axons) have larger calibre than non-myelinated axons (or parts of axons) (Costa et al., 2018). Since calibre is a criterion of myelination, changes in calibre in demyelinated axons could affect their remyelination. Therefore, I also analysed the calibre of the axons in my TEM experiments, and I tested if myelin loss affects the calibre of individual axons locally.

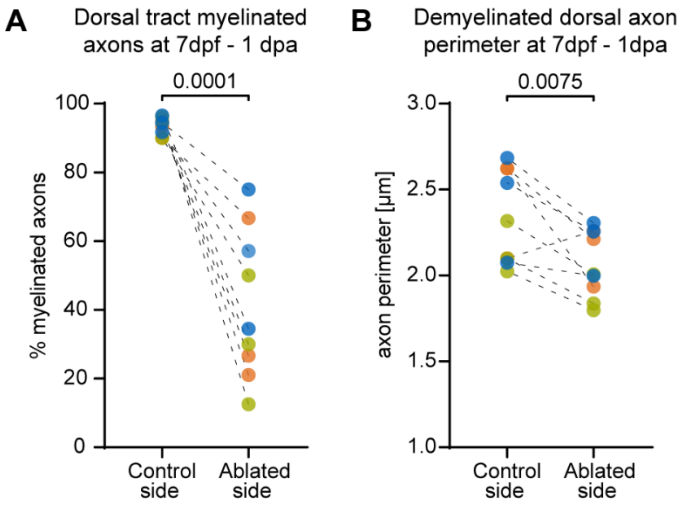

Figure 3.24 Decrease in axon perimeter following its demyelination.

A. Quantification of the myelination of the largest axons per section, set so the control side axons are at least 90% myelinated. Paired t-test. P-value depicted in the graph.
B. Quantification of perimeter of the largest axons per section, set to match the number of large-calibre axons of the control side that are at least 90% myelinated. Paired t-test. P-value depicted in the graph.

First, focusing on the dorsal tract, I selected and analysed the 50 largest calibre axons by visual inspection. I found that 93.48±2.44% of the largest axons of the control side are myelinated. Equally large axons are significantly less myelinated in the ablated side (41.5±21.6% myelinated, paired t-

test, p = 0.0001, Figure 3.24A). Because the fish is bilaterally symmetric, it makes sense to assume that the number of myelinated axons in the dorsal tract of both sides is the same. I can then directly compare the largest axons of both control and ablated dorsal tract in terms of axon perimeter and assume that any observed difference is a direct outcome of demyelination. Indeed, the average perimeter of large spinal cord axons decreases, from 2.34±0.28μm in the control side to 2.07±0.20μm in the ablated side already by 1d post-ablation (7 dpf) (paired t-test, p = 0.0075 - Figure 3.24B).

This indicated that even already at 1d post-ablation, structural changes are triggered within the axon that affect its size and lead to perimeter decrease. It is known that smaller calibre axons are less likely to get myelinated compared to larger calibre ones. This could potentially be one reason newly differentiated oligodendrocytes do not show preference or bias in myelinating demyelinated axons.

Taken together, I was able to use KillerRed to ablate individual oligodendrocytes *in vivo*. The ablations induce rapid cell death and cause minimal bystander damage. Phagocytes are quickly attracted to the lesion site. Oligodendrocyte ablations lead to the creation of a lasting myelin lesion and only partial recovery by 13 dpf, both in terms of cell numbers as well as myelin. TEM analysis of the localization of myelinated axons within the spinal cord, showed that newly added oligodendrocytes do not show a preference between demyelinated and previously unmyelinated axons. Lastly, I was able to show that demyelination decreases axonal calibre, potentially being one reason that remyelination of these axons is not preferable. In conclusion, I can infer from these data that the dominating phenomenon in my ablation system is still the ongoing developmental myelination and oligodendrogenesis and the highly targeted multi-cell ablations that I am causing are potentially not enough to cause enhanced regenerative responses and extensive remyelination.

3.3 Dynamics and regulatory mechanisms underlying positioning of nodes of Ranvier.

Myelin does not only need to be wrapped around the correct axons. For an axon to function properly, the number and length of myelin sheaths need to be in the right position that determines node position. By definition, the node of Ranvier is the short non-myelinated gap between two consecutive myelin sheaths. The length of myelin sheaths (or the distance between consecutive nodes – internode length) of individual axons is one of the main factors affecting conduction velocity (Brill et al., 1977). It is also known that internode length along individual axons can be highly variable (Auer et al., 2018; Ford et al., 2015; Tomassy et al., 2014). However, the mechanisms that guide nodal spacing along individual axons are not well understood.

It has been described that myelin sheath growth (and thus length) can be affected by neuronal activity (Baraban et al., 2018; Krasnow et al., 2018), which can in part explain some of the differences in internodal distance. In recent years, research has focused on different myelination patterns, especially those that appear on partially myelinated axons. (Tomassy et al., 2014). It is important to note that myelination of individual axons does not happen instantaneously, but it can take a long time. This fact raises the question if partially myelinated axons are a final myelination state, or if it is a transient one towards full myelination. Importantly, however, myelin sheaths are not longer along partially myelinated axons compared to fully myelinated ones, even though more of the axonal surface is available. This partial myelination seems to be persistent (as visualised by *in vivo* time-lapse microscopy) and can also be restored following demyelination (Auer et al., 2018; Snaidero et al., 2020). Moreover, in the auditory system of gerbils, internode length shows a highly specific and stereotypic pattern, with myelin sheaths gradually getting shorter from the proximal to the distal parts of the axons (Ford et al., 2015). In this gerbil system, it is exceedingly difficult to envision a glial mechanism that could modulate the formation of such a complex pattern along great distance.

The presence of such different myelination modes as well as the fidelity with which they can be restored highlights a potential for individual axons to intrinsically regulate these patterns, by regulating the placement of nodes of Ranvier along their length. I wondered if and how the node position can be pre-determined along single axons.

3.3.1 Transgenic reagents to label nodes of Ranvier in vivo by live cell imaging

Nodes of Ranvier have been thoroughly researched both in the CNS and the PNS since they were first described. By definition, the node of Ranvier is the short non-myelinated gap between two consecutive myelin sheaths. Nodes are areas rich in voltage-gated sodium channels. These transmembrane proteins are held in position by interacting with elements of the axonal cytoskeleton, βIV-spectrin and AnkyrinG. The node area is also rich in transmembrane adhesion molecules like neuronal neurofascin (Nfasc-186 in mammals, Nfasca in zebrafish) which are also described to interact with the cytoskeleton as well as with proteins of the extracellular matrix, like the GPI-anchored, membrane associated contactin1a (cntn1a). In total, the node of Ranvier is a complex interface with elements spanning the axonal cytoskeleton, the transmembrane and the membrane-associated extracellular matrix (Stathopoulos et al., 2015).

In order to label nodes of Ranvier *in vivo*, I collaborated with my colleague Franziska Auer. Together, we analysed the expression pattern of three constructs that are designed to label nodes or Ranvier albeit being differentially localized, adapted for us in zebrafish *in vivo*:

the GPI-anchored adhesion molecule contactin1a with EYFP fused to its N-terminus (EYFP-cntn1a) (Koudelka et al., 2016).

the intracellular Ankyrin G targeting motif of zebrafish NaV1.2 (EYFP-NaV-II-III) (Garrido et al., 2003).

and neuronal Neurofascin (Nfasca) as a transmembrane protein with a C-terminal fusion of EYFP (Nfasca-EYFP) (Auer et al., 2018)

Utilizing these 3 different constructs allows me to probe for myelination-related changes on the axon that can happen as a result of interactions either from the extracellular matrix (EYFP-cntn1a and Nfasca-EYFP) or the cytoskeleton (EYFP-NaV-II-III and Nfasca-EYFP).

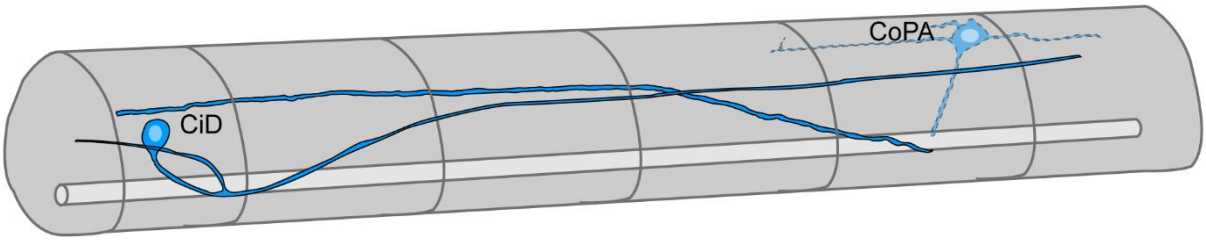

Figure 3.25 Trajectories of CoPA and CiD axons in the spinal cord.

Illustration demonstrating the relative trajectories and distinct morphologies of CoPA and CiD interneurons within the spinal cord.

In fully myelinated axons (CoPA, Figure 3.25), EYFP-cntn1a, designed to be extracellularly tethered to the axonal surface, was completely absent from myelinated parts of the axon and was solely localized at the nodes of Ranvier (confirming Koudelka et al. 2016 – Figure 3.26A, A'). EYFP-NaV-II-III, designed to target the nodes via interaction with AnkyrinG and the cytoskeleton, is enhanced at the sites of the nodes but retains some fluorescence under the myelin sheath (Figure 3.26B, B'). Similar to EYFP-cntn1a, Nfasca-EYFP, a transmembrane adhesion molecule, was completely absent from myelinated segments along the axon and was only present at the nodes of Ranvier (Figure 3.26C, C').

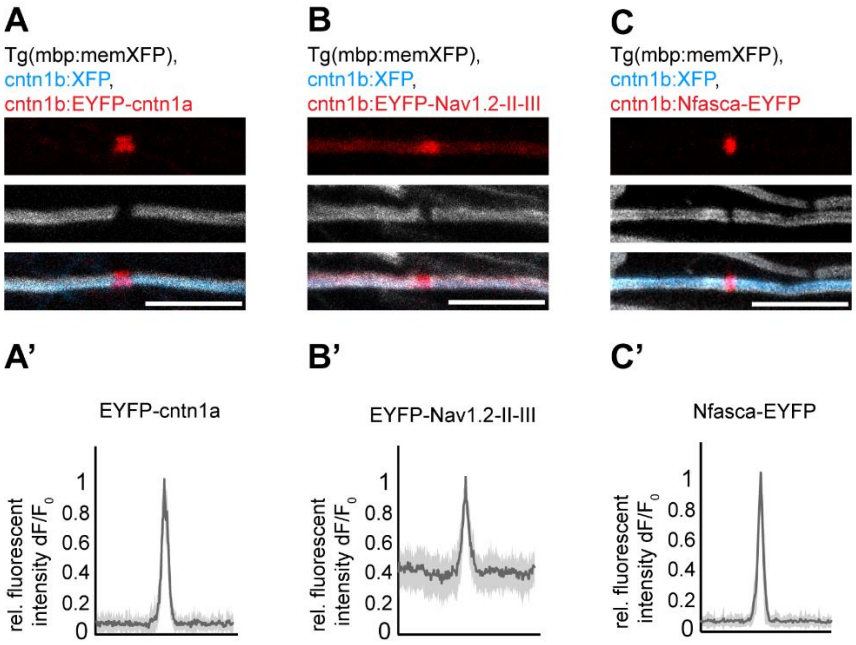

Figure 3.26 Localization of transgenic node of Ranvier reporters along myelinated axon stretches.

A. Confocal image of EYFP-cntn1a on an individually labelled myelinated with all myelin labelled. Scale bar: 10 µm. **A'** Fluorescence intensity traces of EYFP-cntn1a around the node. Bold lines represent the mean and shaded areas the SD. **B.** Confocal image of EYFP-NaV-II-III on an individually labelled myelinated axon with all myelin labelled. Scale bar: 10 µm. **B'** Fluorescence intensity traces of EYFP-NaV-II-III around the node. Bold lines represent the mean and shaded areas the SD.
C. Confocal image of Nfasca-EYFP on an individually labelled myelinated axon with all myelin labelled. Scale bar: 10 µm. **C'** Fluorescence intensity traces of Nfasca-EYFP around the node. Bold lines represent the mean and shaded areas the SD.

I then analysed a partially myelinated neuronal subtype (CiD, Figure 3.25), which could be in this state temporarily until they are fully myelinated but could also remain partially myelinated for prolonged periods of time. On partially myelinated axons, EYFP-cntn1a is absent from the myelinated part and appears diffused on the non-myelinated part (Figure 3.27D, D'). EYFP-NaV-II-III localizes similarly to its fully myelinated localization, having enhanced fluorescence in the non-myelinated segment compared to the myelinated (Figure 3.27E, E'). Lastly, Nfasca-EYFP is again excluded from underneath the myelin sheath and appears diffuse on the non-myelinated part. Interestingly, unlike EYFP-cntn1a, its expression is not completely diffused, but appears as prominent aggregation separated by faint diffuse signal (Figure 3.27F, F').

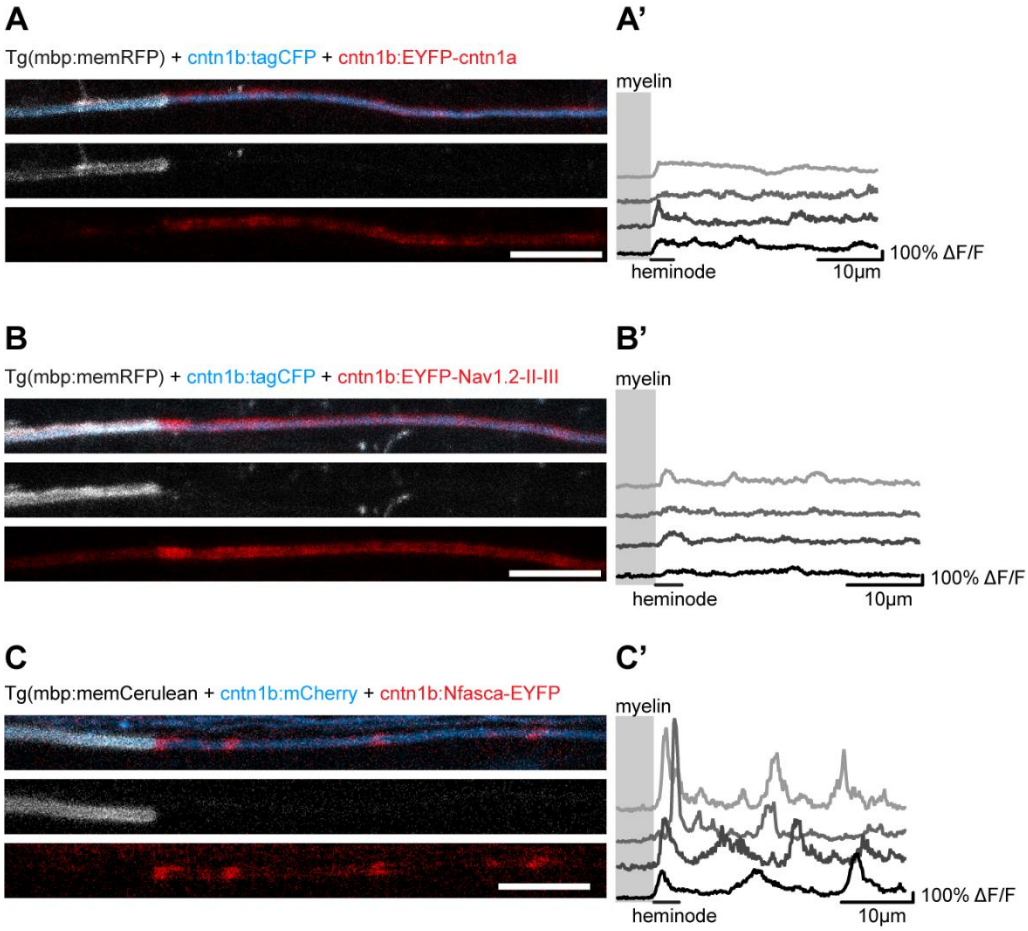

Figure 3.27 Localization of transgenic node of Ranvier reporters along myelinated axon stretches.

A. Confocal image of EYFP-cntn1a along an individually labelled partially myelinated axon with all myelin labelled. Scale bar: 10 µm. **A'** Fluorescence intensity traces of EYFP-cntn1a along four example axons. Grey box indicates the presence of myelin.
B. Confocal image of EYFP-NaV-II-III along an individually labelled partially myelinated axon with all myelin labelled. Scale bar: 10 µm. **B'** Fluorescence intensity traces of EYFP-NaV-II-III along four example axons. Grey box indicates the presence of myelin.
C. Confocal image of Nfasca-EYFP along an individually labelled partially myelinated axon with myelin labelled. Scale bar: 10 µm. **C'** Fluorescence intensity traces of Nfasca-EYFP along four example axons. Grey box indicates the presence of myelin. Note the prominent spikes indicating Nfasca-EYFP accumulations.

Some neuronal subtypes display unusual localization of nodal markers.

The localization of nodal markers was as described in all CiD and CoPA axons that we analysed. However, two neuronal types showed different localization patterns. One is the Rohon-Beard neuron, a sensory cell which is very rarely myelinated (Nelson et al., 2020). The second is a Mauthner axon. As already described, the Mauthner exhibits a different myelination pattern which lacks nodes of Ranvier, having exposed only its synaptic boutons that are found along its length.

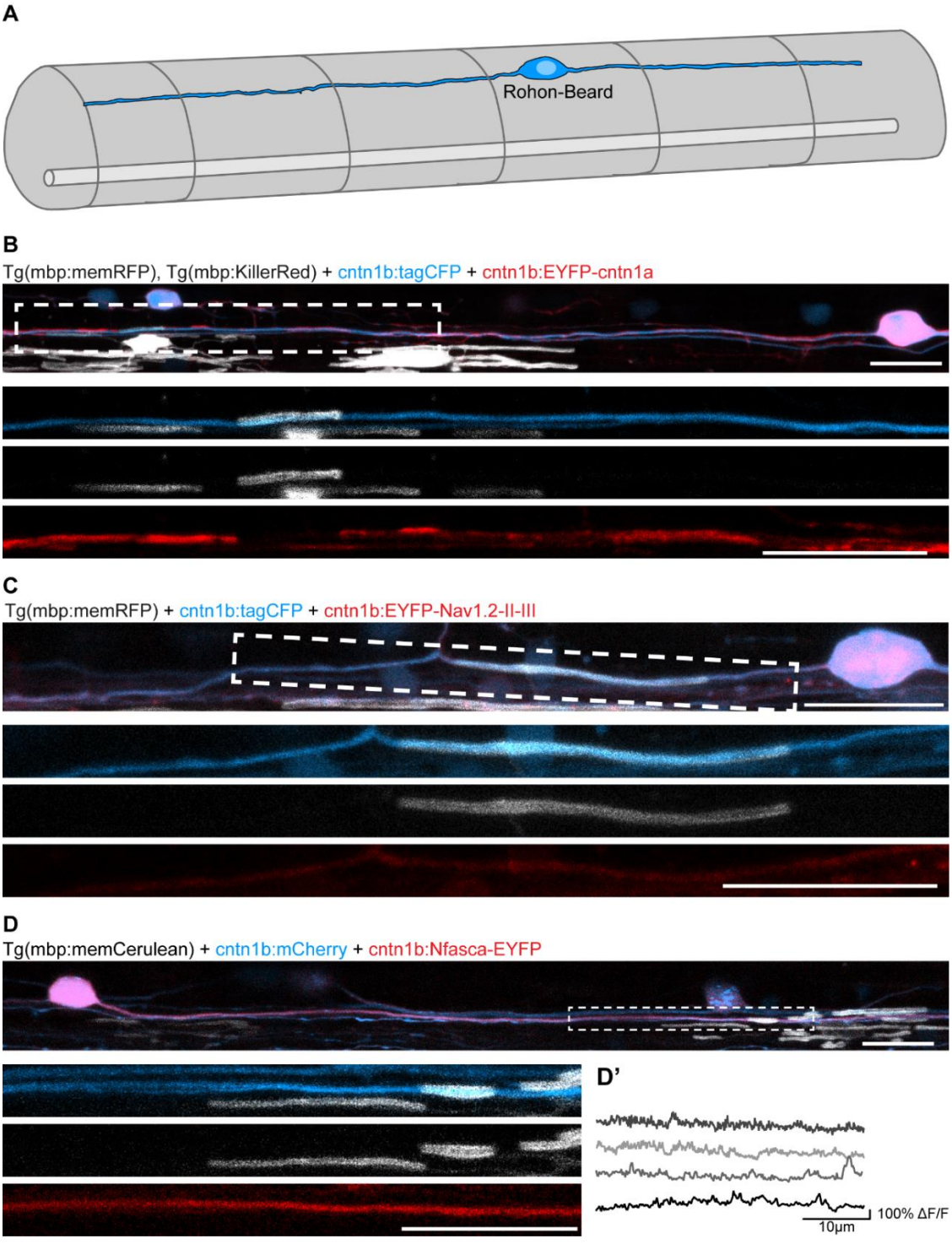

Figure 3.28 Localization of transgenic node of Ranvier reporters along Rohon-Beard processes.

A. Cartoon –anatomy of a Rohon-Beard neuron in the spinal cord.
B. Example confocal image of EYFP-cntn1a along a Rohon-Beard myelinated segment with myelin labelled. Note the exclusion of EYFP-cntn1a under the myelinated segment. Scale bars: 20 µm.
C. Example confocal image of EYFP-NaV-II-III along a Rohon-Beard myelinated with all myelin labelled. Note the lack of contrast between myelinated and non-myelinated segments of the axon. Scale bar: 20 µm.
D. Example confocal image of Nfasca-EYFP along a Rohon-Beard myelinated with all myelin labelled. Note the lack of contract between myelinated and non-myelinated segments of the axon as well as the lack of clustering. **D'** Example traces of Nfasca-EYFP fluorescent intensity along Rohon-Beard processes. Scale bars: 20 µm.

On Rohon-Beard neurites, EYFP-cntn1a is excluded from the myelinated segment and appears diffused in the rest of the axon (Figure 3.28B). EYFP-NaV-II-III is completely diffused, even under the myelin sheath with no contrast to the non-myelinated part of the axon (Figure 3.28C). Lastly, Nfasca-EYFP, like EYFP-NaV-II-III, is not excluded from the myelinated segments and it shows a complete diffusion (Figure 3.28D).

In Mauthner axons, EYFP-cntn1a is localized at the surface of their prominent synaptic boutons (Figure 3.29B). EYFP-NaV-II-III appears again diffused, but with enhanced labelling of the synaptic boutons (Figure 3.29C). Finally, Nfasca-EYFP shows a localization like EYFP-cntn1a, covering the surface of the en passant synapses (Figure 3.29D).

To summarize, all three constructs labelled nodes of Ranvier accurately, with only EYFP-NaV-II-III having relatively poor contrast between the node and the myelinated segments of the axon. I also saw that EYFP-cntn1a and EYFP-NaV-II-III appear diffused along non-myelinated parts of the axon, while Nfasca-EYFP formed distinct aggregates, retaining some diffused expression in-between them.

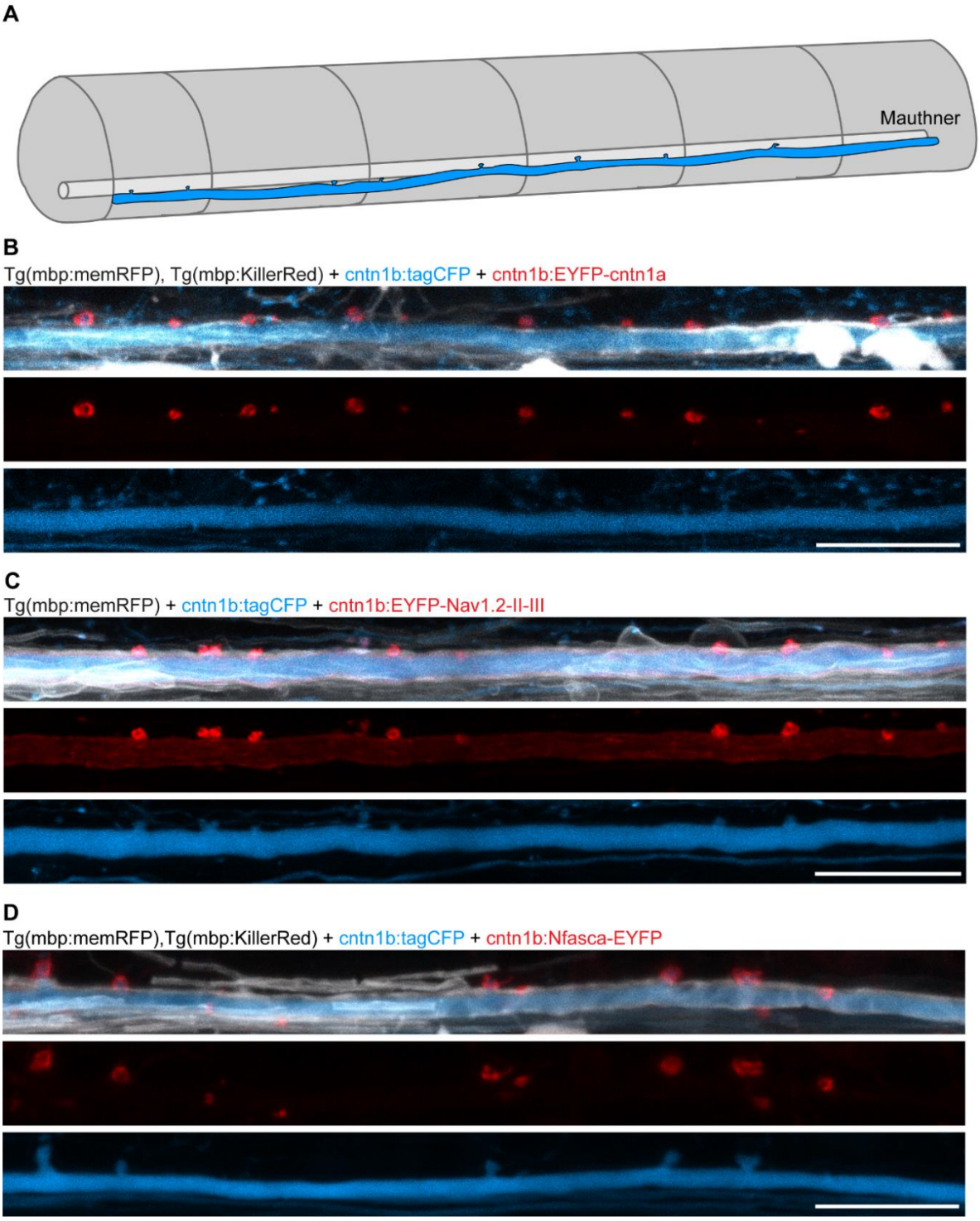

Figure 3.29 Localization of transgenic node of Ranvier reporters along the Mauthner axon.

A. Cartoon –anatomy comparison of Mauthner axon in the spinal cord
B. Example confocal image of EYFP-cntn1a along the Mauthner axon with all myelin labelled. Note the exclusion of EYFP-cntn1a to the en passant synapses. Scale bar: 20 µm.
C. Example confocal image of EYFP-NaV-II-III along the Mauthner axon with all myelin labelled. Note presence of diffused protein and the enhanced localization at the en passant synapses. Scale bar: 20 µm.
D Example confocal image of Nfasca-EYFP along the Mauthner axon with all myelin labelled. Note the exclusion of Nfasca-EYFP to the en passant synapses. Scale bar: 20 µm.

3.3.2 Nfasca-EYFP forms clusters prior to myelination at positions of future node formation

When analysing partially myelinated axons, we noted the prominent formation of clusters of Nfasca-EYFP along non-myelinated segments. This prompted us to further characterize these clusters and analyse their dynamics.

First, we wanted to describe the characteristics of Nfasca-EYFP clusters and compare them to Nfasca-EYFP-labelled nodes of Ranvier. We found that the fluorescent intensity of clusters is comparable to that of nodes and significantly stronger than that of the inter-cluster unmyelinated parts (rel. Nfasca fluorescence at node=0.78±0.15 vs. 0.53±0.22 at cluster vs. 0.09±0.03 at inter-cluster vs. 0.02±0.03 under myelin sheath n=7/7 axons/animals, p=0.652/p<0.001/p<0.001, Kruskal-Wallis test; Figure 3.30A, B).

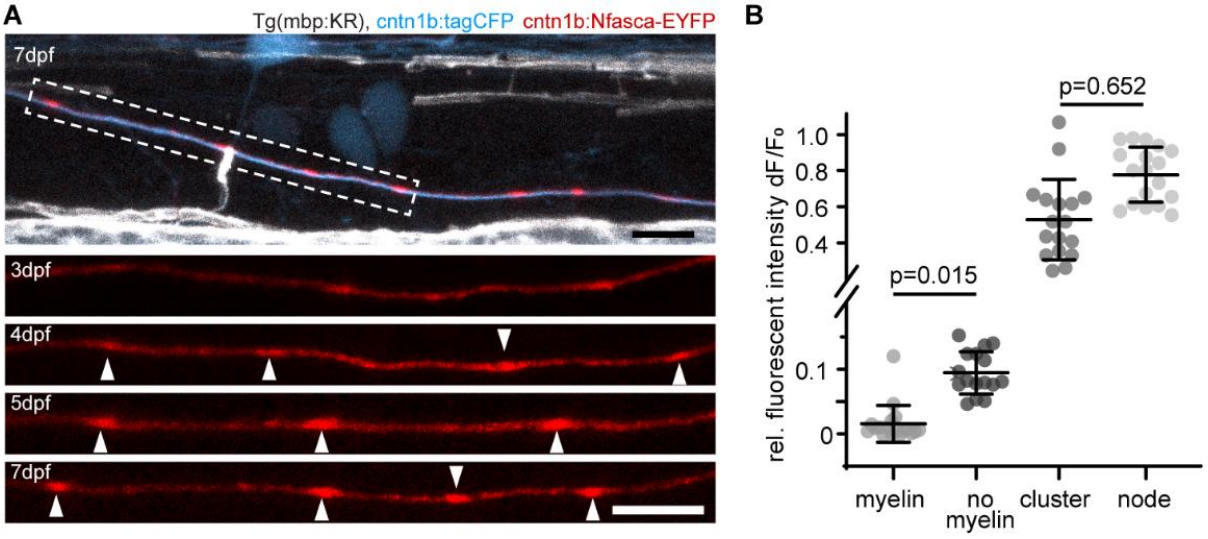

Figure 3.30 Comparison of relative fluorescence of clusters and nodes

A. Confocal images of an individually labelled unmyelinated axon co-expressing Nfasca-EYFP in a myelin reporter full transgenic background. Panels on the bottom show Nfasca-EYFP localization along unmyelinated axon stretch indicated by the dashed box on the top image over time. Scale bar = 10 µm.
B. Quantification of fluorescence intensities at regions on analysed axons. Data are expressed as mean ± SD (Kruskal–Wallis test, p-values are given in the figure). Data acquired by Franziska Auer.

The clusters appeared evenly spaced with an average inter-cluster distance of 18.2±8 µm (n=45/6/4 inter-clusters/axons/animals; compare with average internodal distance of fully myelinated axons:

30.9±13.2 µm, n=25/4/4 internodes/axons/animals, p<0.001, Mann-Whitney test; Figure 3.31A). The same axons have more clusters than nodes on average (0.62±0.23 nodes/clusters, n=7 axons/fish-Figure 3.31B). Time-lapse microscopy of non-myelinated axon stretches allowed me to quantify the motility of Nfasca clusters, 2.48±1.93 µm within a day compared to nodes 1.82±1.07 µm (n=33/5 clusters/axons for clusters 31/9 nodes/axons for nodes, p=0.2669, Mann-Whitney test, Figure 3.31C).

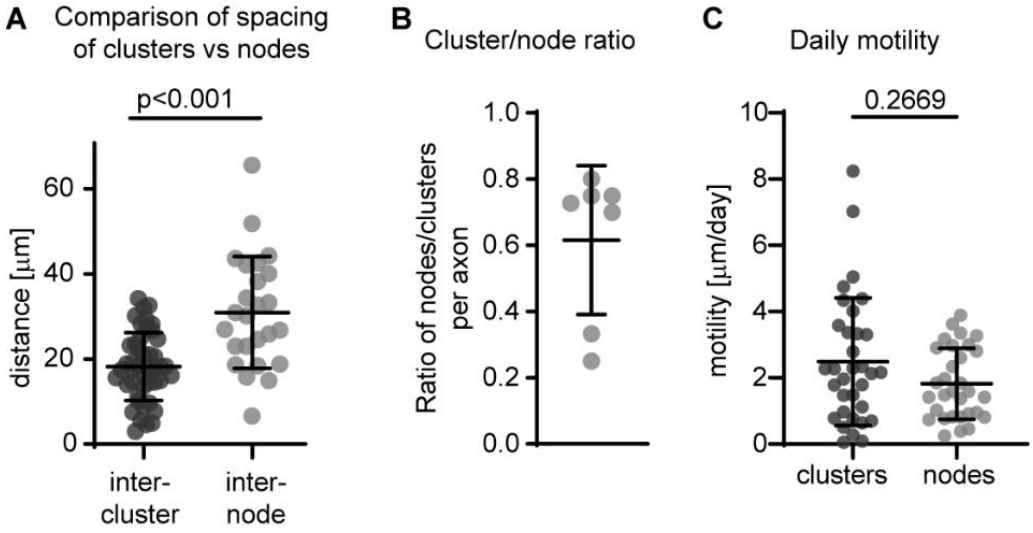

Figure 3.31 Comparison of relative properties of clusters and nodes

A. Quantification of inter-cluster distance and internodal distance along the same axon. Data are expressed as mean ± SD (Mann-Whitney test, p value shown in the graph).
B. Quantification of the ratio of the number of nodes at the end of analysis over the number of clusters at the beginning along single axons. Data are expressed as mean ± SD.
C. Quantification of Nfasca cluster motility per day compared to nodes. Mann-Whitney test. P value shown in the graph. Data are expressed as mean ± SD. Data acquired by Franziska Auer.

Moreover, since the number of clusters prior to myelination exceeds the number of nodes after myelination along the same axons, we wanted to quantify the number of clusters that disappear during the timeframe of our experiments. We found that only a small number of 12.9% (8/62) of all clusters observed disappeared between timepoints (Figure 3.32A, B).

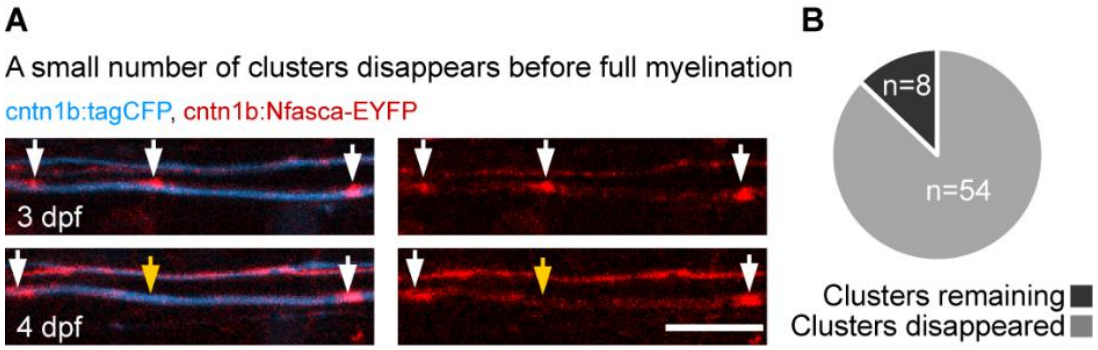

Figure 3.32 Frequency of cluster disappearance

A. Confocal images of an axon co-expressing Nfasca-EYFP and tagCFP at 3 and 4 dpf. White arrows indicate individual clusters. Yellow arrow indicates the loss of a cluster. Scale bar = 10 µm.
B. Quantification of the frequency of cluster disappearance. Data acquired by Franziska Auer.

Another observation that we made is that some sheath ends that are unilaterally isolated from neighbouring sheaths show Nfasca-EYFP-labelled heminodes, while others do not (Figure 3.33A). We quantified that 79% of isolated sheath ends with no neighbour showed a heminodal accumulation of Nfasca (75/95 heminodes, n=22/21 axons/animals - Figure 3.33B). The remaining 21% of myelin sheaths that did not show heminodal Nfasca were overall shorter than the ones with heminodal Nfasca (35±12 µm vs. 23±14 µm, n=58/16 sheaths, Figure 3.33C). This suggests that shorter sheaths, being younger, may have not yet encountered a cluster as they grow along the axon.

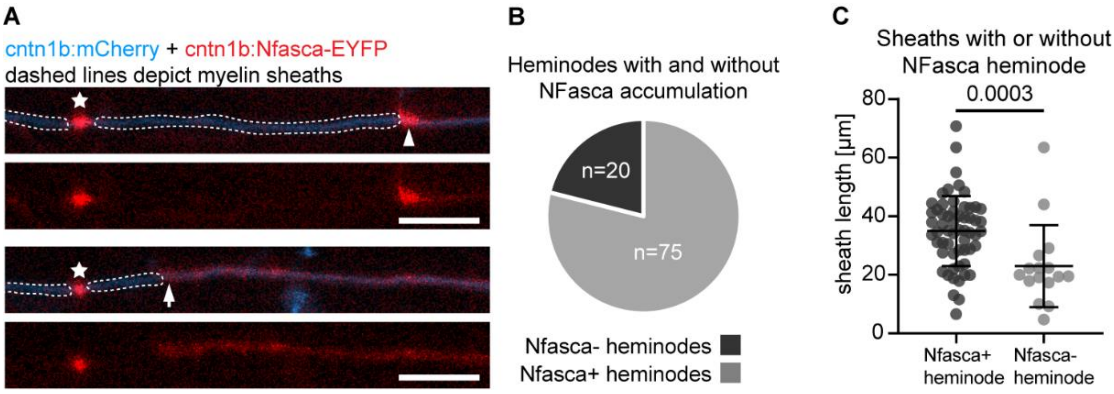

Figure 3.33 Frequency of Nfasca-EYFP heminodal labelling and correlation to myelin sheath length.

A (Top) Example confocal image of myelin sheath carrying a Nfasca-EYFP-positive heminode (arrowhead). (Bottom) Example confocal image of myelin sheath without Nfasca-EYFP-positive heminode(arrow). Asterisk indicates the presence of a node. Dashed areas represent the myelin sheaths. Scale bar = 10 µm.
B. Quantification of the frequency of heminodes with adjacent Nfasca accumulation.
C. Quantification of sheath length for sheaths with heminodal neurofascin compared to the ones without. Data are expressed as mean ± SD (Mann-Whitney test, p value shown in the graph). Data acquired by Franziska Auer.

Clusters of voltage-gated sodium channels along non-myelinated axons have been observed *in vitro* (M. Kaplan et al., 1997; M. R. Kaplan et al., 2001), as well as in histological analysis of mouse and rat CNS (S. A. Freeman et al., 2015) The observation of Nfasca-EYFP accumulations in partially myelinated axons together with their absence from the rarely myelinated Rohon-Beard processes prompted us to investigate further this clustering phenomenon and especially the possibility that cluster position could indicate future node position.

To do so, we focused on timelines of individual axons from a non-myelinated or partially myelinated to a fully myelinated state. We marked each cluster and analysed its fate at the end of the experiment (Figure 3.34B).

We found that 71% (22/31) of all clusters indeed functioned as stop signals for myelin growth, leading to the formation of a node (14/31) or a stable heminode (8/31) (Figure 3.34C, D). The remaining 29% (9/31) were translocated as motile heminodes on the growing myelin (Figure 3.34A, D).

Furthermore, looking at the same data but in reverse sequence, we analysed the origin of each node and whether it has formed at a position of a cluster, a heminode or if it has formed at a position with no distinguishable accumulation.

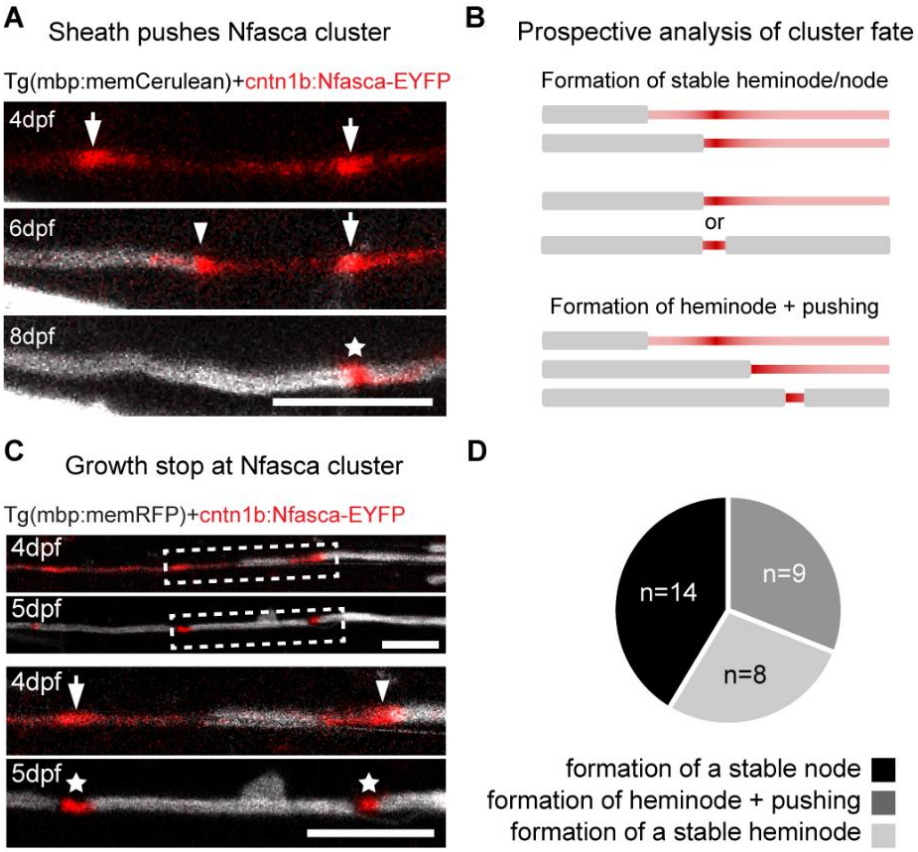

Figure 3.34 Analysis of cluster fate during myelination

A. Confocal images of an axon expressing Nfasca-EYFP in a full transgenic myelin reporter background at 4,6 and 8 dpf. Arrows indicate clusters, arrowhead a heminode and star indicated nodes. The left cluster is visibly pushed by the growing myelin sheath. Scale bar = 10 µm.
B. Cartoon showing the possible cluster fates. (Top) Cluster position is maintained during myelination and correspond to a heminode or node (stable). (Bottom) Myelin sheath pushes cluster as a motile heminode.
C. Confocal images of an axon expressing Nfasca-EYFP in a full transgenic myelin reporter background. Bottom images correspond to the stretch highlighted by dashed box on the top images. Arrow indicates a cluster, arrowhead a heminode and star indicated nodes. Notably both cluster and heminode stay in the position where a node forms. Scale bar = 10 µm.
D. Quantification of the frequency of cluster fates observed.
Data acquired by Franziska Auer.

We found that 55% of all nodes analysed (18/33 nodes in 7 animals) had a cluster at the same position prior to the respective axon's myelination. In 12% of cases (4/33), a heminode preceded the formation of the node, while for the remaining 33% of nodes (11/33), there was no indication of a prior cluster or heminode at the position the node appeared in. Using retrospective analysis of nodal origin, I was able to verify that EYFP-cntn1a and EYFP-NaV-II-III did not aggregate prior to myelination. Indeed, for these nodal reporters, 21% of cntn1a (4/19 nodes in 5 animals) and 27% of NaV-II-III (7/26 nodes in 7 animals) labelled nodes had a heminode at the position of the later node,

but for the remaining nodes, no indications for clustering were detectable prior to the onset of myelination in the position the node would be formed (Figure 3.35).

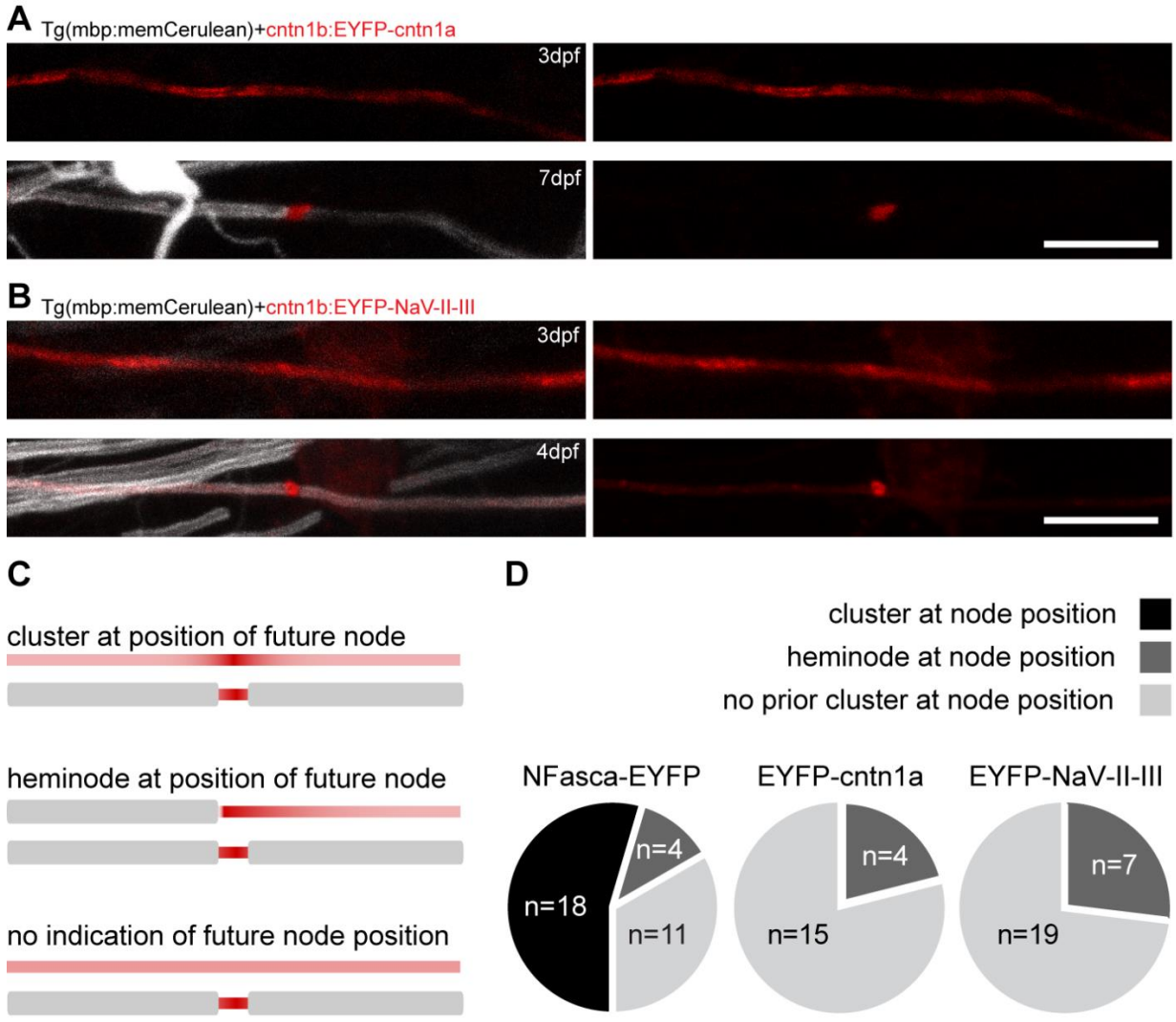

Figure 3.35 Retrospective analysis of node origin during myelination

A. Example timeline of an axon expressing EYFP-cntn1a where there is no indication of cluster presence at the future position of a node of Ranvier. Scale bar = 10 µm.
B. Example timeline of an axon expressing EYFP-NaV-II-III where there is no indication of cluster presence at the future position of a node of Ranvier. Scale bar = 10 µm.
C. Cartoon showing the 3 origins of nodes, having a cluster at node position, a heminode at the node position or having no accumulation at the node position **C.** Cartoon showing the 3 origins of nodes, having a cluster at node position, a heminode at the node position or having no accumulation at the node position.
D. Quantification of node origin for Nfasca-EYFP, EYFP-cntn1a and EYFP-NaV-II-III. Notably, only Nfasca-EYFP forms clusters that can correlate with future node position. Nfasca data acquired by Franziska Auer.

To conclude, we were able to analyse and characterize Nfasca-EYFP cluster formation and dynamics *in vivo* along individual axons during the shift from partially myelinated to fully myelinated

state. In 70% of all cases, the presence of a cluster seemed to determine the position of future node formation, indicating possible axonal contribution in node of Ranvier placement.

3.3.3 Designing CRISPR-Cas9 Nfasca mutagenesis

Since Nfasca seemed to play a role in guiding node of Ranvier position we wanted to investigate how node position is affected upon Nfasca loss. Neurofascin is produced in mammals by the expression of *nfasc* gene. This locus is responsible for the creation of different transcripts, including NFasc-186, the neuronal isomorph and NFasc-155, the oligodendrocyte-specific isomorph via alternative splicing. In the beginning of designing this approach, it was not known that in zebrafish, the homologs of these two proteins are products of two different genes, Neurofascin-a producing the neuronal isomorph (*nfasca)* and Neurofascin-b producing the glial isomorph *(nfascb)* (Klingseisen et al., 2019). So, in order to selectively target only the neuronal isomorph, we designed the guide RNA to target the Mucin domain, which is present exclusively in the extracellular part of neuronal neurofascin and is absent from the glial isomorph.

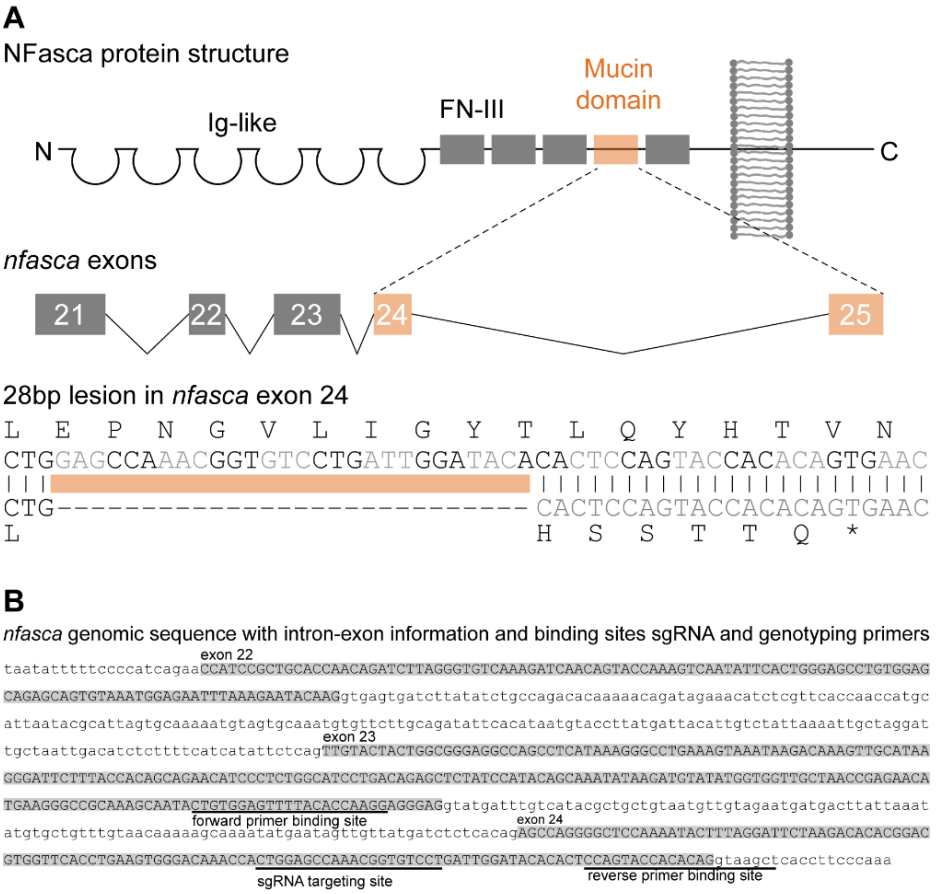

Figure 3.36 CRISPR-Cas9 targeting of nfasca gene in order to create site-specific mutation.

A. Cartoon illustrating the targeting strategy for Nfasca mutagenesis.
B. Part of the nfasca genomic sequence around the sgRNA target site. Intron sequences are shown in lowercase, exon sequences are capitalized and highlighted in grey. Genotyping primer sequences and gRNA recognition site are underscored.

Using this guide RNA in combination with Cas9 expression, we were able to introduce mutations within the *nfasca* locus. We identified a 28bp deletion within the Mucin domain, that led to a premature stop codon, creating a truncated peptide that lacks the transmembrane domain and is therefore unable to retain its localization and interaction with the cytoskeleton (Figure 3.36). We have not investigated the fate of this peptide.

Knock-out mice for Neurofascin do not survive past P7 (Sherman et al., 2005). Surprisingly, homozygous animals for the 28bp deletion (Δ28/Δ28) were viable until adulthood. They show no macroscopic or behavioural phenotypes, they are fertile and show normal lifespan.

First, by immunostaining against the intracellular C-terminus of Nfasca, I confirmed its absence in homozygous mutant fish. In heterozygous and wildtype samples, this antibody strongly labels nodes or Ranvier (Figure 3.37A, A'). Genotyping via PCR was used to identify wildtype, heterozygous (Δ28/+) and homozygous (Δ28/ Δ28) individuals (Figure 3.37B).

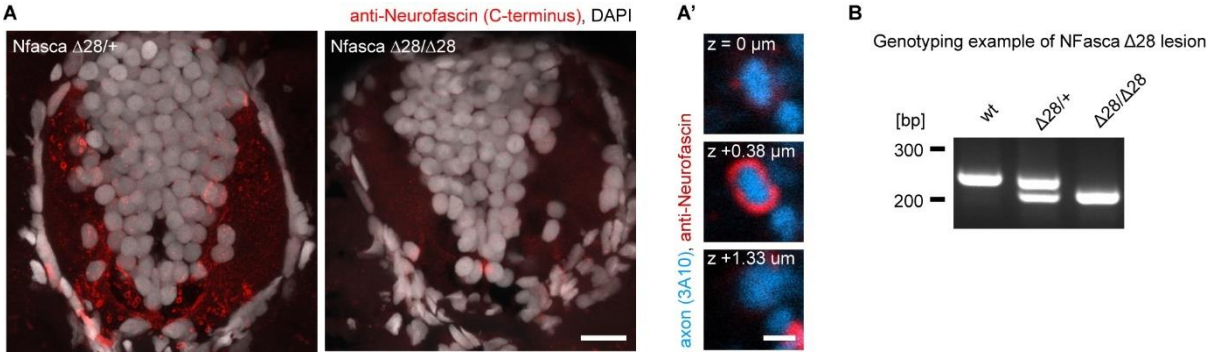

Figure 3.37 Identification and validation of the Δ28 deletion

A. Immunohistochemistry against Nfasca on spinal cord cross sections in heterozygous and homozygous Nfasca mutant zebrafish. Scale bar = 10µm. **A'**. Cross-sectional views of a single 3A10-labelled axon showing Neurofascin localization at different z-positions. Scale bar = 1µm.
B. Example of genotyping PCR results showing wildtype, heterozygous (Δ28/+) and homozygous (Δ28/Δ28) mutants for the NFasca Δ28.

Microscopic *in vivo* analysis of overall myelin overview shows that myelination seems to occur normally in Δ28/Δ28 animals, with nodes or Ranvier appearing normal (Figure 3.38A). The localization of EYFP-cntn1a as well as EYFP-Nav-II-III also remains unaffected as these proteins still label nodes of Ranvier similarly in wildtype and Δ28/Δ28 animals Figure 3.38B, B').

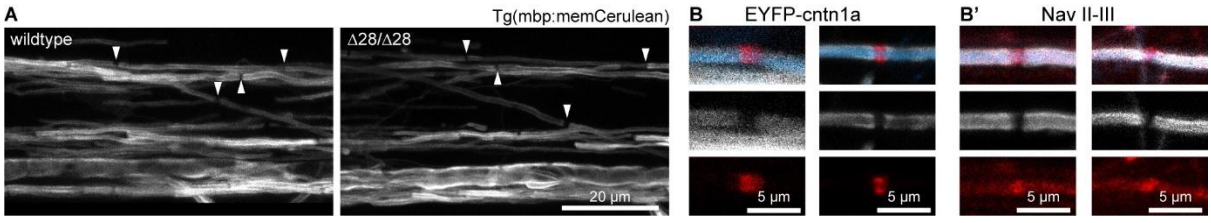

Figure 3.38 Overall myelin as well as nodes of Ranvier appeared normal in Nfasca mutants.

A. Confocal images showing overviews of the spinal cord in a full transgenic reporter line for myelin. Arrowheads highlight node positions. Scale bar = 20 µm.
B. Close-ups from confocal images showing single nodes of Ranvier marked with EYFP-cntn1a in a full transgenic reporter line for myelin in WT (left) and Nfasca mutant zebrafish(right). Scale bar = 5 µm. **B.** Close-ups from confocal images showing single nodes of Ranvier marked with EYFP-NaV-II-III in a full transgenic reporter line for myelin in WT (left) and Nfasca mutant zebrafish(right). Scale bar = 5 µm.

3.3.4 Loss of neuronal neurofascin increases internode distance on single axons.

I focused my analysis on CoPA neurons because their shape is very characteristic, they are among the first to get myelinated (Koudelka et al., 2016) in the dorsal spinal cord and their soma shape and axon trajectory make them very distinguishable.

I used 8-10 dpf mutant larvae that express EYFP-cntn1a in CoPA neurons. By analysing internodal distances of individual CoPA axons, I found a significant 18% increase in internodal distances in Nfasca mutants compared to wildtypes (47.3±7.3 µm in wildtypes vs 55.7±8.4 µm in homozygous mutants in n=9/15 animals, p=0.042, ordinary one-way ANOVA with multiple comparisons - Figure 3.39A-C).

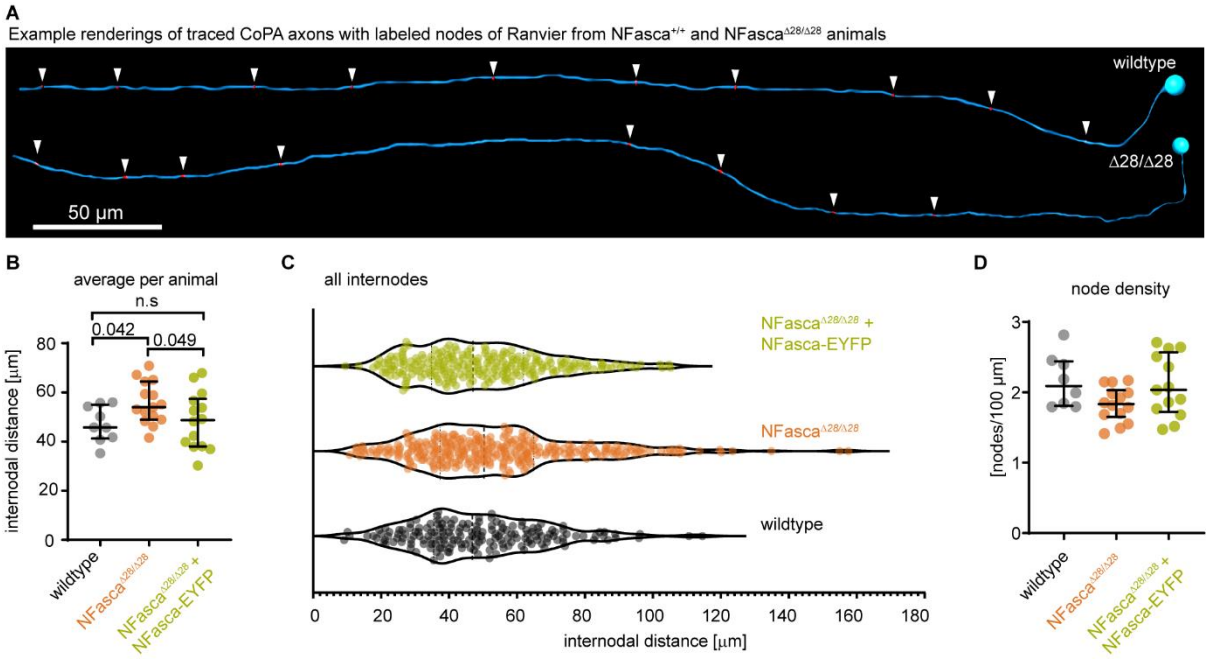

Figure 3.39 Nfasca mutants have significantly longer internodes along single axons.

A. Example traces of node of Ranvier position along two CoPA axons from heterozygous and homozygous Nfasca mutant fish. Arrowheads highlight node positions. Scale bar = 50 µm.
B. Quantification of average internodal distances along single axons per fish in wildtype, homozygous Nfasca mutants and homozygous mutants rescued by Nfasca-EYFP expression (data are expressed as mean ± SD. Ordinary one-way ANOVA, p value depicted in the graph)
C. Graph showing all measured internode distances in wildtype, homozygous Nfasca mutants and homozygous mutants rescued by Nfasca-EYFP expression (data are expressed as median ± quartiles).
D. Quantification of average node density along single axons per fish in wildtype, homozygous Nfasca mutants and homozygous mutants rescued by Nfasca-EYFP expression (data are expressed as mean ± SD.

I then assessed whether overexpression of Nfasca-EYFP construct in Δ28/Δ28 mutants can rescue the internodal distance phenotype. First, I verified that in wildtype fish, Nfasca-EYFP does not alter internode distances by overexpression. I compared CoPA neurons expressing Nfasca-EYFP to CoPA neurons expressing EYFP-cntn1a of the same age (9 dpf). This experiment showed that there was no difference in average internode length per axon, caused by the overexpression of Nfasca-EYFP compared to EYFP-cntn1a (47.4±8.01 μm in WT injected with cntn1a vs 45.6±10.9 μm in WT injected with Nfasca in n=11/10 animals, p = 0.6797, unpaired t test – Figure 3.40A, B).

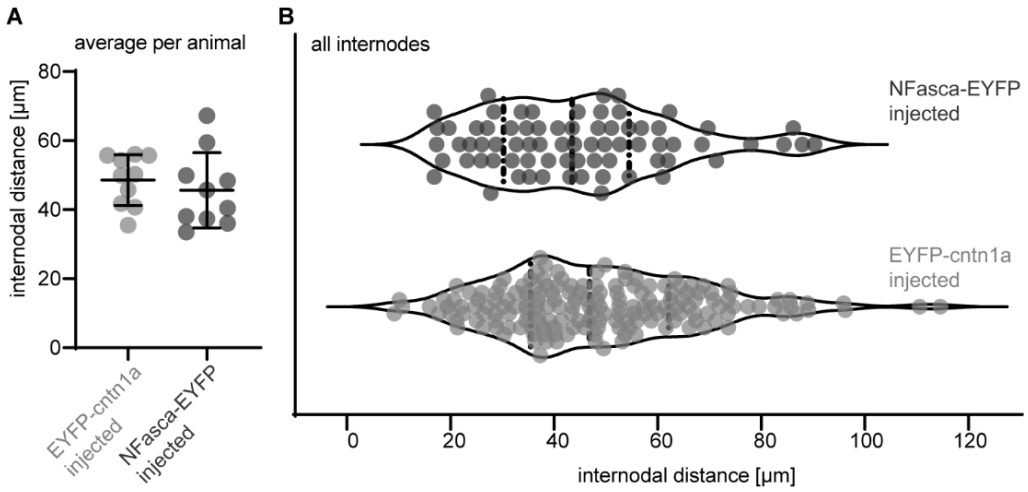

Figure 3.40 Nfasca-EYFP overexpression does not alter individual neuron myelination.

A. Comparison of average internodal distance per animal measured by injected EYFP-cntn1a and by Nfasca-EYFP expression in CoPA neurons. (Data are expressed as mean ± SD).
B. Quantification of all internodal distances measured by injected EYFP-cntn1a and by Nfasca-EYFP expression in CoPA neurons. (Data are expressed as median and quartiles).

Then, I used mutant larvae expressing Nfasca-EYFP in individual CoPA neurons and analysed the internodal distances of each axon along its length. I discovered that this manipulation rescued the previously described phenotype via a significant, 15% reduction of internodal distances (48.5±11.5 μm in 14 animals, p=0.049, ordinary one-way ANOVA with multiple comparisons), while the rescued Δ28/ Δ28 animals were not significantly different than the wildtypes (p=0.757, ordinary one-way ANOVA with multiple comparisons - Figure 3.39B, C).

Lastly, I quantified nodal density as the number of nodes per 100 µm. I found that nodal density slightly decreased in Δ28/Δ28 animals compared to wildtype and that this effect was reversed in rescued Δ28/Δ28 animals (2.16±0.37 nodes/µm in wildtypes vs 1.83±0.25 nodes/µm in homozygous mutants vs 2.09±0.44 nodes/µm in rescued Δ28/Δ28 animals, n=8/14/13 animals respectively, p = 0.078, ordinary one-way ANOVA with multiple comparisons).

Overall, these experiments show that genetic ablation of Nfasca and its dissociation from its cytoplasmic patterns lead to an increase in internodal distances along individual axons. The specificity of this result is further highlighted by the fact that this phenotype can be rescued by simple overexpression of Nfasca-EYFP in homozygous mutant fish. These results further highlight the important of Nfasca in regulating myelination of individual axons.

Myelination delay in Nfasca mutants increases myelin sheath length.

The measurements of internode distance in wildtype and Nfasca mutant animals showed that endogenous Nfasca expression (and thus Nfasca pre-nodal clusters) serve as stop cues for lateral sheath growth. However, another obstacle that can halt lateral sheath growth and thus modulate sheath length is the presence of neighbouring sheaths, competing for myelinating the same axon. In order to test if neighbouring sheaths can halt the elongation of sheaths, they share a node of Ranvier with, I investigated ways to delay myelination, in order to induce sparser myelination on individual axons, where myelin sheaths can grow for longer.

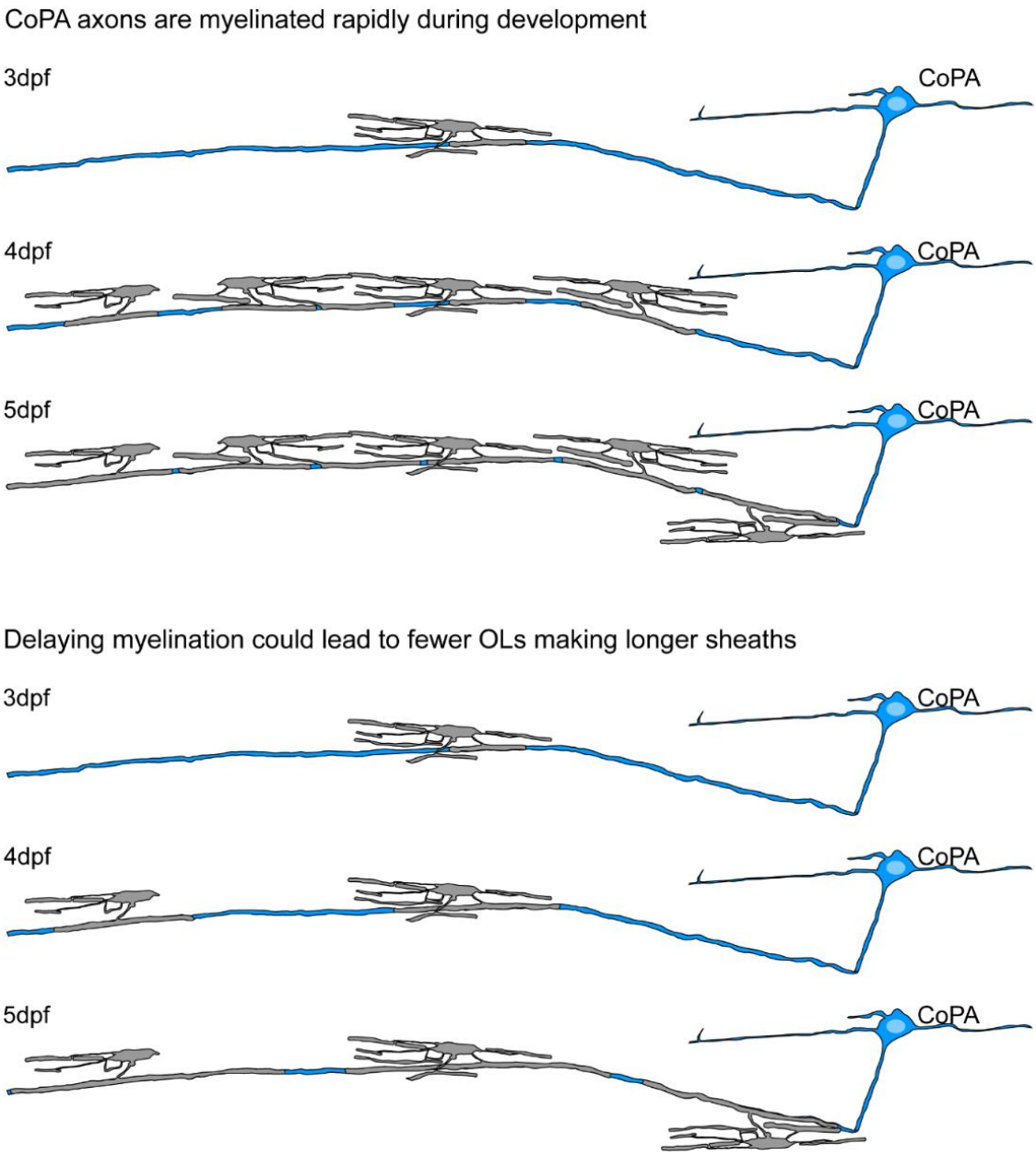

Figure 3.41 Delaying myelination could lead to the production of longer sheaths and thus longer internodal distances.

Illustration of CoPA axons being myelinated over time. CoPA neurons are typically myelinated quickly in development (top). Delaying myelination could lead to the production of longer sheaths by fewer oligodendrocytes (bottom).

To create such an environment, I treated larval zebrafish from 2-5 dpf with (+)-JQ1 (Early et al., 2018), which is known to decrease the amount of myelin in the spinal cord, in order to allow unilaterally or bilaterally isolated sheaths to grow longer. The drug treatment decreased myelination as expected. I focused my analysis exclusively on dorsal and ascending sheaths because these are

more likely to myelinate CoPA axons, which were the focus of my previous analysis (Figure 3.34A). Bulk analysis of the distribution of all ascending and dorsal sheaths measured showed a significant increase in Nfasca mutants compared to wildtypes. The average sheath length per fish was also significantly increased in the mutant compared to the wildtype animals (mean = 65.32±12.52 µm in Nfasca mutants vs mean = 58.75±9.49 µm in WT, n=40/37 Nfasca mutant fish / WT fish, p = 0.0125, Mann-Whitney test - Figure 3.34C).

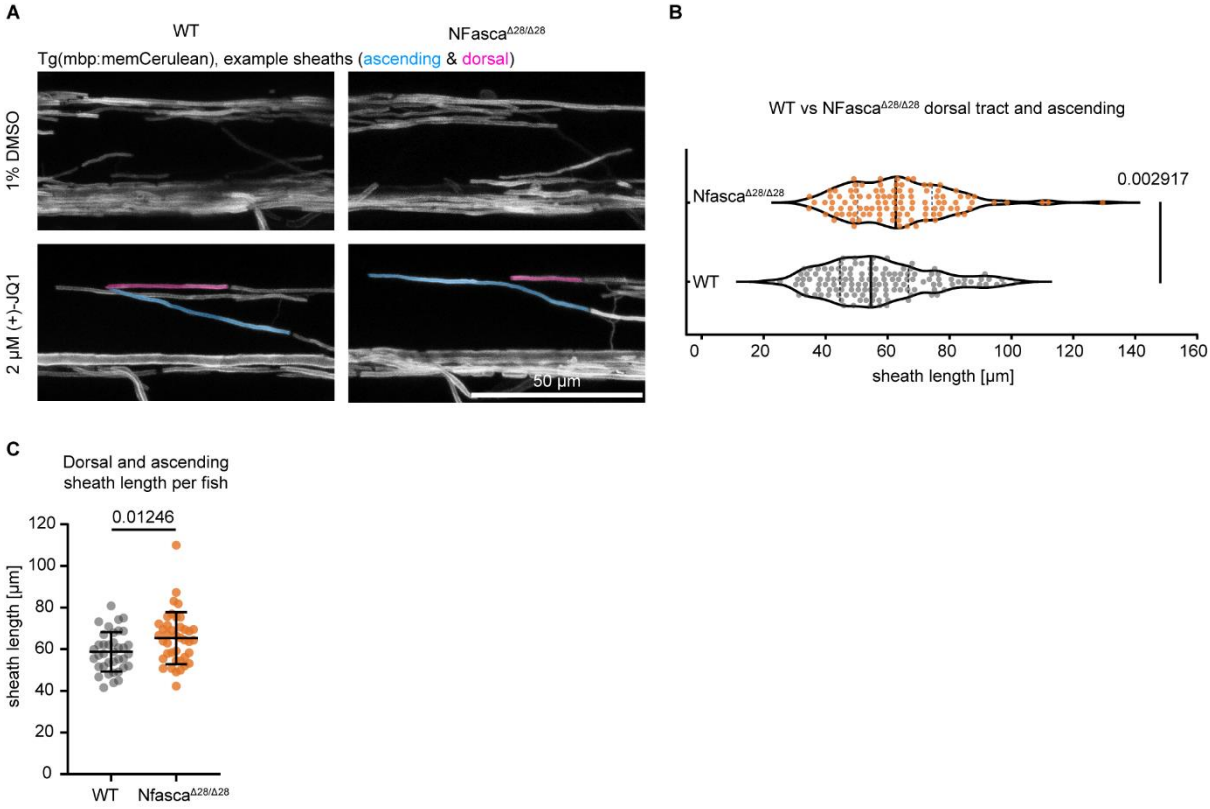

Figure 3.42 Pharmacological delay of myelination leads to longer myelin sheaths in Nfasca mutants.

A. Confocal images showing the effect of (+) JQ1 treatment in sheath density. Dorsal tract and ascending sheaths were pseudo coloured. Scale bar = 50µm.
B. Quantification of sheath length in WT vs NfascaΔ28/Δ28 fish treated with (+)-JQ1 (Data are expressed as median and quartiles. Kolmogorov-Smirnov test, p value depicted in the graph).
C. Quantification of sheath length per fish in WT vs NfascaΔ28/Δ28 fish treated with (+)-JQ1 (data are expressed as mean ± SD, Mann-Whitney test, p value depicted in the graph).

This experiment confirmed the presence of longer myelin sheaths in Nfasca mutants compared to wildtypes thanks to sparser myelin, even though the effect was modest, probably due to the

difference in the age of animals or the age of individual sheaths. Notably, the sheath length observed in treated wildtype animals was on average higher than the internode distance of the same genotype measured previously (mean = 58.75±9.49 µm in the myelination delay experiment vs 47.3±7.3 µm in internode distance experiment), despite the fact that the myelination delay experiment was concluded at 5 dpf, while the internode distance measurements were conducted later, at 9 dpf. While these measurements cannot be directly compared due to the different age of the animals, the result clearly shows that lateral growth of myelin sheaths can also be affected by the presence of neighbouring sheaths as well as by the presence of axonal cues (i.e., Nfasca). However, the pharmacological delay of myelination experiment showed that the result described in the previous sub-chapter is real and independent of the expression of EYFP-cntn1a.

3.4 Node marker localization along individual axons after local demyelination

As I already described in the previous chapters, I was able to describe that Nfasca-EYFP clusters along individual axons prior to myelination, in positions that are in most of the cases instructive for future node position. This could indicate the presence of an axon-intrinsic mechanism that regulates sheath length and the myelination pattern of individual axons. However, in other cases, I observed Nfasca-EYFP clusters pushed by growing myelin segments. In Auer et al. , we have shown that myelin can dynamically change its length and grow within a demyelinated patch of the axon, and frequently go back to the initial position (Auer et al., 2018). Therefore, I wanted to test the fate of nodal clusters following local demyelination. Do myelin sheaths that infiltrate the demyelinated area grow over nodal clusters? Do they push these nodal clusters along as they grow? Can nodes move independently from adjacent myelin? In order to answer these questions, I specifically ablated cells that make consecutive sheaths on individual axons in order to create heminodes and “isolated” nodes, with no adjacent myelin (Figure 3.43A, B).

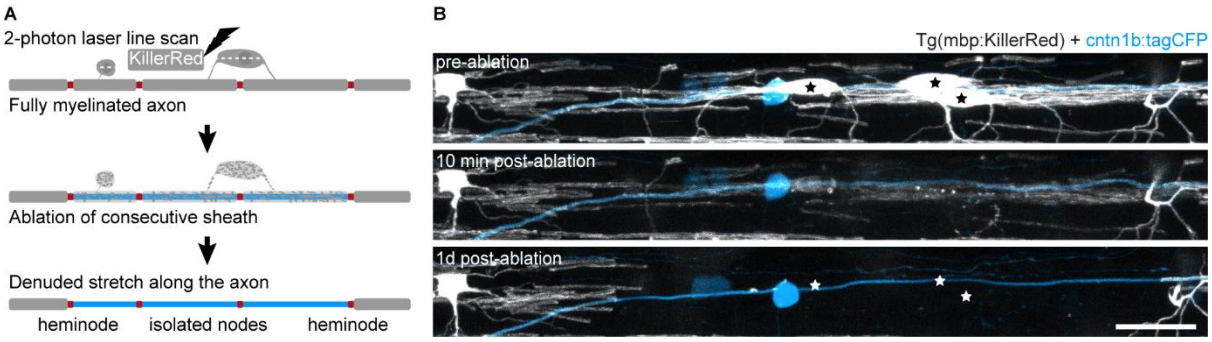

Figure 3.43 Ablating oligodendrocytes in order to demyelinate single axons and study nodal marker localization dynamics.

A. Cartoon - consecutive sheath ablation to create isolated nodes and heminodes.
B. Example images of multi-oligodendrocyte ablations to denude stretches of single axons. Stars indicate targeted oligodendrocytes. Scale bar = 20µm.

First, I performed ablations of cells myelinating an EYFP-cntn1a-expressing axon. As was previously described cntn1a-fusion markers serve as negative myelination label (Koudelka et al., 2016), being excluded from myelinated segments and labelling only unmyelinated areas and nodes of Ranvier. As I was unable to detect any clusters involving EYFP-cntn1a, I was curious about whether it can diffuse into demyelinated areas upon myelin clearance. Indeed, following ablations in this setting, it became apparent that EYFP-cntn1a readily diffused into the demyelinated area (Figure 3.44).

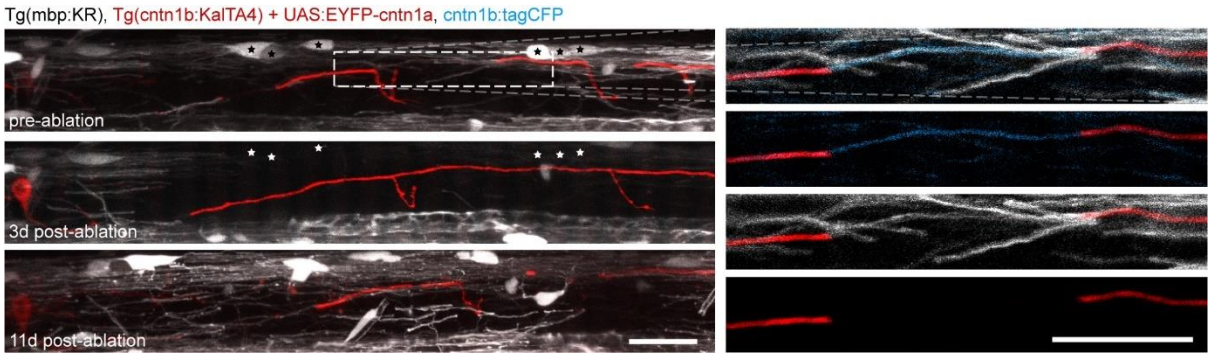

Figure 3.44 EYFP-cntn1a diffuses back into the axon upon demyelination.

(Left) Time-lapse images of a partially myelinated axon (CiD) expressing sigpep-EYFP-cntn1a pre-, 3d- and 11d- post ablation. Note that EYFP-cntn1a diffuses in the axon upon demyelination. (Right) Blow-up of the boxed area showing a myelin sheath on the same axon. Scale bars = 25 um.

In Figure 3.28, I was able to show that EYFP-cntn1a was the only marker that showed differential localisation on RB neurites, where it was excluded from the myelinated segment as described. Taking this into account, together with its diffusion into demyelinated areas further reinforces the idea that EYFP-cntn1a is a negative marker for myelination, that is likely removed from myelinated axonal stretches by the paranodal junction and when this is lost, it can freely diffuse along the axon, with likely no control of its positioning by the axon itself.

Since Nfasca-EYFP was the only nodal marker that participated in the formation of clusters prior to myelination, I hypothesised that this would be the most suitable marker to use in order to study nodal fate following local demyelination. To that end, I performed ablations of oligodendrocytes that myelinated axons expressing Nfasca-EYFP.

I was able to observe that Nfasca-EYFP, in contrast to EYFP-cntn1a, did not diffuse along the demyelinated axonal stretch, but remained concentrated, either as isolated nodes with no flanking myelin, or heminodes unilaterally contacted by surviving myelin time (Figure 3.45 A, B). Only 2/18 analysed nodes disappeared over the course of the experiment (Figure 3.45 C).

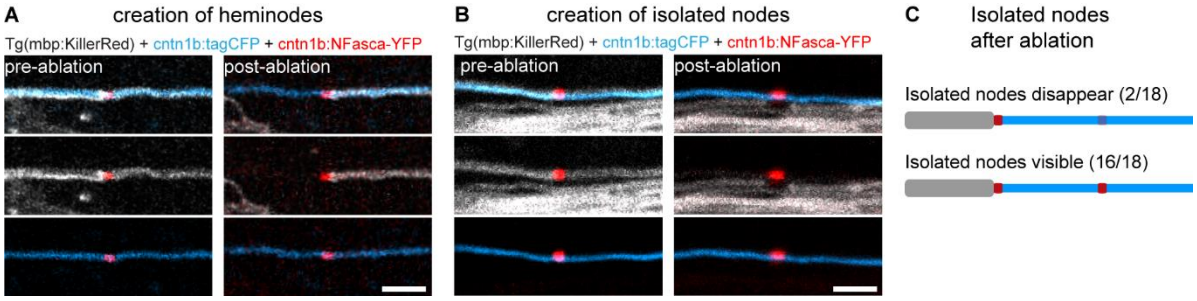

Figure 3.45 Nfasca-EYFP appears concentrated at the heminodes or isolated nodes following myelin loss.

A. Images of individually labelled axon co-expressing Nfasca-EYFP before and after oligodendrocyte ablation leading to creation of a heminode. Scale bar = 5µm.
B. Images as in panel A showing the creation of isolated nodes. Scale bar = 5µm.
C. Cartoon – Frequency of isolated nodes disappearance in all ablation experiments.

Since Nfasca-EYFP was able to label nodal structures even after demyelination, I wanted to analyse the dynamics of such molecules. As expected, control nodes and heminodes on non-ablated, control fish retained a rather stable position over time (Figure 3.46 C, E, E'). However, heminodes induced by the ablations as well as isolated nodes changed their position significantly following loss of their neighbouring myelin (Figure 3.46 A, B, E, E'). The motility of isolated nodes over the first three days post ablation was 2.7-fold higher than that of control nodes (1.51±0.77 µm/day in control *vs*. 4.14±3.41 for isolated nodes, n= 20/5/5 and 17/7/7 nodes/axons/animals, p= 0.01, Kruskal-Wallis test - Figure 3.46 E'). The motility of heminodes was 4.3-fold higher that control nodes (1.51±0.77 µm/day in control *vs* 6.51±3.41 for heminodes, n= 20/5/5 and 21/7/7 nodes/axons/animals, p < 0.0001, Kruskal-Wallis on absolute values; Figure 3.46 E').

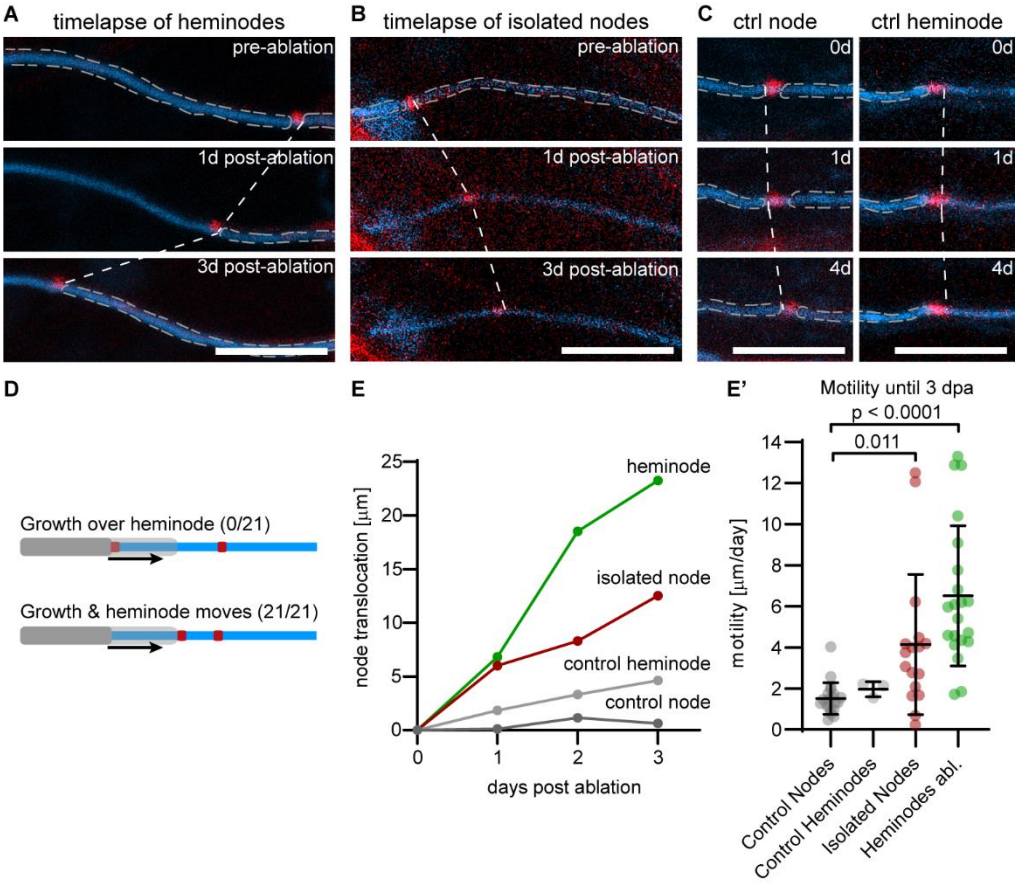

Figure 3.46 Dynamics of Nfasca-EYFP following demyelination.

A. Timeline of an example heminode co-expressing tagCFP and Nfasca-EYFP following unilateral myelin loss. Grey dashed areas represent traces of myelin sheath. White dashed lines indicate movement between timepoints. Scale bar:10 µm.
B. Images as in panel A showing the movements of an example isolated node following ablations. Scale bar:10 µm.
C. Images as in panel A showing a control node of Ranvier (left) and a control heminode(right). Scale bar:10 µm.
D. Cartoon – frequency of sheath growth over a heminode created by the ablations.
E. Quantification of node translocation for the examples in panels A-C. **E'.** Quantification of daily motility of different node phenotypes. Data are expressed as mean ± SD (Kruskal–Wallis test, p values depicted in the graph).

This experiment verifies that Nfasca-EYFP-carrying heminodes are still able to remodel, like what we had already described after ablation of single sheaths (Auer et al., 2018). However, and most interestingly, it seems that isolated nodes can also remodel their position following myelin loss, and in the absence of any adjacent myelin, the only possible source for this motility is the axon itself. This shows for the first time that axons have the capacity to finetune the position of their functional domains in a cell specific manner, possibly trying to maintain their homeostasis.

To summarize, upon local demyelination of single axons, Nfasca-EYFP does not diffuse back into the axon but instead labels induced heminodes and isolated nodes. The axon is able, in the absence of glial contribution, to modulate the position of isolated nodes. Induced heminodes are also highly motile, probably as a result of synergy between axonal mechanisms and glial growth. These mechanisms might represent an attempt of the partially demyelinated axon to modulate its conduction properties in order to preserve its function and show for the first time the capacity of individual axons to intrinsically modulate their node distribution pattern in the absence of adjacent myelin.

4.Discussion

4.1 Oligodendrocyte differentiation dynamics after demyelination.

Demyelination is a prominent feature in many serious pathologies of the CNS, such as multiple sclerosis (MS), a disease that causes localized myelin damage within the CNS. While there is still no effective cure for such diseases, research is ongoing, and several models of demyelinating pathologies have been introduced.

These models include immune-mediated demyelination methods like EAE, where common protein components of myelin, like myelin basic protein (MBP) or myelin oligodendrocyte glycoprotein (MOG) are used to immunise animal models, commonly rats and mice, in order to cause an autoimmune reaction and subsequent demyelination (Gold et al., 2000). Other models use chemical compounds that specifically affect myelin, like lysolecithin (Cunha et al., 2020; Jeffery & Blakemore, 1995) or OLs, like cuprizone (Baxi et al., 2017) and ethidium bromide (Blakemore, 1982). Genetic ablations of oligodendrocytes were also used (). Further, chemogenetic ablations of OLs have been reported, using the NTR-MTZ system (Chung et al., 2013; Sekizar et al., 2015) as well as the DTR/DTX system (Gritsch et al., 2014; Oluich et al., 2012) and the TRPV1-capsaicin system (Neely et al., 2020). Finally, targeted laser-ablations of OLs have also been frequently conducted (Auer et al., 2018; Chapman et al., 2020; Kirby et al., 2006; Snaidero et al., 2020).

Another way to categorise demyelination model is the proposed “inside-out” and “outside-in” models. In the “inside-out” model, myelin damage leads to the formation of myelin debris that are then recognised by immune cells as antigens and trigger an immune response against myelin. An example of an “inside-out” model is reportedly the cuprizone-mediated demyelination. In the “outside in” model, a foreign antigen is causing a systemic immune response that leads to demyelination. Such examples are the Japanese Macaque Encephalomyelitis (JME) or relapsing-remitting EAE (R-EAE) models (Titus et al., 2020).

How do these different models of demyelination compare to each other? Generally, EAE, cuprizone-induced demyelination and the chemogenetic methods cause diluted demyelination throughout the CNS, while lysolecithin (or EtBr) induced demyelination as well as laser ablation techniques, cause localised myelin damage (Torre-Fuentes et al., 2020). Regarding specialised targeting, the chemogenetic approaches affect exclusively OLs that express their genetic component (NTR, DTR or TRPV1). However, as with cuprizone-based demyelination, chemogenetic methods depend on the bioavailability of their chemical component (MTZ, DTX or capsaicin) and effects can vary from cell to cell. Lastly, by design, the laser based OL ablations allow for tight control of the specificity of OL targeting at the single cell level.

Contrary to most of the other cell populations, OL-lineage cells retain the capacity for regeneration, thanks to the persistent population of OPCs, resident in the CNS throughout life. These OPCs can differentiate into oligodendrocytes and remyelinate axons following myelin loss. However, this process has proven inefficient for cellular and functional recovery in patients suffering from myelin pathologies (R. J. M. Franklin, 2002). Overall, most of the already mentioned models are suitable for studying demyelination as well as remyelination, apart from EAE (Torre-Fuentes et al., 2020).

I decided to use a laser-based ablation method to selectively ablate individual OLs in the spinal cord of larval zebrafish. Zebrafish is ideal for studying myelination *in vivo* (Preston & Macklin, 2015). Moreover, the zebrafish spinal cord has a relatively small number of OLs (Marisca et al., 2020), the loss of which can create a lesion of considerable size. Also, using laser ablations allows for having internal controls (non-targeted OLs as well as the contralateral side of the spinal cord), which is a clear advantage for studying the dynamics of myelination and remyelination in the same tissue over time *in vivo*, not possible in any model of diluted myelin damage.

My first aim was to characterise the cellular dynamics in response to local demyelination. Following laser ablations of KillerRed-expressing OLs, targeted cell somata disintegrate rapidly (withing minutes) while demyelinated areas could be easily identified both using light as well as electron microscopy as soon as 1 dpa. Then phagocytes (including native to the CNS microglia and infiltrating

macrophages) react and infiltrate the lesion site minutes after myelin damage, in numbers analogous to the amount of ablated OLs., where they appear to remove most of the largest OL debris. This increase in phagocytes within the lesion site peaked at 1 dpa and by 5 dpa most phagocytes left the affected area. It has long been known that remyelination can be inhibited by the presence of myelin debris following OL death (Kotter et al., 2006). More recently, it has been proven that indeed removal of cellular debris by immune cells is essential for an effective regenerative response (R. Berglund et al., 2020b; Cunha et al., 2020), so infiltration of phagocytes is an important prerequisite for remyelination to take place.

In order to study remyelination, it was important to verify that demyelinated axons within demyelinated lesions survive. It has been described that lysolecithin-induced demyelination damages axons and other cell types within the lesion (Plemel et al., 2018) By using both confocal as well as electron microscopy, I found that OL ablations do not cause bystander damage to axons in the vicinity of the targeted OLs and that the population of axons within the dorsal tract of the spinal cord with perimeter > 0.7 μm remains intact.

By performing OL ablations at 6 dpf, I was able to describe the dynamics of OL differentiation for one week post-lesion (6-13 dpf). It is widely accepted that zebrafish, both larval and adult, are “champions” of regeneration after spinal cord injury and this ability to regenerate several cell types makes them attractive research tools for CNS regeneration (Cigliola et al., 2020). It is also known that zebrafish spinal cord contains a stable population of OPCs that continuously differentiate, at least until 30 dpf (Marisca et al., 2020). My ablation experiments showed that OL numbers fail to reach control levels by 13 dpf, leading to only partial remyelination. New OLs seemed to differentiate at similar rates in both the affected and the control side of the spinal cord, with only a marginal, yet significant, increase in differentiation in the ablated (ipsilateral) side.

However, it is known that increased axonal availability can induce individual OLs to produce more myelin(Almeida et al., 2011). It was possible that the limited amount of OLs that differentiate after myelin loss can compensate by myelinating more axons. In order to test this hypothesis, I analysed

electron micrographs of the spinal cord and compared the ablated to the control sides of the spinal cord. I found that the ablated side had significantly less myelinated axons than the control side, mirroring the results of the cell number quantification. This would indicate that newly differentiated OLs do not possess an enhanced ability to produce more myelin. However, direct observations by sparce OL labelling are needed in order to verify this extrapolation.

It is important to note that since OLs are constantly generated during normal development (Marisca et al., 2020), it might be challenging to distinguish OLs that differentiate as a result of their developmental program versus the ones that spawn as a regenerative response to myelin damage, even though these experiments were designed in order to exclude the rapid increase in OL numbers that happens between 3 and 5 dpf. Yet, it remains possible that the effect I observed was the product of ongoing developmental myelination, as its dynamics were too slow to be considered regeneration. Moreover, one week might not be enough time for the OPCs to differentiate. It is possible that enhanced oligodendrogenesis would have taken place only later, after my observations had been completed. Lastly, there might be a threshold for myelin damage that can induce increased OPC responses, that is higher than the type of titrated, localised myelin lesion that I introduced in my experiments.

Together, my ablation experiments showed that developing zebrafish failed to show enhanced repair to local CNS demyelination, despite the expectations that zebrafish is an excellent model to study regeneration. However, zebrafish remains an excellent model for *in vivo* microscopy and the persistence of myelin lesions within its CNS renders it just as useful in the study of myelin pathologies as the more classical model systems. It would be interesting to study how myelin regeneration could be enhanced, either by increasing the numbers of OPCs that differentiate or their capacity to make more myelin sheaths. This could be achieved by using pharmacological substances that affect myelination (Early et al., 2018) or increase neuronal activity, since activity affects myelin sheath growth (Baraban et al., 2018; Krasnow et al., 2018) To combat the problem of ongoing differentiation, it would be ideal to perform a similar study in young adult zebrafish, after 30 dpf. However, the optical

characteristics of the tissue at that developmental stage would likely limit the ability of intravital imaging. An alternative idea would be the use of Danionella, a small teleost that remains translucent to adulthood and could be ideal for *in vivo* microscopy and optical ablation methods.

4.2 Target axon selection in remyelination.

Knowing that newly differentiated OLs do not make enough myelin in order to repair the induced damage, the next logical question I had was to assess if the newly differentiated OLs have any preference between remyelinating axons that were demyelinated or myelinating axons that were previous unmyelinated. By comparing both confocal and electron microscopy images, I was able to show that between 6 and 13 dpf, new axons are myelinated within the dorsal axon tract of the spinal cord, while after 10 dpf, a new axon tract is myelinated in the lateral spinal cord.

By comparing the rate of increase of myelinated axons over time between the dorsal tract and the newly formed, lateral tract, it was evident that myelination occurs at similar rates in both, despite that the lateral tract contains axons that would have been myelinated during that time and that the dorsal tract contained axons that were demyelinated. This indicates that new OLs do not have a preference between demyelinated or unmyelinated axons in this choice scenario, but rather would myelinate any axon target in their vicinity.

It is known that axon calibre is a factor that influences axon choice in myelination (Stassart et al., 2018). It is also known that myelin deposition leads to axonal radial growth (Costa et al., 2018). However, how myelinated axon calibre changes upon demyelination remained unexplored. The zebrafish spinal cord and specifically the dorsal tract, represents an elegant system to measure calibre changes in demyelination. Knowing from my experiments that the ablation paradigm I applied did not cause any bystander axon damage, I was confident in my identification of axons in the dorsal tract that lost their myelin. By measuring their perimeter, I could show that demyelinated axons in the ablated side were smaller than the myelinated axons of the control side, meaning that axon calibre decreases upon demyelination. This might further impact conduction at a local level, leading to a cumulative effect in combination with the saltatory conduction block that is a direct consequence of local demyelination. Moreover, this shows that not only sheaths that are neighbouring to a demyelinated areas can plastically change in response to myelination (Auer et al., 2018), but axons

themselves undergo structural changes upon myelin damage. Lastly, a local decrease in axon diameter might be one reason demyelinated axons are not preferably remyelinated when new OLs differentiate.

Future studies are needed to identify axonal features that could enhance remyelination. First, axonal surface or secreted molecules could serve as markers of axonal identity that could make them more attractive for myelination at a given time. Within the system I studied maybe these molecules are expressed by lateral axons that are myelinated during the duration of my observations, but not by demyelinated axons. Moreover, it is known that neuronal activity can affect myelination locally (Krasnow et al. 2018, Baraban et al. 2018). Selective stimulation of demyelinated axons, possibly by optogenetics, could be used to activate demyelinated axons and to observe if increased activity could render them more attractive for remyelination. Lastly, it is known that PTEN can influence axon calibre. By inactivating PTEN selectively in demyelinated axons and thus increasing their calibre, one could assess how calibre changes could assist in accurate target axon choice for faithful remyelination (Goebbels et al., 2017).

4.3 Axonal contribution in the regulation of myelination pattern/node positioning.

Nodal components are known to be assembled at the nodes of Ranvier during development either by axon-intrinsic (cytoskeleton or ECM) or axon-extrinsic mechanisms (Glial ECM-paranodal adhesion) (Susuki et al., 2013). While there has been a long line of research investigating how nodal components are recruited at the nodes of Ranvier, little is known on how these molecules are positioned along the length of individual axons. This poses an important question in our understanding of myelination because the localisation of nodes of Ranvier defines the myelination pattern of each individual axon, which in turn can affect its conductive properties (Brill et al., 1977).

To dynamically observe the distribution of different nodal components prior to, during and after myelination, I injected 3 different constructs that were predicted to localise all at the nodes of Ranvier. All 3 constructs appeared initially diffused along the length of unmyelinated axonal stretches, but only one, Nfasca-EYFP formed clusters *in vivo*, along unmyelinated axonal areas. I was able to characterise the dynamics of these clusters as well as their fate and found that the majority of the clusters appeared in the position of a future node of Ranvier or a stable heminode. However, other neurites of the spinal cord, like the Rohon-beard neurons, that are normally only sporadically myelinated (Nelson et al., 2019), failed to show clustered Nfasca-EYFP, further highlighting that the clustering might be an exclusive feature of to-be-myelinated axons. Furthermore, some clusters were not stable, but they could be translocated by merging with the heminode of a growing sheath, leading to the conclusion that two mechanisms exist at the same time for the placement of nodes of Ranvier, an axon-intrinsic one and an oligodendrocyte-intrinsic one. In fact, the pharmacological treatment I conducted to create an environment characterised by sparser myelination, allowed for sheaths to grow more, confirming that the presence of an adjacent sheath can also affect myelin sheath length and thus node position.

Recently, several myelination patterns have been described, understanding the formation of which is challenging and at the moment not entirely clear. Certain neuronal subtypes of cortical neurons have reportedly only partial myelin coverage (Tomassy et al., 2014). Such partial myelination patterns have been also described in zebrafish (Auer et al., 2018; Nelson et al., 2019). Moreover, another interesting and highly complex myelination pattern is that of the axons of the auditory system in gerbils, where sheaths get progressively smaller, the closer to the synapse and the furthest from the some (Ford et al., 2015). Clustering of nodal molecules might affect the formation of myelination patterns. While clusters of nodal components have been already shown *in vitro* ((M. Kaplan et al., 1997) and in immunohistological analyses (S. A. Freeman et al., 2015), these clusters were never observed dynamically *in vivo* and their occurrence at the future positions of nodes of Ranvier had not been explored.

Yet a question still remained: Is Nfasca-EYFP just a marker that labels pre-nodal clusters, or does Nfasca have functional importance in the regulation of node positioning? To answer this question, I analysed internodal distances in zebrafish with mutated Nfasca, that was dissociated from the axonal membrane. I found that, in these animals, internodal distances were less regular and on average longer than in wildtype. Importantly, this effect could be reversed by re-expressing Nfasca (as part of the Nfasca-EYFP marker construct) in individual neurons. These results indicate that, not only Nfasca localises to pre-nodal clusters, but that its presence is necessary for the establishment of the myelination pattern of individual neurons.

It has already been shown that nodal pre-clusters are only a feature of a subset of neurons (S. A. Freeman et al., 2015), so further analyses are required to assess which axons of the CNS take advantage of this mechanism. Furthermore, murine mutants of Nfasca (NF-186) die at early postnatal stages (Sherman et al., 2005; Zonta et al., 2008). It is unclear why Nfasca mutant zebrafish do not show any adverse effects in their longevity. It is possible that a soluble, truncated Nfasca peptide is still expressed and could minimize the phenotype. Alternatively, it is known that zebrafish

have a separate gene for glial neurofascin (*nfascb*) (Klingseisen et al., 2019). Possibly, this glial isomorph could be expressed in axons to compensate for the loss of the neuronal isomorph.

Lastly, the molecular mechanisms behind cluster formation need to be investigated. While my results show that Nfasca plays a role in the formation of stable clusters and thus in the formation of myelination patterns, it remains unclear if it is implicated in the seeding of these clusters, or rather in their stability and localisation, so that in its absence, growing sheaths could push clusters and continue growing, until they encounter a neighbouring sheath. Together, these results illustrate for the first time that neurons have the capacity to influence, via pre-nodal clustering, their own myelination pattern.

4.4 Node position remodelling following local demyelination.

My experiments have shown the importance of Nfasca in regulating node position (and thus myelin length) along individual axons. Importantly, I was able to show that Nfasca appears clustered along the length of axons prior to the onset of myelination, with the position of these clusters often correlating with the future position of nodes of Ranvier. Additionally, the majority of nodes of Ranvier formed where a cluster previously resided. These results suggested the presence of an axon-intrinsic mechanism for regulating the myelination pattern. As we have shown previously (Auer et al., 2018), the myelination pattern can plastically change upon removal of single internodes but would often be restored in remyelination. Since the myelin sheath in these experiments was created by newly differentiated oligodendrocytes, it is conceivable that the information for the position of the node prior to demyelination could be retained by some axonal cues that reside in the axo-glial interface at the node of Ranvier.

In order to test this hypothesis, I performed ablations, aiming to ablate at least two consecutive internodes, in order to isolate nodes of Ranvier, labelled with different nodal marker constructs. First I performed ablations on axons expressing the cntn1b:EYFP-cntn1a construct, that bears no direct connection to the axonal cytoskeleton (Koudelka et al., 2016). This protein however diffused out in the demyelinated axonal stretch, showing that it EYFP-cntn1a indeed serves as a negative marker for myelination, rather than a nodal marker. Moreover, as cntn1a interacts with proteins of the extracellular matrix (Haenisch et al., 2005), one can infer from this result that possibly the extracellular matrix is reorganised and diffuses along demyelinated axon stretches, thus it could not regulate the restoration of myelin patterns during remyelination.

On the other hand, demyelinated axon stretches with nodes labelled with Nfasca-EYFP did not show diffusion of this marker, which rather remained clustered as an “isolated node”. As I only aimed to partially demyelinate the axons, sheaths bordering the demyelinated area had nodes that were, due

to unilateral myelin loss, become “induced heminodes”. This allowed me to observe and describe the dynamics of these “induced heminodes” and “isolated nodes” over time.

Confirming our earliest observation on surviving sheath dynamic growth upon local myelin loss, I found that indeed “induced heminodes” were highly motile. Nfasca-EYFP was always at the leading edge of the surviving heminode as it grew into the demyelinating area. The absence of myelin growth over “induced heminodes”, but rather the “pushing” of these structures by the sheath as it re-initiates growth, indicates that these Nfasca-EYFP aggregates after ablation are localising properly in the plasma membrane of the axon and can be “pushed” by the growing internode, mirroring what happens in many cases during developmental myelination. Surprisingly, “isolated nodes” were also motile in the absence of adjacent myelin, albeit moving more slowly than the “induce heminodes”.

These results give for the first time, important insight into the trafficking of Nfasca upon demyelination. The topic of the distribution of nodal components after myelin loss has already been studied. AnkG has been shown to diffuse into areas with paranodal labelling following OL ablation (Oluich et al., 2012), while voltage-gated sodium channels 1.2 and 1.6 also seemed to diffuse in EAE in the CNS (Craner et al., 2003, 2004). Lastly, regarding NFasc-186 (homolog of Nfasca), while it has been reported that it diffuses within demyelinated areas in MS, close inspection of the data shows that while its localisation is disrupted, it looks more like “isolated nodes” or clusters than a diffusion (Howell et al., 2006). More recently, it has been shown that cytoskeletal nodal components can also remain clustered upon demyelination. (Orthmann-Murphy et al., 2020). My results confirm that Nfasca can remain clustered upon demyelination, hinting that the axon itself can maintain their localisation through other axonal proteins, possibly elements of the axonal cytoskeleton.

In order to further investigate this process, it is important for these experiments to be repeated, but probing for other nodal components, such as AnkG and sodium channels. If AnkG remains clustered, it would be interesting to understand how it could affect the positioning of Nfasca clusters and what would the relevant mechanism for axon transport would be. If sodium channels remain clustered, it is possible that they, through their high local concentrations, could facilitate “microsaltatory”

conduction along the demyelinated axonal stretch, as an attempt to alleviate the effect of the ablations on AP propagation and network function (Lubetzki et al., 2020). This prospect is rendered more interesting by my EM data that suggest that axonal diameter might decrease upon demyelination. Knowing that both internodal distance and axonal diameter can affect conduction (Brill et al., 1977), “isolated node” translocation together with radial shrinkage might be two mechanisms of axonal structural response to local myelin loss. An electrophysiological experiment to measure the conduction velocity of single, partially demyelinated axons could help clarifying this prospect. Alternatively, it is conceivable that this putative mechanism depends on neuronal activity. Another experiment would be to activate the partially demyelinated neurons to observe whether the dynamics of “isolated nodes” change, as a response to the increased frequency of AP.

To summarize, I was able to study the dynamics of different nodal proteins upon local myelin loss. I could confirm that nodal Nfasca-EYFP does not appear diluted after demyelination, but rather remains clustered as “induced heminodes” and “isolated nodes”. Especially the presence of “isolated nodes” in the demyelinated areas suggests the presence of an axon-intrinsic mechanism that maintains their localisation and can modulate their location, theoretically in order to attempt to restore saltatory conduction.

5. References

Akay, L. A., Effenberger, A. H. & Tsai, L.-H. (2021). Cell of all trades: oligodendrocyte precursor cells in synaptic, vascular, and immune function. *Genes & Development*, *35*(3–4), 180–198. https://doi.org/10.1101/gad.344218.120

Almeida, R. G., Czopka, T., ffrench-Constant, C. & Lyons, D. A. (2011). Individual axons regulate the myelinating potential of single oligodendrocytes in vivo. *Development*, *138*(20), 4443–4450. https://doi.org/10.1242/dev.071001

Auer, F., Vagionitis, S. & Czopka, T. (2018). Evidence for Myelin Sheath Remodeling in the CNS Revealed by In Vivo Imaging. *Current Biology*, *28*(4), 549-559.e3. https://doi.org/10.1016/j.cub.2018.01.017

Bacmeister, C. M., Barr, H. J., McClain, C. R., Thornton, M. A., Nettles, D., Welle, C. G. & Hughes, E. G. (2020). Motor learning promotes remyelination via new and surviving oligodendrocytes. *Nature Neuroscience*, 1–13. https://doi.org/10.1038/s41593-020-0637-3

Baraban, M., Koudelka, S. & Lyons, D. A. (2018). Ca2+ activity signatures of myelin sheath formation and growth in vivo. *Nature Neuroscience*, *21*(1), 19–23. https://doi.org/10.1038/s41593-017-0040-x

Baxi, E. G., DeBruin, J., Jin, J., Strasburger, H. J., Smith, M. D., Orthmann-Murphy, J. L., Schott, J. T., Fairchild, A. N., Bergles, D. E. & Calabresi, P. A. (2017). Lineage tracing reveals dynamic changes in oligodendrocyte precursor cells following cuprizone-induced demyelination. *Glia*, *65*(12), 2087–2098. https://doi.org/10.1002/glia.23229

Bechler, M. E., Byrne, L. & ffrench-Constant, C. (2015). CNS Myelin Sheath Lengths Are an Intrinsic Property of Oligodendrocytes. *Current Biology*, *25*(18), 2411–2416. https://doi.org/10.1016/j.cub.2015.07.056

Bengtsson, S. L., Nagy, Z., Skare, S., Forsman, L., Forssberg, H. & Ullén, F. (2005). Extensive piano practicing has regionally specific effects on white matter development. *Nature Neuroscience*, *8*(9), 1148–1150. https://doi.org/10.1038/nn1516

Berglund, E. O., Murai, K. K., Fredette, B., Sekerková, G., Marturano, B., Weber, L., Mugnaini, E. & Ranscht, B. (1999). Ataxia and Abnormal Cerebellar Microorganization in Mice with Ablated Contactin Gene Expression. *Neuron*, *24*(3), 739–750. https://doi.org/10.1016/s0896-6273(00)81126-5

Berglund, R., Guerreiro-Cacais, A. O., Adzemovic, M. Z., Zeitelhofer, M., Lund, H., Ewing, E., Ruhrmann, S., Nutma, E., Parsa, R., Thessen-Hedreul, M., Amor, S., Harris, R. A., Olsson, T. & Jagodic, M. (2020a). Microglial autophagy–associated phagocytosis is essential for recovery from neuroinflammation. *Science Immunology*, *5*(52), eabb5077. https://doi.org/10.1126/sciimmunol.abb5077

Berglund, R., Guerreiro-Cacais, A. O., Adzemovic, M. Z., Zeitelhofer, M., Lund, H., Ewing, E., Ruhrmann, S., Nutma, E., Parsa, R., Thessen-Hedreul, M., Amor, S., Harris, R. A., Olsson, T. &

Jagodic, M. (2020b). Microglial autophagy–associated phagocytosis is essential for recovery from neuroinflammation. *Science Immunology*, *5*(52), eabb5077. https://doi.org/10.1126/sciimmunol.abb5077

Bhat, M. A., Rios, J. C., Lu, Y., Garcia-Fresco, G. P., Ching, W., Martin, M., Li, J., Einheber, S., Chesler, M., Rosenbluth, J., Salzer, J. L. & Bellen, H. J. (2001). Axon-Glia Interactions and the Domain Organization of Myelinated Axons Requires Neurexin IV/Caspr/Paranodin. *Neuron*, *30*(2), 369–383. https://doi.org/10.1016/S0896-6273(01)00294-X

Blakemore, W. F. (1974). Pattern of remyelination in the CNS. *Nature*, *249*(5457), 577–578. https://doi.org/10.1038/249577a0

Blakemore, W. F. (1982). ETHIDIUM BROMIDE INDUCED DEMYELINATION IN THE SPINAL CORD OF THE CAT. *Neuropathology and Applied Neurobiology*, *8*(5), 365–375. https://doi.org/10.1111/j.1365-2990.1982.tb00305.x

Blakemore, W. F. & Franklin, R. J. M. (2008). Advances in multiple Sclerosis and Experimental Demyelinating Diseases. *Current Topics in Microbiology and Immunology*, *318*, 193–212. https://doi.org/10.1007/978-3-540-73677-6_8

Boyle, M. E. T., Berglund, E. O., Murai, K. K., Weber, L., Peles, E. & Ranscht, B. (2001). Contactin Orchestrates Assembly of the Septate-like Junctions at the Paranode in Myelinated Peripheral Nerve. *Neuron*, *30*(2), 385–397. https://doi.org/10.1016/s0896-6273(01)00296-3

Brill, M. H., Waxman, S. G., Moore, J. W. & Joyner, R. W. (1977). Conduction velocity and spike configuration in myelinated fibres: computed dependence on internode distance. *Journal of Neurology, Neurosurgery & Psychiatry*, *40*(8), 769. https://doi.org/10.1136/jnnp.40.8.769

Bulina, M. E., Chudakov, D. M., Britanova, O. V., Yanushevich, Y. G., Staroverov, D. B., Chepurnykh, T. V., Merzlyak, E. M., Shkrob, M. A., Lukyanov, S. & Lukyanov, K. A. (2005). A genetically encoded photosensitizer. *Nature Biotechnology*, *24*(1), 95–99. https://doi.org/10.1038/nbt1175

Chapman, T. W., Olveda, G. E., Pereira, E. & Hill, R. A. (2020). Age and axon-specific forms of cortical remyelination by divergent populations of NG2-glia. *BioRxiv*, 2020.12.09.414755. https://doi.org/10.1101/2020.12.09.414755

Charles, P., Hernandez, M. P., Stankoff, B., Aigrot, M. S., Colin, C., Rougon, G., Zalc, B. & Lubetzki, C. (2000). Negative regulation of central nervous system myelination by polysialylated-neural cell adhesion molecule. *Proceedings of the National Academy of Sciences*, *97*(13), 7585–7590. https://doi.org/10.1073/pnas.100076197

Charles, Perrine, Tait, S., Faivre-Sarrailh, C., Barbin, G., Gunn-Moore, F., Denisenko-Nehrbass, N., Guennoc, A.-M., Girault, J.-A., Brophy, P. J. & Lubetzki, C. (2002). Neurofascin Is a Glial Receptor for the Paranodin/Caspr-Contactin Axonal Complex at the Axoglial Junction. *Current Biology*, *12*(3), 217–220. https://doi.org/10.1016/S0960-9822(01)00680-7

Chen, M., Xu, Y., Huang, R., Huang, Y., Ge, S. & Hu, B. (2017). N-Cadherin is Involved in Neuronal Activity-Dependent Regulation of Myelinating Capacity of Zebrafish Individual Oligodendrocytes In Vivo. *Molecular Neurobiology*, *54*(9), 6917–6930. https://doi.org/10.1007/s12035-016-0233-4

Chung, A.-Y., Kim, P.-S., Kim, S., Kim, E., Kim, D., Jeong, I., Kim, H.-K., Ryu, J.-H., Kim, C.-H., Choi, J., Seo, J.-H. & Park, H.-C. (2013). Generation of demyelination models by targeted ablation of oligodendrocytes in the zebrafish CNS. *Molecules and Cells*, *36*(1), 82–87. https://doi.org/10.1007/s10059-013-0087-9

Cigliola, V., Becker, C. J. & Poss, K. D. (2020). Building bridges, not walls: spinal cord regeneration in zebrafish. *Disease Models & Mechanisms*, *13*(5), dmm044131. https://doi.org/10.1242/dmm.044131

Collinson, J. M., Marshall, D., Gillespie, C. S. & Brophy, P. J. (1998). Transient expression of neurofascin by oligodendrocytes at the onset of myelinogenesis: Implications for mechanisms of axon-glial interaction. *Glia*, *23*(1), 11–23. https://doi.org/10.1002/(sici)1098-1136(199805)23:1<11::aid-glia2>3.0.co;2-7

Costa, A. R., Pinto-Costa, R., Sousa, S. C. & Sousa, M. M. (2018). The Regulation of Axon Diameter: From Axonal Circumferential Contractility to Activity-Dependent Axon Swelling. *Frontiers in Molecular Neuroscience*, *11*, 319. https://doi.org/10.3389/fnmol.2018.00319

Craner, M. J., Lo, A. C., Black, J. A. & Waxman, S. G. (2003). Abnormal sodium channel distribution in optic nerve axons in a model of inflammatory demyelination. *Brain*, *126*(7), 1552–1561. https://doi.org/10.1093/brain/awg153

Craner, M. J., Newcombe, J., Black, J. A., Hartle, C., Cuzner, L. M. & Waxman, S. G. (2004). Molecular changes in neurons in multiple sclerosis: Altered axonal expression of Nav1.2 and Nav1.6 sodium channels and Na+/Ca2+ exchanger. *Proceedings of the National Academy of Sciences of the United States of America*, *101*(21), 8168–8173. https://doi.org/10.1073/pnas.0402765101

Cunha, M. I., Su, M., Cantuti-Castelvetri, L., Müller, S. A., Schifferer, M., Djannatian, M., Alexopoulos, I., Meer, F. van der, Winkler, A., Ham, T. J. van, Schmid, B., Lichtenthaler, S. F., Stadelmann, C. & Simons, M. (2020). Pro-inflammatory activation following demyelination is required for myelin clearance and oligodendrogenesis. *Journal of Experimental Medicine*, *217*(5). https://doi.org/10.1084/jem.20191390

Czopka, T. (2016). Insights into mechanisms of central nervous system myelination using zebrafish. *Glia*, *64*(3), 333–349. https://doi.org/10.1002/glia.22897

Czopka, T., ffrench-Constant, C. & Lyons, D. A. (2013). Individual Oligodendrocytes Have Only a Few Hours in which to Generate New Myelin Sheaths In Vivo. *Developmental Cell*, *25*(6), 599–609. https://doi.org/10.1016/j.devcel.2013.05.013

Czopka, T. & Lyons, D. A. (2011). Chapter 2 Dissecting Mechanisms of Myelinated Axon Formation Using Zebrafish. *Methods in Cell Biology*, *105*, 25–62. https://doi.org/10.1016/b978-0-12-381320-6.00002-3

Desmazieres, A., Zonta, B., Zhang, A., Wu, L.-M. N., Sherman, D. L. & Brophy, P. J. (2014). Differential Stability of PNS and CNS Nodal Complexes When Neuronal Neurofascin Is Lost. *The Journal of Neuroscience*, *34*(15), 5083–5088. https://doi.org/10.1523/jneurosci.4662-13.2014

Early, J. J., Cole, K. L., Williamson, J. M., Swire, M., Kamadurai, H., Muskavitch, M. & Lyons, D. A. (2018). An automated high-resolution in vivo screen in zebrafish to identify chemical regulators of myelination. *ELife*, *7*, e35136. https://doi.org/10.7554/eLife.35136

Eaton, R. C., DiDomenico, R. & Nissanov, J. (1991). Role of the Mauthner Cell in Sensorimotor Integration by the Brain Stem Escape Network. *Brain, Behavior and Evolution*, *37*(5), 272–285. https://doi.org/10.1159/000114365

Ford, M. C., Alexandrova, O., Cossell, L., Stange-Marten, A., Sinclair, J., Kopp-Scheinpflug, C., Pecka, M., Attwell, D. & Grothe, B. (2015). Tuning of Ranvier node and internode properties in myelinated axons to adjust action potential timing. *Nature Communications*, *6*(1), 8073. https://doi.org/10.1038/ncomms9073

Franklin, R. J. & ffrench-Constant, C. (2017). Regenerating CNS myelin — from mechanisms to experimental medicines. *Nature Reviews Neuroscience*, *18*(12), nrn.2017.136. https://doi.org/10.1038/nrn.2017.136

Franklin, R. J. M. (2002). Why does remyelination fail in multiple sclerosis? *Nature Reviews Neuroscience*, *3*(9), 705–714. https://doi.org/10.1038/nrn917

Franklin, R. J. M. & ffrench-Constant, C. (2008). Remyelination in the CNS: from biology to therapy. *Nature Reviews Neuroscience*, *9*(11), 839–855. https://doi.org/10.1038/nrn2480

Franklin, R. J. M. & ffrench-Constant, C. (2017). Regenerating CNS myelin — from mechanisms to experimental medicines. *Nature Reviews Neuroscience*, *18*(12), 753–769. https://doi.org/10.1038/nrn.2017.136

Freeman, M. R. & Rowitch, D. H. (2013). Evolving Concepts of Gliogenesis: A Look Way Back and Ahead to the Next 25 Years. *Neuron*, *80*(3), 613–623. https://doi.org/10.1016/j.neuron.2013.10.034

Freeman, S. A., Desmazières, A., Simonnet, J., Gatta, M., Pfeiffer, F., Aigrot, M., Rappeneau, Q., Guerreiro, S., Michel, P., Yanagawa, Y., Barbin, G., Brophy, P. J., Fricker, D., Lubetzki, C. & Sol-Foulon, N. (2015). Acceleration of conduction velocity linked to clustering of nodal components precedes myelination. *Proceedings of the National Academy of Sciences*, *112*(3), E321–E328. https://doi.org/10.1073/pnas.1419099112

Fünfschilling, U., Supplie, L. M., Mahad, D., Boretius, S., Saab, A. S., Edgar, J., Brinkmann, B. G., Kassmann, C. M., Tzvetanova, I. D., Möbius, W., Diaz, F., Meijer, D., Suter, U., Hamprecht, B., Sereda, M. W., Moraes, C. T., Frahm, J., Goebbels, S. & Nave, K.-A. (2012). Glycolytic oligodendrocytes maintain myelin and long-term axonal integrity. *Nature*, *485*(7399), 517–521. https://doi.org/10.1038/nature11007

Garrido, J., Giraud, P., Carlier, E., Fernandes, F., Moussif, A., Fache, M.-P., Debanne, D. & Dargent, B. (2003). A Targeting Motif Involved in Sodium Channel Clustering at the Axonal Initial Segment. *Science*, *300*(5628), 2091–2094. https://doi.org/10.1126/science.1085167

Goebbels, S., Wieser, G. L., Pieper, A., Spitzer, S., Weege, B., Yan, K., Edgar, J. M., Yagensky, O., Wichert, S. P., Agarwal, A., Karram, K., Renier, N., Tessier-Lavigne, M., Rossner, M. J., Káradóttir, R. T. & Nave, K.-A. (2017). A neuronal PI(3,4,5)P3-dependent program of

oligodendrocyte precursor recruitment and myelination. *Nature Neuroscience*, *20*(1), 10–15. https://doi.org/10.1038/nn.4425

Gold, R., Hartung, H.-P. & Toyka, K. V. (2000). Animal models for autoimmune demyelinating disorders of the nervous system. *Molecular Medicine Today*, *6*(2), 88–91. https://doi.org/10.1016/s1357-4310(99)01639-1

Goulding, M. (2009). Circuits controlling vertebrate locomotion: moving in a new direction. *Nature Reviews Neuroscience*, *10*(7), 507–518. https://doi.org/10.1038/nrn2608

Gritsch, S., Lu, J., Thilemann, S., Wörtge, S., Möbius, W., Bruttger, J., Karram, K., Ruhwedel, T., Blanfeld, M., Vardeh, D., Waisman, A., Nave, K.-A. & Kuner, R. (2014). Oligodendrocyte ablation triggers central pain independently of innate or adaptive immune responses in mice. *Nature Communications*, *5*(1), 5472. https://doi.org/10.1038/ncomms6472

Gudi, V., Gai, L., Herder, V., Tejedor, L. S., Kipp, M., Amor, S., Sühs, K.-W., Hansmann, F., Beineke, A., Baumgärtner, W., Stangel, M. & Skripuletz, T. (2017). Synaptophysin Is a Reliable Marker for Axonal Damage. *Journal of Neuropathology & Experimental Neurology*, *76*(2), 109–125. https://doi.org/10.1093/jnen/nlw114

Haenisch, C., Diekmann, H., Klinger, M., Gennarini, G., Kuwada, J. Y. & Stuermer, C. (2005). The neuronal growth and regeneration associated Cntn1 (F3/F11/Contactin) gene is duplicated in fish: expression during development and retinal axon regeneration. *Molecular and Cellular Neuroscience*, *28*(2), 361–374. https://doi.org/10.1016/j.mcn.2004.04.013

Hedstrom, K. L., Xu, X., Ogawa, Y., Frischknecht, R., Seidenbecher, C. I., Shrager, P. & Rasband, M. N. (2007). Neurofascin assembles a specialized extracellular matrix at the axon initial segment. *The Journal of Cell Biology*, *178*(5), 875–886. https://doi.org/10.1083/jcb.200705119

Hill, R. A., Li, A. M. & Grutzendler, J. (2018). Lifelong cortical myelin plasticity and age-related degeneration in the live mammalian brain. *Nature Neuroscience*, *21*(5), 683–695. https://doi.org/10.1038/s41593-018-0120-6

Ho, T., Zollinger, D. R., Chang, K.-J., Xu, M., Cooper, E. C., Stankewich, M. C., Bennett, V. & Rasband, M. N. (2014). A hierarchy of ankyrin-spectrin complexes clusters sodium channels at nodes of Ranvier. *Nature Neuroscience*, *17*(12), nn.3859. https://doi.org/10.1038/nn.3859

Howell, O., Palser, A., Polito, A., Melrose, S., Zonta, B., Scheiermann, C., Vora, A., Brophy, P. & Reynolds, R. (2006). Disruption of neurofascin localization reveals early changes preceding demyelination and remyelination in multiple sclerosis. *Brain*, *129*(12), 3173–3185. https://doi.org/10.1093/brain/awl290

Hruscha, A., Krawitz, P., Rechenberg, A., Heinrich, V., Hecht, J., Haass, C. & Schmid, B. (2013). Efficient CRISPR/Cas9 genome editing with low off-target effects in zebrafish. *Development*, *140*(24), 4982–4987. https://doi.org/10.1242/dev.099085

Hughes, E. G., Orthmann-Murphy, J. L., Langseth, A. J. & Bergles, D. E. (2018). Myelin remodeling through experience-dependent oligodendrogenesis in the adult somatosensory cortex. *Nature Neuroscience*, *21*(5), 696–706. https://doi.org/10.1038/s41593-018-0121-5

Jang, M., Gould, E., Xu, J., Kim, E. & Kim, J. (2019). Oligodendrocytes regulate presynaptic properties and neurotransmission through BDNF signaling in the mouse brainstem. *ELife*, *8*, e42156. https://doi.org/10.7554/eLife.42156

Jeffery, N. D. & Blakemore, W. F. (1995). Remyelination of mouse spinal cord axons demyelinated by local injection of lysolecithin. *Journal of Neurocytology*, *24*(10), 775–781. https://doi.org/10.1007/bf01191213

Jepson, S., Vought, B., Gross, C. H., Gan, L., Austen, D., Frantz, J. D., Zwahlen, J., Lowe, D., Markland, W. & Krauss, R. (2012). LINGO-1, a Transmembrane Signaling Protein, Inhibits Oligodendrocyte Differentiation and Myelination through Intercellular Self-interactions. *Journal of Biological Chemistry*, *287*(26), 22184–22195. https://doi.org/10.1074/jbc.m112.366179

Jung, S., Kim, S., Chung, A., Kim, H., So, J., Ryu, J., Park, H. & Kim, C. (2010). Visualization of myelination in GFP-transgenic zebrafish. *Developmental Dynamics*, *239*(2), 592–597. https://doi.org/10.1002/dvdy.22166

Kaplan, M., Meyer-Franke, A., Lambert, S., Bennett, V., Duncan, I., Levinson, S. & Barres, B. (1997). Induction of sodium channel clustering by oligodendrocytes. *Nature*, *386*(6626), 386724a0. https://doi.org/10.1038/386724a0

Kaplan, M. R., Cho, M.-H., Ullian, E. M., Isom, L. L., Levinson, S. R. & Barres, B. A. (2001). Differential Control of Clustering of the Sodium Channels Nav1.2 and Nav1.6 at Developing CNS Nodes of Ranvier. *Neuron*, *30*(1), 105–119. https://doi.org/10.1016/S0896-6273(01)00266-5

Karttunen, M. J., Czopka, T., Goedhart, M., Early, J. J. & Lyons, D. A. (2017). Regeneration of myelin sheaths of normal length and thickness in the zebrafish CNS correlates with growth of axons in caliber. *PLOS ONE*, *12*(5), e0178058. https://doi.org/10.1371/journal.pone.0178058

Kirby, B. B., Takada, N., Latimer, A. J., Shin, J., Carney, T. J., Kelsh, R. N. & Appel, B. (2006). In vivo time-lapse imaging shows dynamic oligodendrocyte progenitor behavior during zebrafish development. *Nature Neuroscience*, *9*(12), 1506–1511. https://doi.org/10.1038/nn1803

Klingseisen, A., Ristoiu, A.-M. M., Kegel, L., Sherman, D. L., Rubio-Brotons, M., Almeida, R. G., Koudelka, S., Benito-Kwiecinski, S. K., Poole, R. J., Brophy, P. J. & Lyons, D. A. (2019). Oligodendrocyte Neurofascin Independently Regulates Both Myelin Targeting and Sheath Growth in the CNS. *Developmental Cell*, *51*(6), 730-744.e6. https://doi.org/10.1016/j.devcel.2019.10.016

Knafo, S., Fidelin, K., Prendergast, A., Tseng, P.-E. B., Parrin, A., Dickey, C., Böhm, U. L., Figueiredo, S. N., Thouvenin, O., Pascal-Moussellard, H. & Wyart, C. (2017). Mechanosensory neurons control the timing of spinal microcircuit selection during locomotion. *ELife*, *6*. https://doi.org/10.7554/eLife.25260

Komada, M. & Soriano, P. (2002). βIV-spectrin regulates sodium channel clustering through ankyrin-G at axon initial segments and nodes of Ranvier. *The Journal of Cell Biology*, *156*(2), 337–348. https://doi.org/10.1083/jcb.200110003

Kordeli, E., Lambert, S. & Bennett, V. (1995). AnkyrinG. A new ankyrin gene with neural-specific isoforms localized at the axonal initial segment and node of Ranvier. *The Journal of Biological Chemistry*, *270*(5), 2352–2359.

Kotter, M. R., Li, W.-W., Zhao, C. & Franklin, R. J. M. (2006). Myelin Impairs CNS Remyelination by Inhibiting Oligodendrocyte Precursor Cell Differentiation. *The Journal of Neuroscience*, *26*(1), 328–332. https://doi.org/10.1523/jneurosci.2615-05.2006

Koudelka, S., Voas, M. G., Almeida, R. G., Baraban, M., Soetaert, J., Meyer, M. P., Talbot, W. S. & Lyons, D. A. (2016). Individual Neuronal Subtypes Exhibit Diversity in CNS Myelination Mediated by Synaptic Vesicle Release. *Current Biology*, *26*(11), 1447–1455. https://doi.org/10.1016/j.cub.2016.03.070

Krasnow, A. M., Ford, M. C., Valdivia, L. E., Wilson, S. W. & Attwell, D. (2018). Regulation of developing myelin sheath elongation by oligodendrocyte calcium transients in vivo. *Nature Neuroscience*, *21*(1), 24–28. https://doi.org/10.1038/s41593-017-0031-y

Kwan, K. M., Fujimoto, E., Grabher, C., Mangum, B. D., Hardy, M. E., Campbell, D. S., Parant, J. M., Yost, H. J., Kanki, J. P. & Chien, C. (2007). The Tol2kit: A multisite gateway-based construction kit for Tol2 transposon transgenesis constructs. *Developmental Dynamics*, *236*(11), 3088–3099. https://doi.org/10.1002/dvdy.21343

Labun, K., Montague, T. G., Gagnon, J. A., Thyme, S. B. & Valen, E. (2016). CHOPCHOP v2: a web tool for the next generation of CRISPR genome engineering. *Nucleic Acids Research*, *44*(W1), W272–W276. https://doi.org/10.1093/nar/gkw398

Lassmann, H. & Bradl, M. (2017). Multiple sclerosis: experimental models and reality. *Acta Neuropathologica*, *133*(2), 223–244. https://doi.org/10.1007/s00401-016-1631-4

Laursen, L. S., Chan, C. W. & ffrench-Constant, C. (2009). An Integrin–Contactin Complex Regulates CNS Myelination by Differential Fyn Phosphorylation. *The Journal of Neuroscience*, *29*(29), 9174–9185. https://doi.org/10.1523/jneurosci.5942-08.2009

Lee, S., Leach, M. K., Redmond, S. A., Chong, S. Y. C., Mellon, S. H., Tuck, S. J., Feng, Z.-Q., Corey, J. M. & Chan, J. R. (2012). A culture system to study oligodendrocyte myelination processes using engineered nanofibers. *Nature Methods*, *9*(9), 917–922. https://doi.org/10.1038/nmeth.2105

Lee, X., Yang, Z., Shao, Z., Rosenberg, S. S., Levesque, M., Pepinsky, R. B., Qiu, M., Miller, R. H., Chan, J. R. & Mi, S. (2007). NGF Regulates the Expression of Axonal LINGO-1 to Inhibit Oligodendrocyte Differentiation and Myelination. *The Journal of Neuroscience*, *27*(1), 220–225. https://doi.org/10.1523/jneurosci.4175-06.2007

Linneberg, C., Harboe, M. & Laursen, L. S. (2015). Axo-Glia Interaction Preceding CNS Myelination Is Regulated by Bidirectional Eph-Ephrin Signaling. *ASN Neuro*, *7*(5), 1759091415602859. https://doi.org/10.1177/1759091415602859

Liu, C.-H., Stevens, S. R., Teliska, L. H., Stankewich, M., Mohler, P. J., Hund, T. J. & Rasband, M. N. (2020). Nodal β spectrins are required to maintain Na+ channel clustering and axon integrity. *ELife*, *9*, e52378. https://doi.org/10.7554/eLife.52378

Lubetzki, C., Zalc, B., Williams, A., Stadelmann, C. & Stankoff, B. (2020). Remyelination in multiple sclerosis: from basic science to clinical translation. *The Lancet Neurology*, *19*(8), 678–688. https://doi.org/10.1016/s1474-4422(20)30140-x

Ludwin, S. K. & Maitland, M. (1984). Long-term remyelination fails to reconstitute normal thickness of central myelin sheaths. *Journal of the Neurological Sciences*, *64*(2), 193–198. https://doi.org/10.1016/0022-510x(84)90037-6

Marisca, R., Hoche, T., Agirre, E., Hoodless, L. J., Barkey, W., Auer, F., Castelo-Branco, G. & Czopka, T. (2020). Functionally distinct subgroups of oligodendrocyte precursor cells integrate neural activity and execute myelin formation. *Nature Neuroscience*, 1–12. https://doi.org/10.1038/s41593-019-0581-2

McKenzie, I. A., Ohayon, D., Li, H., Faria, J. P. de, Emery, B., Tohyama, K. & Richardson, W. D. (2014). Motor skill learning requires active central myelination. *Science*, *346*(6207), 318–322. https://doi.org/10.1126/science.1254960

Mensch, S., Baraban, M., Almeida, R., Czopka, T., Ausborn, J., Manira, A. E. & Lyons, D. A. (2015). Synaptic vesicle release regulates myelin sheath number of individual oligodendrocytes in vivo. *Nature Neuroscience*, *18*(5), 628–630. https://doi.org/10.1038/nn.3991

Mi, S., Miller, R. H., Lee, X., Scott, M. L., Shulag-Morskaya, S., Shao, Z., Chang, J., Thill, G., Levesque, M., Zhang, M., Hession, C., Sah, D., Trapp, B., He, Z., Jung, V., McCoy, J. M. & Pepinsky, R. B. (2005). LINGO-1 negatively regulates myelination by oligodendrocytes. *Nature Neuroscience*, *8*(6), 745–751. https://doi.org/10.1038/nn1460

Miller, D. J., Duka, T., Stimpson, C. D., Schapiro, S. J., Baze, W. B., McArthur, M. J., Fobbs, A. J., Sousa, A. M. M., Šestan, N., Wildman, D. E., Lipovich, L., Kuzawa, C. W., Hof, P. R. & Sherwood, C. C. (2012). Prolonged myelination in human neocortical evolution. *Proceedings of the National Academy of Sciences*, *109*(41), 16480–16485. https://doi.org/10.1073/pnas.1117943109

Moore, S., Meschkat, M., Ruhwedel, T., Trevisiol, A., Tzvetanova, I. D., Battefeld, A., Kusch, K., Kole, M. H. P., Strenzke, N., Möbius, W., Hoz, L. de & Nave, K.-A. (2020). A role of oligodendrocytes in information processing. *Nature Communications*, *11*(1), 5497. https://doi.org/10.1038/s41467-020-19152-7

Morrison, B. M., Lee, Y. & Rothstein, J. D. (2013). Oligodendroglia: metabolic supporters of axons. *Trends in Cell Biology*, *23*(12), 644–651. https://doi.org/10.1016/j.tcb.2013.07.007

Münzel, E. J., Becker, C. G., Becker, T. & Williams, A. (2014). Zebrafish regenerate full thickness optic nerve myelin after demyelination, but this fails with increasing age. *Acta Neuropathologica Communications*, *2*(1), 77. https://doi.org/10.1186/s40478-014-0077-y

Nave, K.-A. (2010a). Myelination and support of axonal integrity by glia. *Nature*, *468*(7321), 244. https://doi.org/10.1038/nature09614

Nave, K.-A. (2010b). Myelination and the trophic support of long axons. *Nature Reviews Neuroscience*, *11*(4), 275. https://doi.org/10.1038/nrn2797

Neely, S. A., Williamson, J. M., Klingseisen, A., Zoupi, L., Early, J. J., Williams, A. & Lyons, D. A. (2020). New oligodendrocytes exhibit more abundant and accurate myelin regeneration than those that survive demyelination. *BioRxiv*, 2020.05.22.110551. https://doi.org/10.1101/2020.05.22.110551

Nelson, H. N., Treichel, A. J., Eggum, E. N., Martell, M. R., Kaiser, A. J., Trudel, A. G., Gronseth, J. R., Maas, S. T., Bergen, S. & Hines, J. H. (2019). Individual neuronal subtypes control initial myelin sheath growth and stabilization. *BioRxiv*, 809996. https://doi.org/10.1101/809996

Nelson, H. N., Treichel, A. J., Eggum, E. N., Martell, M. R., Kaiser, A. J., Trudel, A. G., Gronseth, J. R., Maas, S. T., Bergen, S. & Hines, J. H. (2020). Individual neuronal subtypes control initial myelin sheath growth and stabilization. *Neural Development*, *15*(1), 12. https://doi.org/10.1186/s13064-020-00149-3

Oluich, L.-J., Stratton, J. S., Xing, Y., Ng, S., Cate, H. S., Sah, P., Windels, F., Kilpatrick, T. J. & Merson, T. D. (2012). Targeted Ablation of Oligodendrocytes Induces Axonal Pathology Independent of Overt Demyelination. *The Journal of Neuroscience*, *32*(24), 8317–8330. https://doi.org/10.1523/JNEUROSCI.1053-12.2012

Orthmann-Murphy, J., Call, C. L., Molina-Castro, G. C., Hsieh, Y. C., Rasband, M. N., Calabresi, P. A. & Bergles, D. E. (2020). Remyelination alters the pattern of myelin in the cerebral cortex. *ELife*, *9*, e56621. https://doi.org/10.7554/elife.56621

Oumesmar, B. N., Vignais, L., Duhamel-Clerin, E., Avellana-Adalid, V., Rougon, G. & Evercooren, A. B. (1995). Expression of the Highly Polysialylated Neural Cell Adhesion Molecule During Postnatal Myelination and Following Chemically Induced Demyelination of the Adult Mouse Spinal Cord. *European Journal of Neuroscience*, *7*(3), 480–491. https://doi.org/10.1111/j.1460-9568.1995.tb00344.x

Pan, S., Mayoral, S. R., Choi, H., Chan, J. R. & Kheirbek, M. A. (2020). Preservation of a remote fear memory requires new myelin formation. *Nature Neuroscience*. https://doi.org/10.1038/s41593-019-0582-1

Park, H.-C., Hong, S.-K., Kim, H.-S., Kim, S.-H., Yoon, E.-J., Kim, C.-H., Miki, N. & Huh, T.-L. (2000). Structural comparison of zebrafish Elav/Hu and their differential expressions during neurogenesis. *Neuroscience Letters*, *279*(2), 81–84. https://doi.org/10.1016/s0304-3940(99)00940-4

Pérez-Cerdá, F., Sánchez-Gómez, M. V. & Matute, C. (2015). Pío del Río Hortega and the discovery of the oligodendrocytes. *Frontiers in Neuroanatomy*, *9*, 92. https://doi.org/10.3389/fnana.2015.00092

Pietri, T., Manalo, E., Ryan, J., Saint-Amant, L. & Washbourne, P. (2009). Glutamate drives the touch response through a rostral loop in the spinal cord of zebrafish embryos. *Developmental Neurobiology*, *69*(12), 780–795. https://doi.org/10.1002/dneu.20741

Pillai, A. M., Thaxton, C., Pribisko, A. L., Cheng, J., Dupree, J. L. & Bhat, M. A. (2009). Spatiotemporal ablation of myelinating glia-specific neurofascin (NfascNF155) in mice reveals gradual loss of paranodal axoglial junctions and concomitant disorganization of axonal domains. *Journal of Neuroscience Research*, *87*(8), 1773–1793. https://doi.org/10.1002/jnr.22015

Plemel, J. R., Michaels, N. J., Weishaupt, N., Caprariello, A. V., Keough, M. B., Rogers, J. A., Yukseloglu, A., Lim, J., Patel, V. V., Rawji, K. S., Jensen, S. K., Teo, W., Heyne, B., Whitehead, S. N., Stys, P. K. & Yong, V. W. (2018). Mechanisms of lysophosphatidylcholine-induced demyelination: A primary lipid disrupting myelinopathy. *Glia*, *66*(2), 327–347. https://doi.org/10.1002/glia.23245

Preston, M. A. & Macklin, W. B. (2015). Zebrafish as a model to investigate CNS myelination. *Glia*, *63*(2), 177–193. https://doi.org/10.1002/glia.22755

Prineas, J. W. & Connell, F. (1979). Remyelination in multiple sclerosis. *Annals of Neurology*, *5*(1), 22–31. https://doi.org/10.1002/ana.410050105

Purves, D., Augustine, G. J., Fitzpatrick, D., Hall, W. C., LaMantia, A., McNamara, J. O. & Williams, S. M. (2004). *Neuroscience, 3rd Edition*. Sinauer Associates, Inc.

Ratcliffe, C. F., Westenbroek, R. E., Curtis, R. & Catterall, W. A. (2001). Sodium channel β1 and β3 subunits associate with neurofascin through their extracellular immunoglobulin-like domain. *The Journal of Cell Biology*, *154*(2), 427–434. https://doi.org/10.1083/jcb.200102086

Redmond, S. A., Mei, F., Eshed-Eisenbach, Y., Osso, L. A., Leshkowitz, D., Shen, Y.-A. A., Kay, J. N., Aurrand-Lions, M., Lyons, D. A., Peles, E. & Chan, J. R. (2016). Somatodendritic Expression of JAM2 Inhibits Oligodendrocyte Myelination. *Neuron*, *91*(4), 824–836. https://doi.org/10.1016/j.neuron.2016.07.021

Roberts, A., Li, W. & Soffe, S. R. (2012). A functional scaffold of CNS neurons for the vertebrates: The developing Xenopus laevis spinal cord. *Developmental Neurobiology*, *72*(4), 575–584. https://doi.org/10.1002/dneu.20889

Rosenbluth, J. (1999). A brief history of myelinated nerve fibers: one hundred and fifty years of controversy. *Journal of Neurocytology*, *28*(4–5), 251–262. https://doi.org/10.1023/a:1007083409850

Schnädelbach, O., Özen, Í., Blaschuk, O. W., Gour, B. J., Meyer, R. L. & Fawcett, J. W. (2001). N-Cadherin Is Involved in Axon-Oligodendrocyte Contact and Myelination. *Molecular and Cellular Neuroscience*, *17*(6), 1084–1093. https://doi.org/10.1006/mcne.2001.0961

Scholz, J., Klein, M. C., Behrens, T. E. J. & Johansen-Berg, H. (2009). Training induces changes in white-matter architecture. *Nature Neuroscience*, *12*(11), 1370–1371. https://doi.org/10.1038/nn.2412

Sekizar, S., Mannioui, A., Azoyan, L., Colin, C., Thomas, J.-L., Pasquier, D. D., Mallat, M. & Zalc, B. (2015). Remyelination by Resident Oligodendrocyte Precursor Cells in a Xenopus laevis Inducible Model of Demyelination. *Developmental Neuroscience*, *37*(3), 232–242. https://doi.org/10.1159/000380817

Sherman, D. L., Tait, S., Melrose, S., Johnson, R., Zonta, B., Court, F. A., Macklin, W. B., Meek, S., Smith, A. J. H., Cottrell, D. F. & Brophy, P. J. (2005). Neurofascins Are Required to Establish Axonal Domains for Saltatory Conduction. *Neuron*, *48*(5), 737–742. https://doi.org/10.1016/j.neuron.2005.10.019

Sim, F. J., Zhao, C., Penderis, J. & Franklin, R. J. M. (2002). The Age-Related Decrease in CNS Remyelination Efficiency Is Attributable to an Impairment of Both Oligodendrocyte Progenitor Recruitment and Differentiation. *Journal of Neuroscience*, *22*(7), 2451–2459. https://doi.org/10.1523/jneurosci.22-07-02451.2002

Snaidero, N., Schifferer, M., Mezydlo, A., Zalc, B., Kerschensteiner, M. & Misgeld, T. (2020). Myelin replacement triggered by single-cell demyelination in mouse cortex. *Nature Communications*, *11*(1), 4901. https://doi.org/10.1038/s41467-020-18632-0

Stassart, R. M., Möbius, W., Nave, K.-A. A. & Edgar, J. M. (2018). The Axon-Myelin Unit in Development and Degenerative Disease. *Frontiers in Neuroscience*, *12*, 467. https://doi.org/10.3389/fnins.2018.00467

Stathopoulos, P., Alexopoulos, H. & Dalakas, M. C. (2015). Autoimmune antigenic targets at the node of Ranvier in demyelinating disorders. *Nature Reviews Neurology*, *11*(3), 143–156. https://doi.org/10.1038/nrneurol.2014.260

Steadman, P. E., Xia, F., Ahmed, M., Mocle, A. J., Penning, A. R. A. R., Geraghty, A. C., Steenland, H. W., Monje, M., Josselyn, S. A. & Frankland, P. W. (2020). Disruption of Oligodendrogenesis Impairs Memory Consolidation in Adult Mice. *Neuron*, *105*(1), 150-164.e6. https://doi.org/10.1016/j.neuron.2019.10.013

Susuki, K., Chang, K.-J., Zollinger, D. R., Liu, Y., Ogawa, Y., Eshed-Eisenbach, Y., Dours-Zimmermann, M. T., Oses-Prieto, J. A., Burlingame, A. L., Seidenbecher, C. I., Zimmermann, D. R., Oohashi, T., Peles, E. & Rasband, M. N. (2013). Three Mechanisms Assemble Central Nervous System Nodes of Ranvier. *Neuron*, *78*(3), 469–482. https://doi.org/10.1016/j.neuron.2013.03.005

Teh, C., Chudakov, D. M., Poon, K.-L., Mamedov, I. Z., Sek, J.-Y., Shidlovsky, K., Lukyanov, S. & Korzh, V. (2010). Optogenetic in vivocell manipulation in KillerRed-expressing zebrafish transgenics. *BMC Developmental Biology*, *10*(1), 110. https://doi.org/10.1186/1471-213X-10-110

Thaxton, C., Pillai, A. M., Pribisko, A. L., Dupree, J. L. & Bhat, M. A. (2011). Nodes of Ranvier Act as Barriers to Restrict Invasion of Flanking Paranodal Domains in Myelinated Axons. *Neuron*, *69*(2), 244–257. https://doi.org/10.1016/j.neuron.2010.12.016

Titus, H. E., Chen, Y., Podojil, J. R., Robinson, A. P., Balabanov, R., Popko, B. & Miller, S. D. (2020). Pre-clinical and Clinical Implications of "Inside-Out" vs. "Outside-In" Paradigms in Multiple Sclerosis Etiopathogenesis. *Frontiers in Cellular Neuroscience*, *14*, 599717. https://doi.org/10.3389/fncel.2020.599717

Tomassy, G., Berger, D. R., Chen, H.-H., Kasthuri, N., Hayworth, K. J., Vercelli, A., Seung, S. H., Lichtman, J. W. & Arlotta, P. (2014). Distinct Profiles of Myelin Distribution Along Single Axons of Pyramidal Neurons in the Neocortex. *Science*, *344*(6181), 319–324. https://doi.org/10.1126/science.1249766

Torre-Fuentes, L., Moreno-Jiménez, L., Pytel, V., Matías-Guiu, J. A., Gómez-Pinedo, U. & Matías-Guiu, J. (2020). Experimental models of demyelination and remyelination. *Neurología (English Edition)*, *35*(1), 32–39. https://doi.org/10.1016/j.nrleng.2019.03.007

Vagionitis, S. & Czopka, T. (2018). Myelin, Methods and Protocols. *Methods in Molecular Biology*, *1791*, 25–35. https://doi.org/10.1007/978-1-4939-7862-5_3

Vagionitis, S., Auer, F., Xiao, Y., Almeida, R.G., Lyons, D. A. & Czopka, T. (2021). Clusters of neuronal Neurofascin prefigure node of Ranvier position along single axons. *BioRxiv*, 2021.06.25.449890. https://doi.org/10.1101/2021.06.25.449890

Venable, J. H. & Coggeshall, R. (1965). A SIMPLIFIED LEAD CITRATE STAIN FOR USE IN ELECTRON MICROSCOPY. *The Journal of Cell Biology*, *25*(2), 407–408. https://doi.org/10.1083/jcb.25.2.407

Volkmer, H., Hassel, B., Wolff, J. M., Frank, R. & Rathjen, F. G. (1992). Structure of the axonal surface recognition molecule neurofascin and its relationship to a neural subgroup of the immunoglobulin superfamily. *The Journal of Cell Biology*, *118*(1), 149–161. https://doi.org/10.1083/jcb.118.1.149

Walton, E. M., Cronan, M. R., Beerman, R. W. & Tobin, D. M. (2015). The Macrophage-Specific Promoter mfap4 Allows Live, Long-Term Analysis of Macrophage Behavior during Mycobacterial Infection in Zebrafish. *PLOS ONE*, *10*(10), e0138949. https://doi.org/10.1371/journal.pone.0138949

Xin, W., Mironova, Y. A., Shen, H., Marino, R., Waisman, A., Lamers, W. H., Bergles, D. E. & Bonci, A. (2019). Oligodendrocytes Support Neuronal Glutamatergic Transmission via Expression of Glutamine Synthetase. *Cell Reports*, *27*(8), 2262-2271.e5. https://doi.org/10.1016/j.celrep.2019.04.094

Young, K. M., Psachoulia, K., Tripathi, R. B., Dunn, S.-J., Cossell, L., Attwell, D., Tohyama, K. & Richardson, W. D. (2013). Oligodendrocyte Dynamics in the Healthy Adult CNS: Evidence for Myelin Remodeling. *Neuron*, *77*(5), 873–885. https://doi.org/10.1016/j.neuron.2013.01.006

Zhou, D., Lambert, S., Malen, P. L., Carpenter, S., Boland, L. M. & Bennett, V. (1998). AnkyrinG Is Required for Clustering of Voltage-gated Na Channels at Axon Initial Segments and for Normal Action Potential Firing. *The Journal of Cell Biology*, *143*(5), 1295–1304. https://doi.org/10.1083/jcb.143.5.1295

Zonta, B., Tait, S., Melrose, S., Anderson, H., Harroch, S., Higginson, J., Sherman, D. L. & Brophy, P. J. (2008). Glial and neuronal isoforms of Neurofascin have distinct roles in the assembly of nodes of Ranvier in the central nervous system. *The Journal of Cell Biology*, *181*(7), 1169–1177. https://doi.org/10.1083/jcb.200712154

6. Publications

Auer, F., Vagionitis, S. & Czopka, T. (2018). Evidence for Myelin Sheath Remodeling in the CNS Revealed by In Vivo Imaging. *Current Biology*, *28*(4), 549-559.e3. https://doi.org/10.1016/j.cub.2018.01.017

Vagionitis, S. & Czopka, T. (2018). Myelin, Methods and Protocols. *Methods in Molecular Biology*, *1791*, 25–35. https://doi.org/10.1007/978-1-4939-7862-5_3

Vagionitis, S., Auer, F., Xiao, Y., Almeida, R.G., Lyons, D. A. & Czopka, T. (2021). Clusters of neuronal Neurofascin prefigure node of Ranvier position along single axons. *BioRxiv*, 2021.06.25.449890. https://doi.org/10.1101/2021.06.25.449890